OPEN-ENDCAP PAUL TRAPS FOR RADIAL-2D ION CRYSTALS

Yuanheng Xie

Submitted to the faculty of the University Graduate School

in partial fulfillment of the requirements

for the degree

Doctor of Philosophy

in the Department of Physics,

Indiana University

December 2022

Accepted by the Graduate Faculty, Indiana University, in partial fulfillment of the requirements for the degree of Doctor of Philosophy.

Doctoral Committee

Richerme, Phil, Ph.D (Chair)

Ortiz, Gerardo, Ph.D

Snow, W. Michael, Ph.D

Liao, Jinfeng, Ph.D

11/01/2022

ACKNOWLEDGEMENTS

This thesis is a work accumulated over many years, carried out with the support of many people. I would like to express my deepest appreciation to my advisor Dr. Phil Richerme, when I first joined Richerme's lab, Professor Richerme gives me a lot of guidance, he has an enormous enthusiasm for physics and vast knowledge and experience in research. I still remember the first several months in the lab, he taught me many basic tricks to prepare, assemble and bake the vacuum system, and every time in the group meeting, we discussed a lot of physics which refreshed my understanding. I've greatly appreciated his help and supervision. Many thanks to my committees, Dr. Gerardo Ortiz, Dr. W. Michael Snow, Dr. Jinfeng Liao, Dr. Herbert A. Fertig, Dr. Michael S. Berger, and Dr. Brian DeSalvo, who devote their time to my candidacy seminary, annual report and dissertation defense. I would also like to extend my deepest gratitude to Dr. Marissa D'Onofrio and AJ Rasmusson for their excellent contributions to the experiments. Marissa was my first colleague and my classmate, she dedicated her time to constructing the lab and doing research. Two years after our lab settled down in Simon Hall, AJ joined our lab. AJ is hard-working with the experiment and willing to share wonderful ideas with us. Both of them made big contributions to constructing our lab and we cultivate a deep friendship. I would like to extend my sincere thanks to Dr. Jifeng Cui, and Dr. Antonis Kyprianidis. Both of them are Post-doc in our lab, we had a great time working together, and they gave us many useful suggestions in simulation and electrical circuits. Thanks should also go to physics machine shop Machinist Gary wood, who gave me a lot of convenience in machining, especially for some work in rush time. My special gratitude goes to the many scientists with whom I have had the delight of working and who all contribute much to this work, in particular: Evangeline Wolanski, Paula Madetzke, Andrew Henderson, Michelle Lollie, Noah Schlossberger Justin Kittell. Exceptional much thanks my friends who bring joy to my life and encourage me to finish this Ph.D. program, namely: Juan Cai, Zhi Liu, Miao Wang, Jiazhou Shen, Wencao Yang, Ting Lin, Shuzhe Shi, Zidu Lin, Zheng Li, Hongfa Li, Shenyuan Huang, Shifang Wei, Siyi Tang,

Weihua Liu, Ying Pan.

Yuanheng Xie

OPEN-ENDCAP PAUL TRAPS FOR RADIAL-2D ION CRYSTALS

Quantum simulations of complex materials address fundamental problems that cannot be analytically solved due to the exponential scaling of the Hilbert space with increasing particle numbers. Simulations using trapped ions have had remarkable success investigating one-dimensional quantum interacting spin models, and we seek to extend these ideas to two dimensions by exploiting new crystal geometries in a radio frequency (rf) Paul trap. This 2d quantum simulation will allow us to address open questions related to geometric frustration, ground states and dynamics of long-range spin models, and quantum spin liquids. To approach that goal, we designed a new open-endcap, blade-style rf trap which can confine and resolve large numbers of ions in the radial-2D crystal phase, with this trap, we successfully trap up to 29 ions in 2D triangular configuration. Then we present an experimental study that establishes radial-2D crystals as a robust platform for quantum simulation, through the characterization of ion positions, structural phases, normal mode frequencies, and effects from rf heating. What's more, we examine other challenges faced by trapped ion systems: optimally cooling to the motional ground state, the most common methods for sideband cooling rely on low Doppler-cooled temperatures, and we introduce a framework that optimizes the pulsed sideband cooling sequence and verify its improvement compared to traditional methods. We also develop and experimentally validate an improved method to measure ion temperatures after sideband cooling and make a comparison with the previous thermometry. Additionally, our group measures the susceptibility of trapped-ion qubits to the presence of ionizing radiation, we expose an ion-trap apparatus to a variety of α, β, and γ sources and measure the resulting changes in trapped-ion qubit lifetimes, coherence times, gate fidelities, and motional heating rates. We also

propose high dose radiation experiments with our portable trap ion system for further radiation study.

Richerme, Phil, Ph.D (Chair)

Ortiz, Gerardo, Ph.D

Snow, W. Michael, Ph.D

Liao, Jinfeng, Ph.D

Contents

List of Figures

List of Tables

CHAPTER 1

Introduction

Richard Feynman pointed out that it is difficult for a classical computer to simulate quantum mechanical systems[1], suggesting that a quantum computer would be required instead. In 1994, Peter Shor proposed a famous quantum algorithm called Shor's Algorithm, which can factor exponentially faster than the current classic computer; this drew many researchers' attention in the quantum simulation area.

In quantum simulation, one of the most important concepts is the qubit, we already know the bit is the fundamental concept of classical information, and quantum simulations are built based on the analogous concept; the quantum bit (qubit for short) is the basic unit of quantum information. Just as the classical bit has a state - either 0 or 1, a qubit not only has two basic states $|0\rangle$ and $|1\rangle$ but also is possible to form a linear combination of states, often called superposition:

$$|\psi\rangle = \alpha|0\rangle + \beta|1\rangle \tag{1.1}$$

The numbers α and β are complex numbers, when we measured a qubit, we may get either the result 0 with probability $|\alpha|^2$ or the result 1 with probability $|\beta|^2$, naturally, $|\alpha|^2 + |\beta|^2 = 1$. Generally, a qubit state is the unit vector in a two-dimensional complex vector space. One good way to think about qubits is the following geometric representation. Due to $|\alpha|^2 + |\beta|^2 = 1$, we may rewrite Eq.1.1 as

$$|\psi\rangle = e^{i\gamma}(\cos\frac{\theta}{2}|0\rangle + e^{i\varphi}\sin\frac{\theta}{2}|1\rangle) \tag{1.2}$$

where θ,φ and γ are real number. The numbers θ and φ define a point on the unit 3-D sphere,

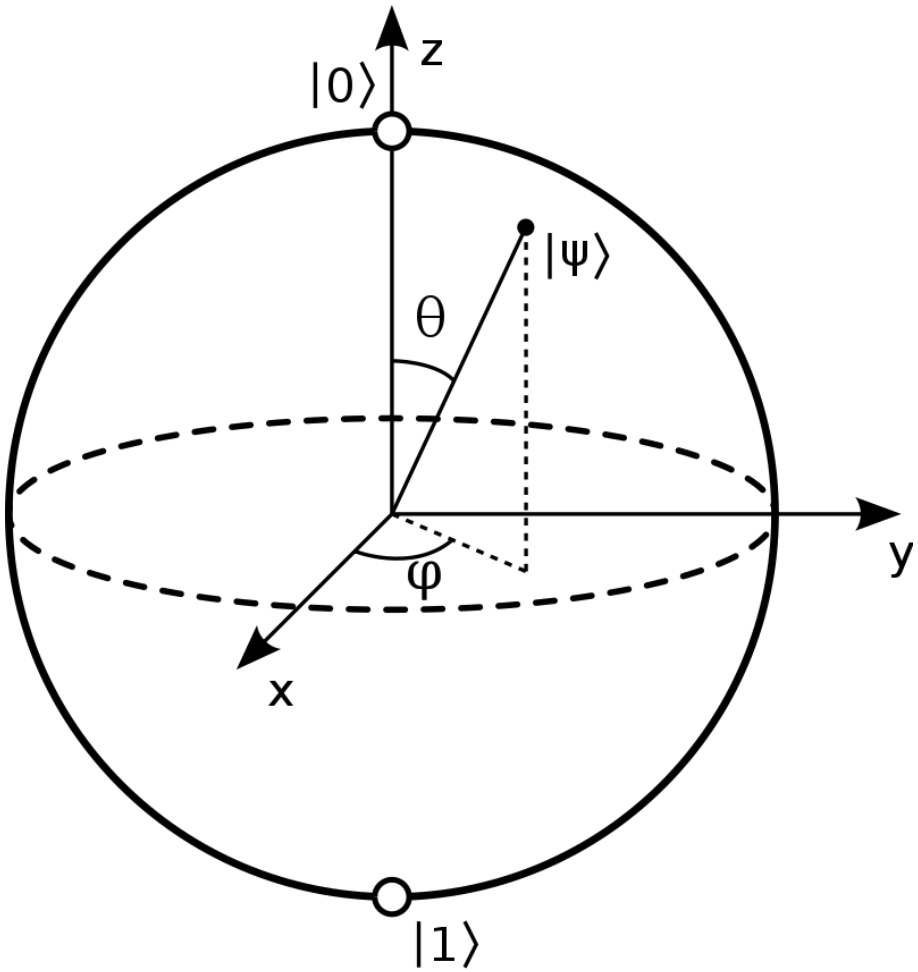

Figure 1.1: Bloch Sphere

often called the Bloch sphere. This useful tool can provide a means of visualizing a single qubit's state, and many of the operations on the single qubits are neatly described within the Bloch sphere picture.

Qubits selection has many choices, they could be atoms in 1D or 2D arrays of cavities[2, 3, 4, 5, 6], electrons in quantum dot arrays or superconducting circuits[7, 8, 9, 10, 11, 12, 13, 14], or ions in the linear ion trap or penning trap[15, 16, 17, 18, 19, 20, 21]. The qubits in our experiment are the trapped atomic ions, it is one of the most promising platform for quantum bits and simulation[22, 23, 21, 24, 25], which is evidenced by the ions' long coherence time[26], high fidelity of initializing the quantum state[21] and measurement[27], and the highest-reported single- and two-qubit gate fidelities [28, 29]. The trapped ion system is isolated by the vacuum

chamber and confined by the electromagnetic field, which can avoid most types of noise. The ions are laser-cooled, then applied to the external Raman laser or microwave to perform quantum operations. Their fundamental reproducibility, less noise, ease of control and readout, and strong ion-ion interactions present advantages among quantum simulation systems.

Quantum simulation involves more qubits, and the quantum state of a physical system can be represented in the superposition form. The information encoded in the quantum state has to be tracked by coefficients which are scaled exponentially due to the feature of superposition. For example, we consider an N two-level(spin up and spin down) physical system, the wave function $|\Psi\rangle$ can be written as:

$$|\Psi\rangle = \sum_{s_1=\{\uparrow,\downarrow\}} \cdots \sum_{s_N=\{\uparrow,\downarrow\}} a_{s_1,\ldots,s_N} |s_1, \ldots, s_N\rangle. \tag{1.3}$$

A 2^N coefficient $a_{s_1,\ldots,s_N}$ to describe the full wavefunction while a classical system requires only N coefficients for a possible outcome.

The probability amplitude for all possible quantum states scales exponentially, and the operations of the temporal evolution of the system during the simulation also increase exponentially with the size of the system increase, both of them would cause an exponential explosion for classical simulation. Classical numerical techniques like quantum Monte Carlo methods may give us an approximation of the many-body physics system. Still, they can not work when the large system and system involve tons of entanglements[30, 31]. Therefore, the simulation of quantum systems, in general, remains a hard task even for today's supercomputers, and quantum simulation is necessary to simulate quantum systems.

There are two types of quantum simulation. When we take a Hamiltonian that maps well onto a specific system we are interested in, then let it evolve for a certain time and see what happens, this is called analog simulation[32, 33, 34]. Another simulation, known as digital simulation[20]. The idea is the desired Hamiltonian which contributes from many terms $H = \sum_{i=1}^{l} H_l$. In general,

these terms may not commute with each other. We trotter the quantum operation matrix U with :

$$U = e^{-iHt} \approx (e^{-H_1 t/n} e^{-H_2 t/n} \dots e^{-H_l t/n})^n = (U_1 U_2 \dots U_l)^n \tag{1.4}$$

where n is the number of steps. This would be strict equality in Eq. 1.4 when all the unitaries commute with each other. With the trotterization, it forms a sequence of quantum operations U_1 to U_l, which now commute with each other. These operations can be applied one by one like digital computation and the error of approximation is proportional to the commutator.

Quantum simulation is useful for understanding the physics of the many-body system. Many success based on trapped ion system has been achieved in the past years: engineering high-fidelity quantum gates, such as two-qubit and single-qubit logic gates with respective fidelities 99.9(1)% and 99.9934(3)%[28]; general issues of quantum thermalization, such as many-body localization and prethermalization, "time crystals," dynamical phase transitions, and Hamiltonian engineering and sequencing techniques [35]. Among these successes, one-dimensional ion chains confined in the linear Paul traps have been the workhorse of quantum information processing experiments [36, 37, 38, 39, 40, 41, 42, 35]. Yet, many applications of trapped-ion quantum information are not well-matched to the capabilities of one-dimensional (1D) geometries, for example, the physics of a 2D system can be replicated in a 1D chain to some extent, this requires addressing every lattice site and perform gates between any pairs of ions, which demands building a fully-function universal quantum computer. This led us to think about finding two-dimensional geometries to expand the scope of the study. A native 2D lattice simplifies the lasers since only global beams are needed to make 2D interactions. The results will be much higher fidelity since it doesn't require nearly as many operations. Developing a well-controlled, scalable two-dimensional quantum simulator can help us understand the behavior of complex, two-dimensional (2D) quantum systems. And such a tunable and reconfigurable apparatus will be able to address important open questions in quantum many-body physics that are intractable to numerical calculation and inaccessible to any current experimental system.

Several parallel efforts to trap and manipulate 2D ion crystals are currently underway. For instance, 2D ion systems in microtrap arrays [43, 44] and in Penning traps [45, 46, 47] have made impressive progress over the last decade, but still face challenges of implementing fast quantum gates and individual addressing, respectively. To overcome such difficulties, several groups have proposed the trapping of 2D ion crystals using global potentials in standard or modified Paul traps [48, 49, 50, 51], however, the drawback of these schemes is the susceptibility of ions to radio frequency (rf) driven micromotion, which must be carefully considered during the trap-design stage to avoid potential effects such as rapid heating or loss of the ion crystal. Early ion-trapping work observed the confinement of 2D ion crystals in the “lateral-2D" phase, for which the rf-driven micromotion exists along both in-plane and out-of-plane directions [52], later work minimized excess micromotion in this geometry [53] and cooled ions to near their motional ground state [54].

Additionally, 2D ion crystals have been trapped in the "radial-2D" phase, for which the transverse modes are co-aligned with the trap axial axis and remain micromotion-free [55, 56]. In this geometry, 2D crystals had long lifetimes, well-characterized vibrational modes, and low heating rates in the out-of-plane (transverse) direction, validating the usefulness for quantum simulation experiments. The radial-2D crystals studied in reference [55] is confined in a linear Paul trap with "needle" style endcap electrodes [57], which block optical access along the trap axis (perpendicular to the radial plane). In such traps, it is only possible to view the radial-2D crystal from the side. To achieve full site-resolved imaging and enable the possibility of individual addressing for this crystal geometry, it is necessary to develop an open endcap linear Paul trap, which is the main task in these theses.

This thesis is divided into the following chapters:

The second chapter describes the necessary theoretical and experimental background on quantum simulation with trapped ions. We look at the pseudopotential approximation that ions experienced inside the linear trap, calculate the ion’s motion, and discuss the Mathieu stability regions. Moreover, this chapter also shows how to generate 2D ion crystals and analyze the precise ion’s motion, micormotion, and normal modes in the 2D geometry.

Chapter three details the segmented blade 2D ion trap and our considerations when designing the trap. It includes the techniques we use to polish the trap blades and details about trap assembly. This open-endcap trap design provides strong axial confinement to form clear radial 2D crystals and allows site-resolved imaging in the 2D crystal plane. In addition, in this chapter, the preparation of all hardware, such as vacuum chamber, voltage control, atomic oven, image system, computer control system, and PID feedback circuit, is also presented.

Chapter four defines a qubit within the electronic energy levels of Yb^+ 171, outlining the cooling method applied to ion and qubit initialization and detection. We also discuss the optical pathways, particularly the lasers that prepare the qubit and drive the stimulated Raman transitions. Finally, this chapter discusses how we trap ions and shows the 2D ion crystals we get in the two-dimensional ion trap.

Chapter five demonstrates optimized pulsed sideband cooling methods and new thermometry that can accurately evaluate the ion's temperature after sideband cooling(SBC). We present a framework for calculating the optimal sequence of SBC pulses for near-ground-state cooling and show the advantages of the optimal and multiorder cooling scheme between different cooling protocols. The thermometry technique we developed can more accurately measure $\bar{n}$ following SBC. Our optimal cooling strategy applies to any trapped-ion experiment using pulsed SBC and is flexible enough to incorporate decoherence effects or heating models if desired. Our close temperature measurement experimental agreement with theoretical predictions as well as significant improvements compared with the thermometry protocols.

The sixth chapter shows the experimental study on the radial-2D crystals, which is our 2D quantum simulation platform. In this chapter, we start with 13 ions in a linear chain, then demonstrate the structural phase boundaries of different phases and the traverses normal modes of the 2D crystal. Micromotion-induced heating rate measurements are also presented in this chapter by measuring the Voigt profile and verifying the transverse motional modes heating rate; we find our 2D crystal is well-predictable numerically and can remain decoupled from the radial mode.

Chapter seven discusses a radiation study on a single-ion performed in a rod-style linear Paul

trap. The real-time susceptibility of trapped-ion systems to a small dose of ionizing radiation. Our trapped ion is exposed to a variety of α, β, and γ sources and measures the lifetime, motional heating rates, coherence time, and gate fidelities. Our study shows that there is no quantifiable degradation of a trapped ion in the presence of low-dose radiation sources for the measurement we perform. We report on developing a portable ion trap for high-dose radiation study. This experiment is designed to fit within test chambers at high-dose radiation test facilities. The entire system is accommodated into a mobile rack unit comprising laser, electronics, and physics package subsystems.

The eighth chapter gives an outlook for future directions.

CHAPTER 2

Ion Trapping and Radial-2D Ion Crystals

2.1 Overview

Trapping particles makes it possible to prevent any contact between the particle and the thermal walls, by this way, we can get a well-controlled environment over a long period that allows very accurate measurement of the physical properties. Earnshaw's theorem tells us that charge particles cannot be trapped in a static field, but dynamically confining the charging particles is possible in a radio frequency electric field. The analogy with a ball moving on the saddle-shaped surface provides a way to understand the method for confining ions[58]. This linear Paul trap produced the trapped ion field assembled by the electrodes shown in Fig.2.1[59], the rods lie parallel to the z-axis and at the corners of a square in the XY-plane. Each rod is connected to the one diagonally opposite, and the a.c. Voltage is applied on the two pairs, and ions can be confined by this radio frequency electric field and electrostatic field. In addition, pre-cooling is necessary to make the kinetic energy of the particles smaller than the trap depth. This chapter briefly overviews the theoretical principle of an ion trap and how to realize a radial-2D ion crystal.

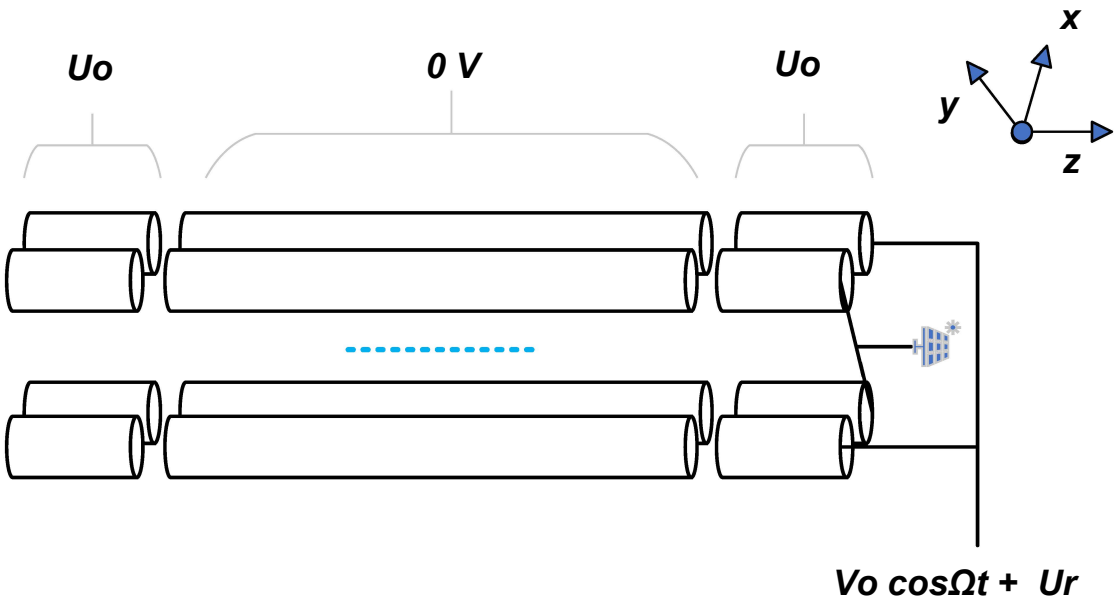

Figure 2.1: a schematic diagram of the electrode configuration for a linear Paul-rf trap

2.2 Ions confined in the Paul Traps

The rf or Paul trap can trap ions primarily through pondermotive forces generated by inhomogeneous oscillating fields [22]. A linear Paul trap is derived from the original design of Drees and Paul[22] as shown in Fig.2.1. A potential $V_0 \cos \Omega_T t + U_r$ applied between diagonally opposite electrodes, and the end segments along z direction hold a constant electric field as a function z, near the trap center axis, the potential can be written in this form:

$$\begin{aligned} \Phi(\vec{r}, t) &= \Phi_{dc}(\vec{r}) + \Phi_{rf}(\vec{r}, t) \\ &= \frac{\kappa U_0}{2z_0^2}(2z^2 - \chi x^2 - \gamma y^2) + \frac{V_0 \cos(\Omega_T t)}{2d_0^2}(x^2 - y^2) \end{aligned} \tag{2.1}$$

where U_0 is the dc voltage, V_0 is the amplitude of an rf voltage with oscillation frequency Ω_T, d_0 and z_0 are the radial and axial trap dimensions, and κ is a geometric factor of order one determined by the trap electrodes. In Eq. 2.1, we have also introduced the radial anisotropic factors χ and γ, which we experimentally choose to deviate slightly from one. (It is always required that $\chi + \gamma = 2$

to satisfy Laplace's equation). This small asymmetry breaks the degeneracy of the x and y radial axis, thereby preventing radial-2D crystals from rotating freely in the xy plane.

First, we review the time average force produced by an oscillating electric force. Let's consider charged particle in an oscillating field $V_0 \cos \Omega_T t$, then the force that acts on the particle is expressed as:

$$\begin{aligned} F = m\ddot{z} &= eE(z,t) \\ &= \frac{e}{2d} V_0 \cos \Omega_T t \\ &= eE_0(z) \cos \Omega_T t \end{aligned} \tag{2.2}$$

Where $E_o(z)$ and $\cos \Omega_T t$ are the spatial and temporal variation of the electric field. By integrating this equation, we got the solution of equation 2.2:

$$z(t) = z_0 - \frac{eE_0(z)}{m\Omega_T^2} \cos \Omega_T t \tag{2.3}$$

With the initial conditions $z(0) = z_0$, which represents the time-averaged position of the charged particle, and we have assumed that the particle was at rest at $t = 0$ ($\dot{z}(0) = 0$). It can be seen that, under a homogeneous oscillating field, a charged particle does not experience any confining potential. The average force felt by the particle is zero. By adding a small inhomogeneity in the driving electrical field $E_0(z)$ and expanding it to about $z = z_0$ and only taking the first two terms, we have

$$E_0(z) = E_0(z_0) + \partial_z E_0 \mid_{z=z_0} (z - z_0) \tag{2.4}$$

From equation 2.2 and 2.3, we substitute $z - z_0 = -\frac{eE_0(z)}{m\Omega_T^2} \cos \Omega_T t$ into equation 2.4, the time

dependent force experience by the particle is [60]:

$$\begin{aligned} F(t) &= eE_0(z)\cos\Omega_T t \\ &= e(E_0(z_0) + \partial_z E_0 \mid_{z=z_0} (z - z_0))\cos\Omega_T t \\ &= eE_0(z_0) + \frac{e^2}{m\Omega_T^2} E_0(z_0)\partial_z E_0 \mid_{z=z_0} (\cos\Omega_T t)^2 \end{aligned} \tag{2.5}$$

Then the time average of this force is

$$\begin{aligned} \bar{F}(z_0) = \langle F(t)\rangle &= -\frac{e^2}{2m\Omega_T^2} E_0(z_0)\partial_z E_0 \mid_{z=z_0} \\ &= -\frac{e^2}{4m\Omega_T^2}\partial_{z_0} E_0^2 \\ &= -e\frac{\partial}{\partial z_0}[\frac{e}{4m\Omega_T^2} E_0^2(z_0)] \\ &= -e\frac{\partial \phi_p}{\partial z_0} \end{aligned} \tag{2.6}$$

where we have defined the "pseudopotential" ϕ_p, also known as the ponderomotive potential:

$$\phi_p = \frac{e}{4m\Omega_T^2} E_0^2(z_0) \tag{2.7}$$

we extend the equation 2.6 into three dimension:

$$\bar{F} = -e\nabla\phi_p \text{ with } \phi_p = \frac{e(\vec{E}_0(x,y,z))^2}{4m\Omega_T^2} \tag{2.8}$$

Note that the force in equation 2.6 is not dependent on the sign of the charge. It can trap both positive and negative charge particles. The effects of higher order expansion of 2.4 are neglected here. However, it will produce different motion corresponding to $\cos\Omega_T t$ term is driven by the applied rf field and is called "micromotion." We will discuss it in the latter sections.

2.3 Pseudopotential approximation

In the linear Paul trap, the particle's motion illustrates in two dimensions, and we take a simple condition of Eq.2.1 into account. The potential close to the z-axis has the form of a quadruple potential:

$$\Phi(\vec{r}, t) = \frac{V_0}{2} \cos \Omega_T t (1 + \frac{x^2 - y^2}{r_0^2}). \tag{2.9}$$

where $r_0 = \sqrt{2} d_0$. From the gradient of potential Φ_{rf}, we find the electric field

$$\mathbf{E} = \mathbf{E}_0(r) \cos \Omega_T t = -\frac{V_0}{r_0^2} \cos \Omega_T t (x \hat{e}_x - y \hat{e}_y). \tag{2.10}$$

According to Eq.2.8, we obtain

$$\mathbf{F} = -\frac{e^2 V_0^2}{2m^2 \Omega_T^2 r_0^4} (x \hat{e}_x + y \hat{e}_y). \tag{2.11}$$

Looking at the equation of motion in the x-direction is

$$\frac{d^2 x}{dt^2} = -\frac{e^2 V_0^2}{2m^2 \Omega_T^2 r_0^4} x. \tag{2.12}$$

which gives us the secular frequency in the x direction (the result for y is the same):

$$\omega_x = \frac{eV_0}{\sqrt{2} m \Omega_T r_0^2} x. \tag{2.13}$$

The complete solution for a particle trapped in the ion trap is given by solving the Mathieu equation. We first derivative the Eq.2.9, yielding the equation of motion:

$$m \frac{d^2 x}{dt^2} = -\frac{eV_0}{r_0^2} \cos \Omega_T t x \tag{2.14}$$

A change of variable $\tau = \Omega_T t/2$ substitutes into the equation of motion leads to

$$\frac{d^2x}{dt^2} = -\frac{eV_0}{\Omega_T^2 m r_0^2}\cos\Omega_T t x \tag{2.15}$$

which is a simplified form of the Mathieu equation:

$$\frac{d^2x}{dt^2} - (a_x - 2q_x\cos 2\tau)x = 0 \tag{2.16}$$

with $a_x = 0$ and $q_x = 2eV_0/\Omega_T^2 m r_0^2$ when we not consider the dc confinement. Since the physical goal is to trap ions, we seek stable solutions to the equation of motion. According to Floquet theory, we look for a approximate solution to the form

$$x = x_0\cos A\tau\{1 + B\cos 2\tau\} \tag{2.17}$$

The arbitrary constant A gives the secular frequency of the overall motion, and B is the amplitude of the fast oscillation, which is the micromotion we mentioned before. Substitution into the equation (with $a_x = 0$) gives

$$\begin{aligned} x_0[-4B\cos A\tau\cos 2\tau + 4AB\sin A\tau\sin 2\tau - A^2\cos A\tau\{1 + B\cos 2\tau\}] \\ = 2q_x x_0\cos 2\tau\cos 2\tau\cos A\tau\{1 + B\cos 2\tau\} \end{aligned} \tag{2.18}$$

We shall assume that $A \ll 1$, and also the amplitude $B \ll 1$ (the term $B\cos 2\tau$ corresponds with the micromotion, that is the reason we assume the B is tiny). Thus the terms proportional to $\cos A\tau\cos 2\tau$ dominate on each side, and equating their coefficients gives $B = -q_x/2$ and $A = q_x/\sqrt{2}$. This gives An approximate solution

$$x = x_0\cos(\frac{q_x\tau}{\sqrt{2}} + \theta_0)\{1 + \frac{q_x}{2}\cos 2\tau\} \tag{2.19}$$

Since the $\tau = \Omega_T t/2$, the particle's average displacement undergoes simple harmonic motion at an

angular frequency given by

$$\omega_x = \frac{q_x \Omega_T}{2\sqrt{2}} = \frac{eV_0}{\sqrt{2}\Omega_T m r_0^2} \tag{2.20}$$

with the assumption $q_x \ll 1$, it is the same as we present before.

If we add the electrostatic constant terms Φ_{dc} back to our calculation, a_x is not zero and has a value $a_x = 2e\kappa U_0/\Omega_T^2 m z_0^2$. Then the secular frequency is modified as

$$\omega_x = \beta_i \frac{\Omega_T}{2}, \ \beta \simeq [a_x + q_x^2/2]^{1/2} \tag{2.21}$$

By symmetry, the same considerations apply for motion in the y-direction, and we define the radial frequency $\omega_r \equiv \omega_x = \omega_y$.

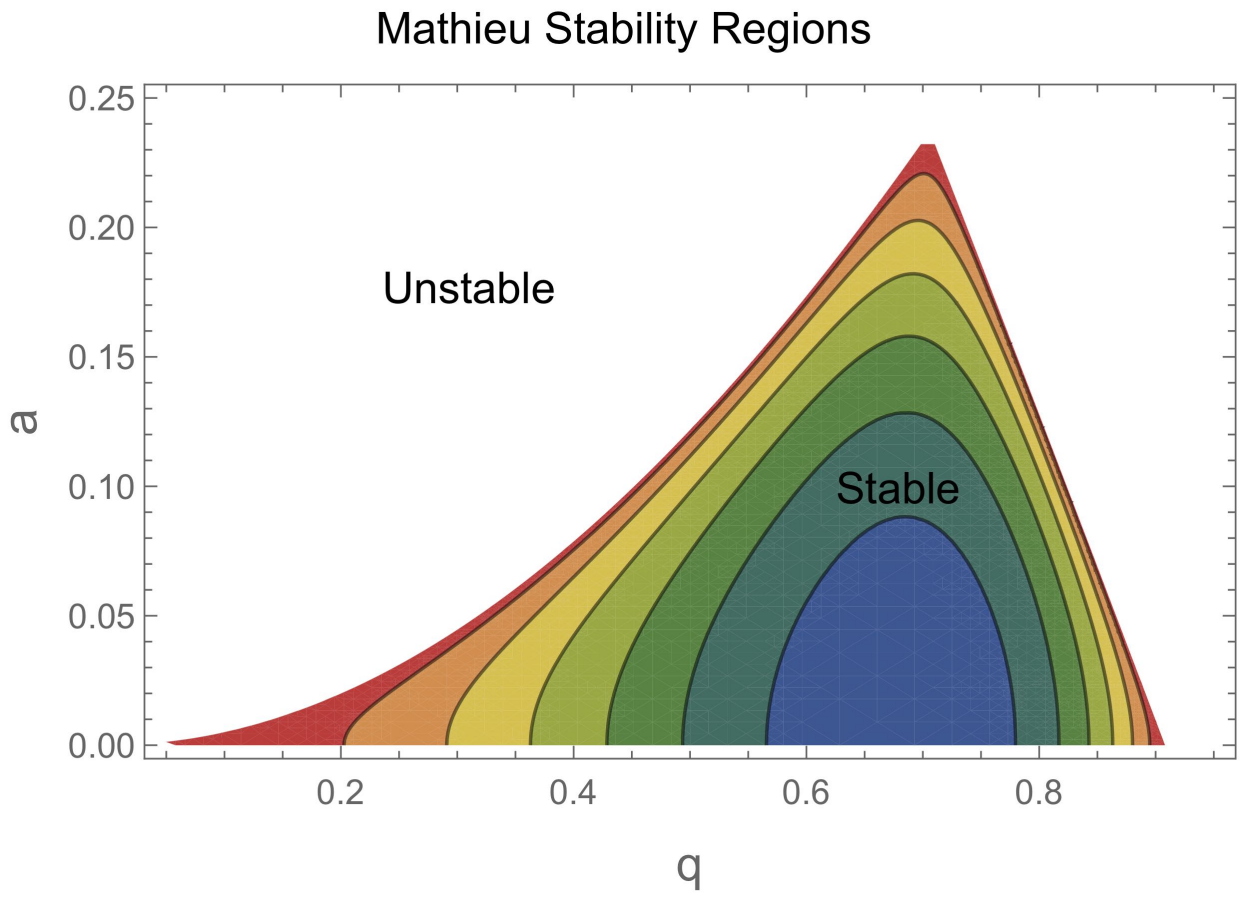

Figure 2.2: Mathieu stability regions in the a - q plane, ions will be effectively trapped if ions with the rainbow color region

The second term in the bracket of equation 2.19 represents the first-order micromotion which oscillates fast at frequency Ω_T, and its amplitude is proportional to the ion's average position x_0. Characterizing the micromotion can help increase the accuracy of several types of ion trap experiments. For example, the micromotion can have negative effects: it can lead to large systematic Doppler shifts in ion-based atomic clocks [61, 62], and it can greatly reduce the fidelity of the quantum gate[63, 64]. Within this pseudopotential framework, we can account for rf-driven micromotion by expanding the ions' motion around their equilibrium positions [22, 63]. To leading order, the coordinates of each ion vary in time as

$$\vec{r}(t) = \vec{r}^{(0)} + \vec{r}^{(1)} \cos(\Omega_t t) + \vec{r}^{(2)} \cos(2\Omega_t t) + \ldots \tag{2.22}$$

where $\vec{r}_0$ is the time-averaged ion position, $\vec{r}^{(1)} = (q_x\hat{x} + q_y\hat{y} + q_z\hat{z})r^{(0)}/2$ and $\vec{r}^{(2)} = (q_x^2\hat{x} + q_y^2\hat{y} + q_z^2\hat{z})r^{(0)}/32$ are the amplitudes of the first two micromotion terms.

So far, we have described confinement in the x-y plane. The linear Paul trap also provides axial (the z^2 terms in Φ_{dc}) confinement by adding voltages on the end-cap electrodes, we treat particles' motion as the secular motion with secular frequency ω_z as we discussed above. When we take the anisotropic factors χ and γ into consideration, the secular resonance frequencies in the radial and axial directions can be written as,

$$\omega_r \approx \omega_x \approx \omega_y \; ; \; \omega_x = \sqrt{\frac{Q}{m}\left(\frac{qV_0}{4d_0^2} - \frac{\kappa\chi U_0}{z_0^2}\right)}; \; \omega_y = \sqrt{\frac{Q}{m}\left(\frac{qV_0}{4d_0^2} - \frac{\kappa\gamma U_0}{z_0^2}\right)} \tag{2.23}$$

$$\omega_z = \sqrt{\frac{Q}{m}\frac{2\kappa U_0}{z_0^2}} \tag{2.24}$$

The Paul trap has a sharp transition from stable trapping to no trapping depending on the values of a_x and q_x. This gives us the Mathieu stability region (see Fig.2.2). From the a-q plane, we can select the space where the ions are confined in both directions simultaneously. Therefore, near the trap's center, the potential may be approximated as a harmonic pseudopotential well.

$$\Phi(\vec{r}) = \frac{1}{2}m(\omega_x^2 x^2 + \omega_y^2 y^2 + \omega_z^2 z^2) \tag{2.25}$$

2.4 Structural Phase Transition

Under the harmonic pseudopotential well, ions' structure configuration depends on the secular frequency in three directions. When the axial confinement is weaker than that in the radial direction, i.e., $\omega_z \ll \omega_r$, the ions tend to lie in a string along the z-axis. If we make the confinement stronger than the radial direction, ions will experience phase transition from string, zig-zag, and 3-dimensional cloud. If we push all ions along the axial direction, even more, all ions will fall into one plane and realize a two-dimensional (2D) crystal. [55, 65]. As shown in Fig. 2.3.

Confining ion crystals in one, two, or three dimensions require significantly different parameters to achieve each of these geometries. These parameters can be adjusted by selecting a reasonable trap size when designing the trap and also can change the applied voltages when we trap ions. Thus, trap designs optimized for holding 1D chains have proved incapable (or impractical) of confining ions in the radial-2D phase[66].

Under the pseudopotential approximation, this radial-2D phase is achieved when the trap aspect ratio $\alpha \equiv \omega_z/\omega_r$ satisfies the condition [49, 67, 55]

$$\omega_z/\omega_r > (2.264N)^{\frac{1}{4}} \tag{2.26}$$

hence, as mentioned in reference [49], a 100-ion system requires an axial frequency four times larger than the radial frequency. Increasing the dc endcap voltage can usually achieve a large axial frequency. However, from Eq.2.23, if the dc voltage is large compared with the rf voltage, this would make the radial frequencies imaginary, and ions shall not have bound trajectories. To achieve these stable 2D triangular configurations, the trapping voltage, frequencies, trap size, and ion crystal size must be carefully chosen. The details shall be talked about in Chapter three.

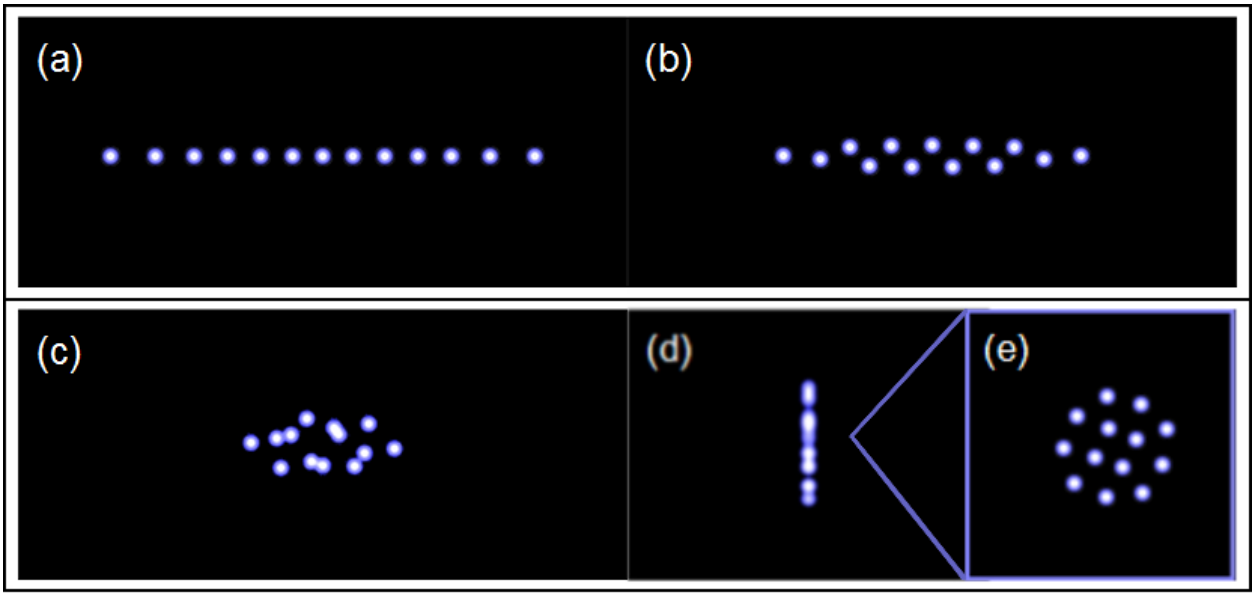

Figure 2.3: Crystals of 13 ions are shown for increasing values of the trap aspect ratio $\alpha \equiv \omega_z = \omega_r$. The structure transforms from a 1D chain (a) to zig-zag (b) and 3D spheroidal phases (c), before ending in a 2D triangular lattice in the radial plane (d). Panel (e) shows the front view of the 2D crystal with calculated all ion positions. Simulated ion sizes in (e) correspond to the diffraction-limited spot size of our imaging optics and include effects from rf-driven micromotion.

2.5 Dynamic Simulation of Ions Motion in the Crystal

The pseudopotential approximation doesn't include the effects of micromotion, which cannot be avoided in the 2D crystal with multiple ions. With the extracted secular trap frequencies from the finite-element simulation of the ion trap, we can apply the harmonic pseudopotential approximation to estimate the ion positions for large radial-2D crystals. For N trapped ions, take the coulomb interactions into account; the total potential energy depends on both the trapping potential as well as the Coulomb interaction between every pair of ions:

$$\begin{aligned} V(x,y,z) = &\sum_{n=1}^{N} \frac{1}{2} m(\omega_x^2 x_i^2 + \omega_y^2 y_i^2 + \omega_z^2 z_i^2) \\ &+ \frac{Q^2}{4\pi\epsilon_0} \sum_{i\neq j}^{N} \sum_{j}^{N} \frac{1}{\sqrt{(x_i - x_j)^2 + (y_i - y_j)^2 + (z_i - z_j)^2}} \end{aligned} \tag{2.27}$$

The equilibrium position of each ion can be found by simulating the full equations of motion with an added friction (cooling) term [51]. The results of one such calculation, for 17 ions, are shown in Fig. 2.4(b). After calculating the equilibrium positions, each ion's vibrational modes and micromotion trajectory can be computed by using the Floquet–Lyapunov transformation [68, 69]. This transformation can precisely solve N ions' normal modes and micromotion in a 2D crystal. And the potential energy of the ions in our Paul trap can be written as

$$\begin{aligned} V &= V_{trap} + V_{coulomb} \\ &= \sum_{i}^{n} \frac{1}{2}(\Lambda_x x_i^2 + \Lambda_y y_i^2 + \Lambda_z z_i^2) + \frac{1}{2}\sum_{i\neq j} \frac{q^2}{4\pi\epsilon_0}\|r_i - r_j\|^{-1} \end{aligned} \tag{2.28}$$

where $r_i = \{x_i, y_i, z_i\}$ is the vector coordinate of ion i, and the time-dependent trapping terms are given by

$$\Lambda_\alpha = B_\alpha + A_\alpha \cos(\Omega_t t),\ \alpha \in \{x, y, z\} \tag{2.29}$$

A_α, B_α represent the real trap electric potential coefficients. In Sec 2.3, we calculated the secular frequencies under the pseudopotential approximation, which may be expressed as

$$V_{pseudo} = \frac{1}{2}m\sum_{i}^{n}(\omega_x^2 x_i^2 + \omega_y^2 y_i^2 + \omega_z^2 z_i^2) \tag{2.30}$$

The total potential energy could then be written as

$$\begin{aligned} V &= V_1 + V_2 \\ &= (V_{pseudo} + V_{coulomb}) + (V_{trap} - V_{pseudo}) \end{aligned} \tag{2.31}$$

Treating V_2 as the perturbation, we expand the time-dependent positions $\{R_{i,\alpha}(t)\}$ around the minimum-configuration locations $\{R^0_{i,\alpha}\} = (x_1^{(0)}, y_1^{(0)}, z_1^{(0)}, \ldots, x_N^{(0)}, y_N^{(0)}, z_N^{(0)})$ that are obtained from the secular part of $V_1 = V_{pseudo} + V_{coulomb}$. The time-dependent positions can then be written

in terms of the normal modes S_j by setting

$$R_{i,\alpha}(t) = R^0_{i,\alpha} + r_{i,\alpha} = R^0_{i,\alpha} + \sum_j^{3N} \Gamma_{i,j} S_j(t) \tag{2.32}$$

where $\Gamma_{i,j}$ are the matrix elements of the normal mode vectors, with rows indexed by the N ions i in the three directions α, and columns indexed by the $3N$ normal modes j.

We then plug Eq. 2.32 into Eq. 2.31, write the potential in terms of the normal modes, and keep the first two terms:

$$\begin{aligned} V &= \frac{1}{2}\vec{S}^T \Lambda \vec{S} + \sum_{i,\alpha}^{N} (\Lambda_\alpha - \frac{1}{2} m\omega_\alpha^2)(R^0_{i,\alpha} + \sum_j^{3N} \Gamma_{i,j} S_j)^2 + \dots \\ &\approx \frac{1}{2}\vec{S}^T \Lambda \vec{S} + ((\vec{R}^0)^T + \vec{S}^T \Gamma)(W_1 + W_2 cos\Omega t)(\vec{R}^0 + \Gamma^T \vec{S}) \end{aligned} \tag{2.33}$$

where $\Lambda = \text{diag}\{\Omega^2_{i\alpha}\}$, $W_1 = \text{diag}\{B_\alpha - \frac{1}{2} m\omega_\alpha^2\}$, $W_2 = \text{diag}\{A_\alpha\}$, and Ω_i is the ith normal frequency in α direction. The linearized equation of motion derived from Eq. 2.33 is

$$mS'' + (\Lambda + J) \cdot S + P + (L + Y \cdot S) \cos \Omega t = 0 \tag{2.34}$$

where

$$\begin{aligned} \vec{P} &= \Gamma \cdot W_1 \cdot \vec{R}^0 + (\vec{R}^0)^T \cdot W_1 \Gamma^T \\ \vec{L} &= \Gamma \cdot W_2 \cdot \vec{R}^0 + (\vec{R}^0)^T \cdot W_2 \Gamma^T \\ J &= \Gamma \cdot W_1 \cdot \Gamma^T + (\Gamma \cdot W_1 \cdot \Gamma^T)^T \\ Y &= \Gamma \cdot W_2 \cdot \Gamma^T + (\Gamma \cdot W_2 \cdot \Gamma^T)^T \end{aligned} \tag{2.35}$$

Let

$$\begin{aligned} A &= (\Lambda + J)\frac{4}{\Omega^2 m} \\ Q &= -\frac{1}{2}Y\frac{4}{\Omega^2 m} \\ \vec{G} &= -\vec{P}\frac{4}{\Omega^2 m} \\ \vec{F} &= -\frac{1}{2}\vec{L}\frac{4}{\Omega^2 m} \end{aligned} \tag{2.36}$$

We then have a simplified inhomogeneous Mathieu Matrix Equation from Eq.2.34

$$\vec{S}'' + (A - 2Q\cos\Omega t)\cdot\vec{S} = \vec{G} + 2\vec{F}\cos\Omega t \tag{2.37}$$

where F and G are $3N$-component constant vectors. We assign the basic π periodic solution $\vec{S} = \sum_{-\infty}^{\infty}\vec{B}_{2n}e^{i(2n)t}$ in the equations of motion (Eq. 2.37) to obtain

$$\begin{gathered} (A - 4n^2)\vec{B}_{2n} - Q(\vec{B}_{2n-2} + \vec{B}_{2n+2}) = \\ \vec{G}\delta_{1,n} + \vec{F}(\delta_{n,1} + \delta_{n,-1}) \end{gathered} \tag{2.38}$$

By defining $C_{2n} = A - 4n^2$ and using $B_{2n} = B_{-2n}$, we can write infinite recursion relations for $\vec{B}_{2n}$,

$$A\vec{B}_0 - 2Q\vec{B}_2 = \vec{G} \tag{2.39}$$

$$C_2\vec{B}_2 - Q(\vec{B}_0 + \vec{B}_4) = \vec{F} \tag{2.40}$$

$$C_{2n}\vec{B}_{2n} - Q(\vec{B}_{2n-2} + \vec{B}_{2n+2}) = 0, (n \geq 2) \tag{2.41}$$

Eq. 2.41 immediately gives a recursion relation in the form of Eq. 2.37, which allows us to get the infinite inversions expression

$$\vec{B}_4 = T_2 Q\vec{B}_2 \tag{2.42}$$

where

$$T_2 = [C_4 - Q[C_6 - Q[C_8 - ...]^{-1}Q]^{-1}Q]^{-1} \tag{2.43}$$

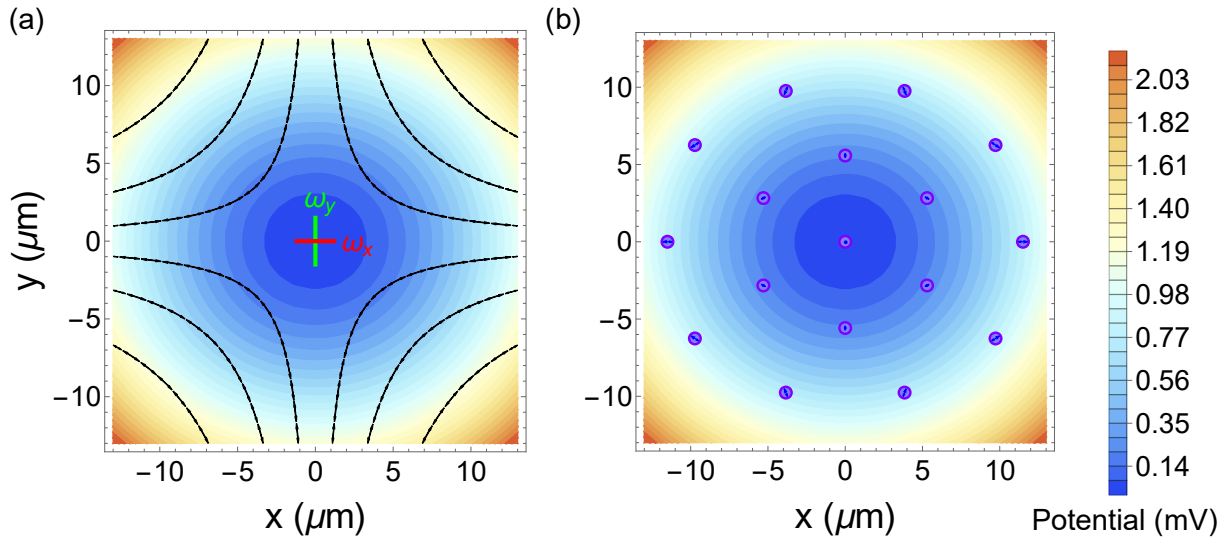

Figure 2.4: (a) The radial trapping potential for our open-endcap geometry, calculated using finite-element simulation methods. The two radial frequencies are made slightly non-degenerate to prevent the rotation of the ion crystal. The associated electric field lines are shown in black. (b) Simulated equilibrium ion positions for 17 $^{171}Yb^{+}$ ions in the potential of (a). Ions away from the central axes experience driven micromotion, whose amplitude can be calculated using the Floquet-Lyapunov transformation. For the 17-ion crystal, these amplitudes (shown as small arrows in (b)) are predicted to be small compared to the inter-ion spacing.

Substituting Eq. 2.42 into Eq. 2.39 and 2.40 we obtain the linear system

$$\begin{pmatrix} A & -2Q \\ -Q & R_2 - QT_2Q \end{pmatrix} \begin{pmatrix} \vec{B}_0 \\ \vec{B}_2 \end{pmatrix} = \begin{pmatrix} \vec{G} \\ \vec{F} \end{pmatrix} \tag{2.44}$$

which can be solved to find the coefficients of the normal modes $\vec{S}$, and the micromotion terms $\vec{r} = \Gamma^T \cdot \vec{S}$.

The first-order micromotion is described by the term $\vec{B}_2$, which to first-order scales linearly as the ions' radial distance from the trap center, and the following micromotion terms are $\vec{B}_4$ and so on. Fig.2.4s shows the radial trapping potential and the amplitude of the moicromotions, and the small arrows in Fig. 2.4(b) show the resulting micromotion amplitude for the off-axis ions.

The ions fluctuate around the equilibrium when there is a slight deviation from their equilibrium positions. The ions oscillate in complex patterns most of the time, but every oscillation of the system

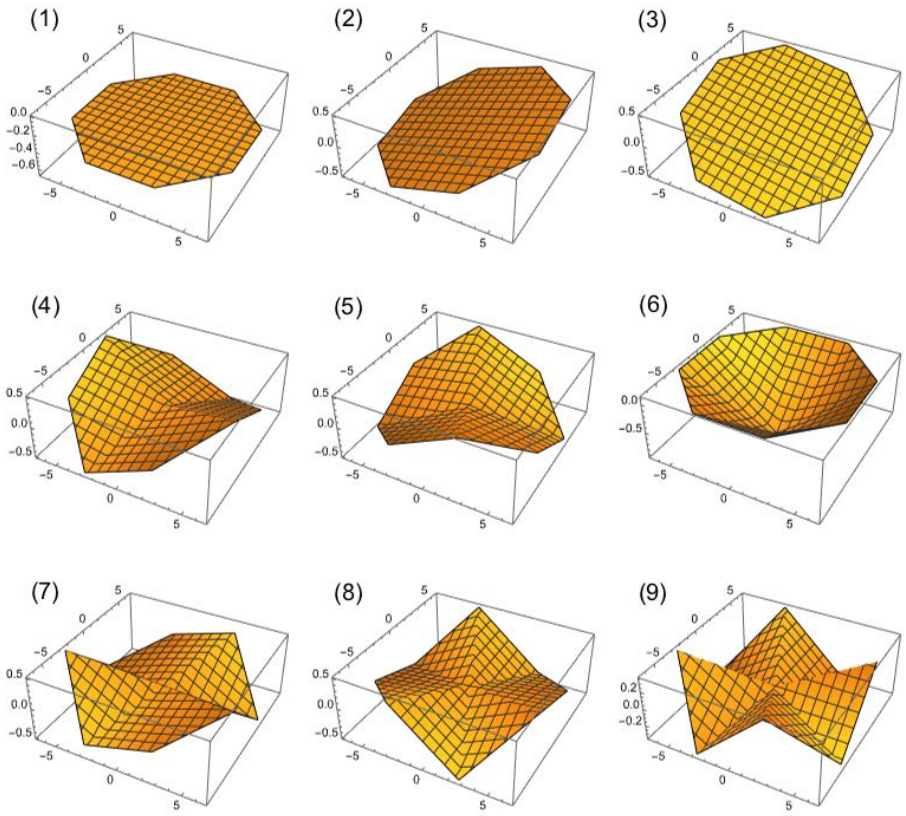

Figure 2.5: Normal modes of 9 ions, (1) is the center of mass mode(COM), and (2-9) are other normal modes.

(with small amplitudes) can be Fourier decomposed into a group of vibrational modes known as the normal modes of vibration. In a radial 2D crystal, quantum simulation cares about the transverse mode, which is defined as along the z-axis(axial direction). The Ising interaction is coupled with the normal mode eigenvector components between qubit pairs[70]; each mode makes a contribution to the interaction. With secular frequency $\omega_x = \omega_y = 0.47$MHz and $\omega_z = 1.15$ MHz, the calculation of 9 ions' transverse modes is shown in Fig.2.5, the highest-frequency mode is the center-of-mass motion, with eigenvector $1/N[1, 1, 1 \ldots 1]^T$, eigenfrequency ω_z. The next lower frequency mode is the tilt mode, and the last one is the zig-zag mode.

CHAPTER 3

Radial-2D Ion Trap Design and Experimental Hardware

3.1 Segment Blade Paul trap

The primary design challenge for trapping crystals in the radial-2D phase is to choose the appropriate trap dimensions, voltages, and frequencies that ensure Eq. 2.26 is strongly obeyed for large numbers of ions while keeping all parameters experimentally reasonable.

The principles that guide the radial-2D crystal trap design may include several parts: first, we have to make our trap parameter satisfy the equation 2.26, it can be most easily accomplished by substantially increasing ω_z while keeping ω_r constant, it would require large U_0 and/or small z_0. However, we need to keep the voltage within the tolerance range of the experimental conditions; thus, a more appropriate way is to choose a smaller z_0 in the process of designing the trap. Second, large U_0 and small z_0 have a deconfining effect in the radial direction, the second term $\kappa\gamma U_0/z_0^2$ of equation 2.23 grows too large, ω_r become an imaginary number, the ions will escape from the trap. Third, to counter the effect of deconfining, V_0 must also be moderately large while keeping d_0 small. Fourth, the micromotion effects of the trapped ions depend on the trap-driven frequency Ω_T;a relatively large driven frequency can keep the Mathieu q parameter which depends on the driven frequency, small. In conclusion, these observations lead to a set of self-consistent design choices: small trap dimensions d_0 and z_0, large dc voltage U_0, moderately large rf voltage V_0, and relatively large trap frequency Ω_T.

A regular rod trap doesn't have the ability to shrink its dimension size because it would make the electrical circuit design to be hard, and a tiny rod cannot mimic the potential produced by the

hyperbolic shape electrode. Thus a segment-blade design for our linear trap Paul trap is a good choice, and there are several advantages of this trap geometry:

1). The open endcaps of the blades ensure that imaging is possible perpendicular to the 2D ion plane;

2). The trap dimensions d_0 and z_0 can be made relatively small to avoid unreasonably high voltages V_0 and U_0;

3). There is no compromise between the numerical aperture (NA) of the imaging optics and the trap size. In this type of trap, the angle-designed edges of the rf and dc blades ensure that there are no obstructions to the light collection. We calculated our NA = 0.24 by using an imaging objective (Special Optics 54-17-29-369 nm)

4). The design must incorporate electrodes to compensate for stray dc fields at the trap center. These compensation electrodes should not be too close to the trap volume to avoid distorting the trap field. At the same time, they must be near and large enough to produce a sufficiently dc field at the trap center to push ions. What's more, optical access must be taken into consideration.

Micro-fabricated, gold-coated blades are a popular choice for constructing ion trap electrodes [71, 72]. We requested the company Translume Inc to help us design gold-coated blades with really high precision. However, during the experiment, we found the gold coating on such electrodes is often susceptible to damage from resistive heating or large electric fields which arise during the operation of the trap[73]. For instance, tests in our lab demonstrated that the large rf voltages required for creating the radial-2D crystal phase quickly led to the melting and evaporation of the gold layer. This irreversible damage also happened in Wesley C. Campbell's group [74] with the same technology from the Translume, as we can see in the right graph of Fig.3.1.

We fabricated our electrodes from solid tungsten to ensure more robust performance in the presence of large rf voltages. Tungsten is a readily available, strong, and low resistivity metal that has been used in a variety of earlier rf traps [75, 76]. Compared with more common metals (such as stainless steel), we consider tungsten advantageous for our trap since its low resistivity will limit blade heating, and any associated vacuum pressure increases when large rf voltages are applied.

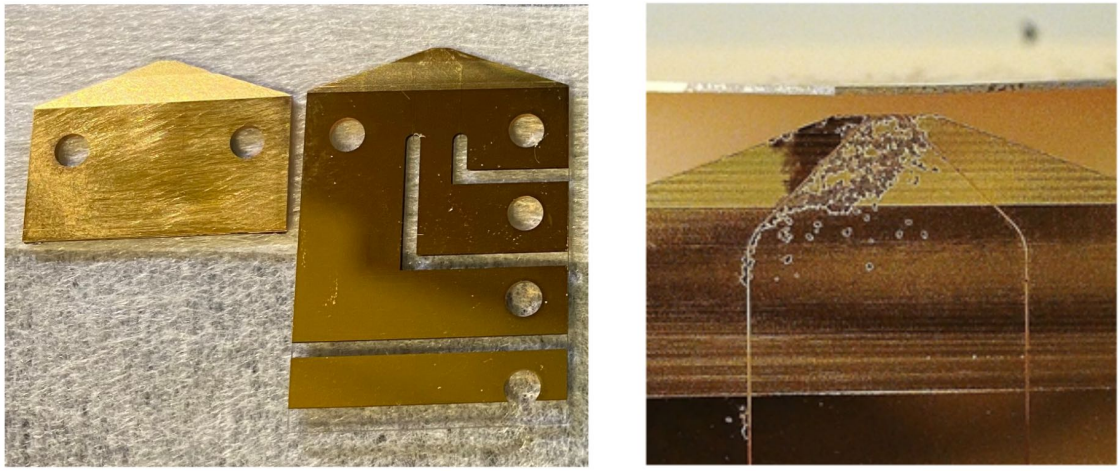

Figure 3.1: The left graph shows the Gold-coated blades, the right graph zooms in on the region of the blade tip, and the golden coating melt on the glass surface.

The SOLIDWORKS 2013 is the software we use to create models and assemblies. This software is an easy-to-use parametric design modular in which we can easily edit the design at any stage in the design process, look at each part of the design, see natural mass properties, and check for interference. We don't need to build/manufacture the product before we see any errors. Following the design guidance above, each trap segment's specification is listed in Fig. 3.3. The units of the numbers on the graph are imperial. We may trap ions with 14 V on the dc electrodes and 150 V on the rf electrodes. Thus the safety margin as the overall set-up (including electrical feed-throughs) is designed to allow for voltages up to 500 V. We isolate the blades with the stainless steel frame by the Macor, which is a machinable glass-ceramic; there are thread inserts on each tapped hole of Macor pieces to ensure a stable and fixed connection between blades and Macor parts, the specification is shown in Fig. 3.2.

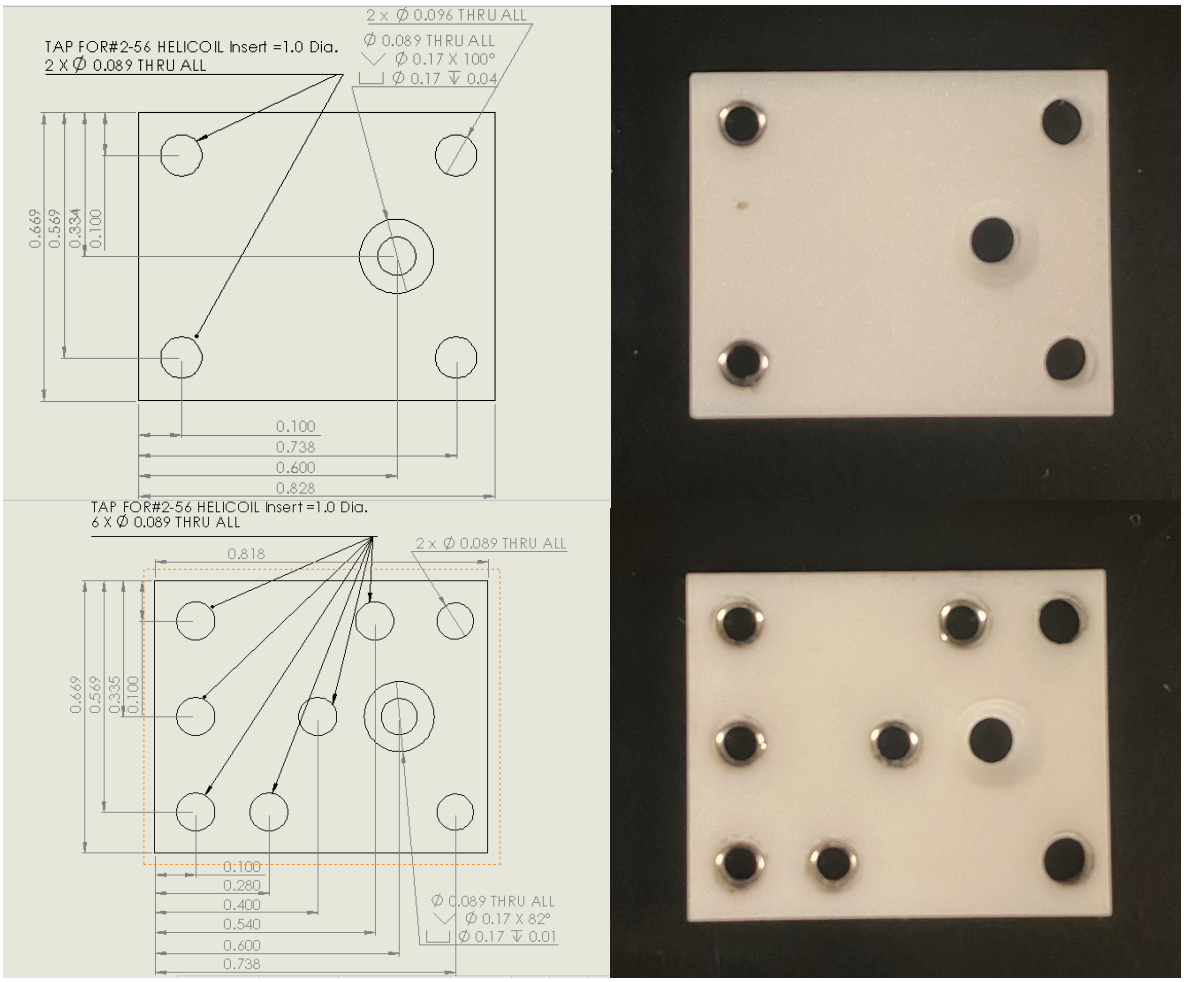

Figure 3.2: Geometry of the Macor pieces, number units are in Inches

Fig. 3.3 (the SOLIDWORKS file) shows the geometry of the blade trap. The trap is segmented into two pairs of blades – dc blades and rf blades. The rf blade is a whole piece of the electrode with a tip length of 1mm and thickness of 100 μm. The dc blade includes three different types of electrodes—two endcap electrodes and one rf ground electrode whose tip thickness is 100 μm, and the total length of three electrodes plus the gaps is 1 mm. The rf blades are continuous and of the same full length as the three dc blade segments. The side view in Fig. 3.3 gives the overall look of the 2D trap, all blades are well aligned and form a 200 μm by 200 μm by 1 mm trap space (they are variables based on the size of the actual trap, we can adjust they once we get the real dimensions). The trap provides transnational symmetry for the rf potential and all blades can be dc biased to

allow for translation along all principal axes. We also add two additional rods (we can also see them in the "front view" of Fig.3.3) with voltage compensation along the vertical/horizontal directions, which can help us translate and shape the crystal.

3.2 Finite-Element Simulations

We discussed the general ion trap theory in sections 2.1 and 2.2. The specific blade trap we use has to do the simulation to help us make the experiment prediction. Trapping ions in the radial-2D crystal phase needs a delicate balance between the voltages applied to the electrodes as shown in equation 2.4 and the geometry of the trap. According to the design requirement, the specificity of our 2D ion trap is listed below, $d_0 = 23 \ \ \mu m$, $z_0 = 200 \ \ \mu m$, $U_0 = 14.4 \ \ V$, $V_0 = 150 \ \ V$, and $\Omega_T = 2\pi \times 27.51$ MHz. And the geometric factor κ and anisotropic factor χ and γ also influence this subtle balance. Since the different traps have different κ due to the trap geometry and fabrication, and blade style electrodes are not perfect hyperbolas (for which $\kappa = 1$). Consequently, performing numeric simulations to determine the secular trap frequencies and normal modes and ensure stable trapping in the radial-2D region.

COMSOL Multiphysics is used to carry out the calculations of the potential of various trap configurations. We set up the boundaries and materials for our blades and import the 3D file we created with SOLIDWORKS. The goal of the simulation is to develop a number of basis functions that compare each electrode's electric potential at 1 V to that of the other electrodes at ground potential. The total trapping potentials can be calculated by adding these potentials (or electric fields) and weighting them based on the applied voltages. The rf pseudopotential field is computed from the electric field with both rf rails at 1 V, and they must be done for each DC and rf electrode (if the rf rails can have a DC bias applied).

With the basis function extracted from the COMSOL, we can calculate the effective potentials $\phi_{dc}(\vec{r})$ and $\phi_{rf}(\vec{r})$ which arise from the application of 1 Volt to each individual electrode (with the others grounded). The total potential near the center of our trap can be written in the form

$\Phi_{tot}(\vec{r},t) = \Phi_{rf}(\vec{r},t) + \Phi_{dc}(\vec{r})$, where the rf contribution is given by:

$$\begin{aligned}\Phi_{rf}(\vec{r},t) &= V_0\cos(\Omega_t t)\phi_{rf}(\vec{r}) \\ &= V_0\cos(\Omega_t t)(\eta^x_{rf}x^2 + \eta^y_{rf}y^2 + \eta^z_{rf}z^2)\end{aligned} \tag{3.1}$$

and the dc component is:

$$\Phi_{dc}(\vec{r}) = U_0\phi_{dc}(\vec{r}) = U_0(\eta^x_{dc}x^2 + \eta^y_{dc}y^2 + \eta^z_{dc}z^2) \tag{3.2}$$

Where the factors η^α in Eqs. 3.1 and 3.2 indicate the curvatures in the α direction for the rf and dc potentials. Comparing these equations to the form of Eq. 2.1, the geometric factor can be extracted as $\kappa = z_0^2\eta^z_{dc}$ as well as the anisotropic factors $\chi = -2z_0^2\eta^x_{dc}/\kappa$ and $\gamma = -2z_0^2\eta^y_{dc}/\kappa$. The resulting trap potential, along with its associated electric field, is shown in Fig. 2.4(a). The action of this simulated potential $\Phi(\vec{r},t)$ gives rise to time evolution described by the Mathieu equations 2.15, with the dimensionless parameters $a_i = 8QU_0\eta^i_{dc}/m\Omega_t^2$, $q_i = -4QV_0\eta^i_{rf}/m\Omega_t^2$, where $i \in \{x,y,z\}$. Under the pseudopotential approximation, which is valid when $a_i < q_i^2 \ll 1$ (for our case, $a \sim 0.002$ and $q \sim 0.08$ in the x and y directions), the ion secular frequencies are then defined by $\omega_i = \beta_i\Omega_t/2$, where $\beta_i \approx \sqrt{a_i + q_i^2/2}$ are the characteristic exponents of the Mathieu equation as we talked in the equation 2.21 [51, 22]. From this way, we extracted the secular trap frequencies ω_i where $i \in \{x,y,z\}$. Once we get the secular frequencies, based on Section 2.5, the micromotion and Normal mode can be calculated.

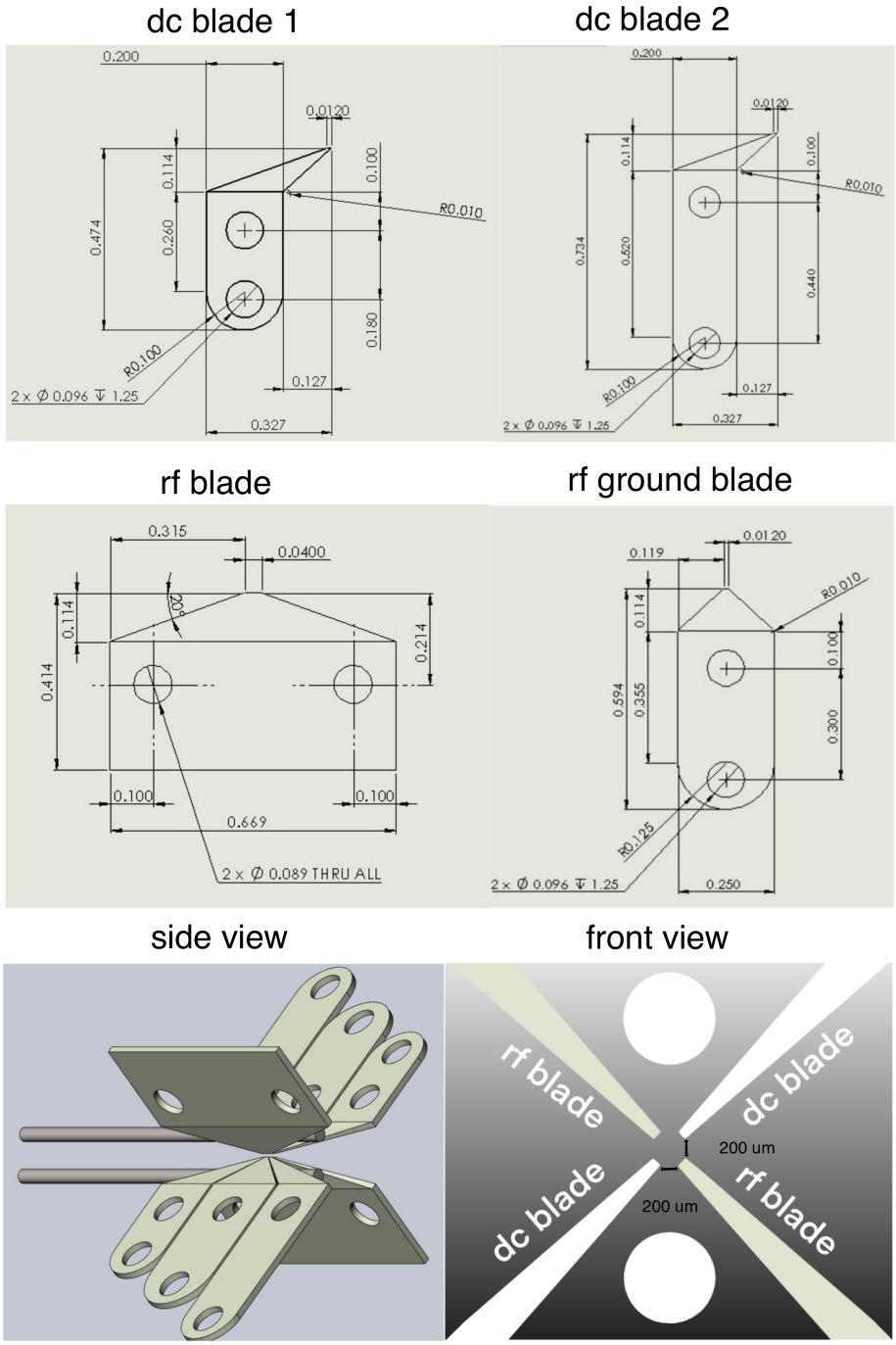

Figure 3.3: Geometry of the blade trap, number units are in Inches

3.3 Blades fabrication

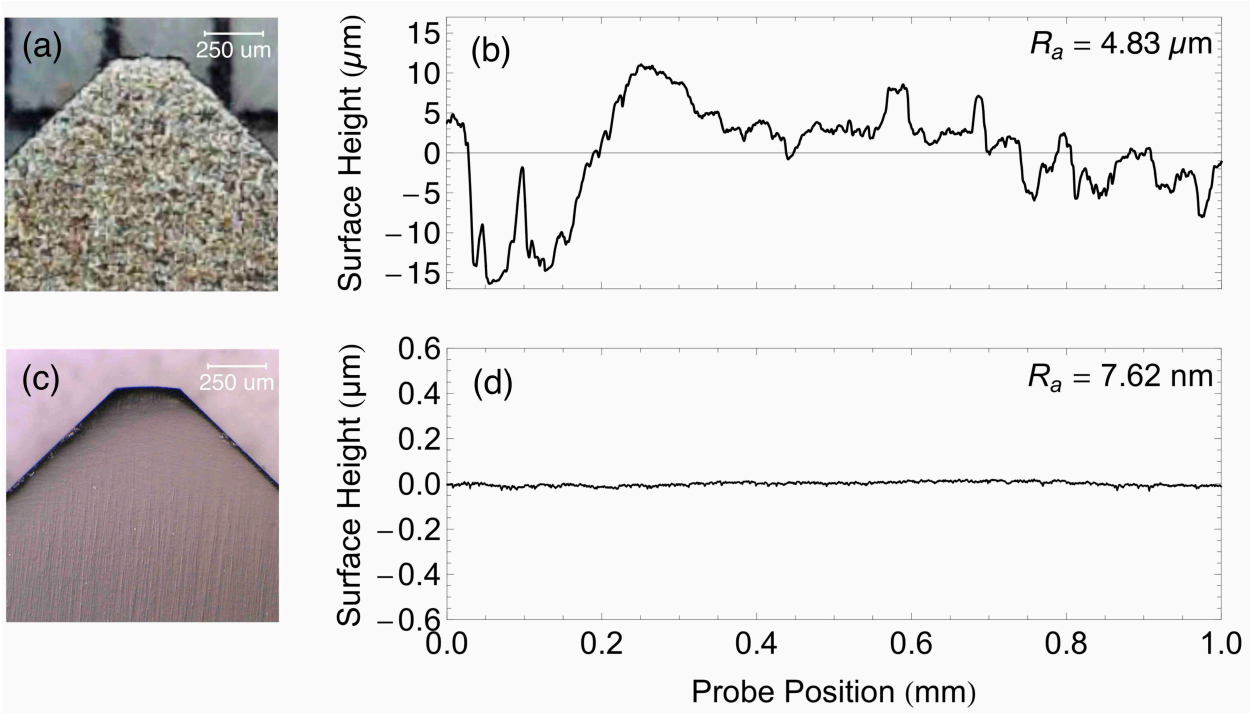

Figure 3.4: (a) Image of a blade electrode directly after wire-EDM machining. (b) Using a stylus profilometer near the blade's tip, we characterize the average surface roughness R_a. (c) After electropolishing and hand polishing, the blade has a smooth mirror-like surface. (d) Nearly three orders of magnitude reduce the surface roughness of the polished blade compared to the unprocessed blade.

Electrodes fabrication is an essential step for a functional ion trap. A smooth electrode surface can limit the stray electrical field, and a shiny surface helps reduce diffuse reflection from the laser to the imaging system. The blade electrodes are fabricated from a sheet of 500 μm-thick pure tungsten using a wire-cut EDM (Electrical Discharge Machining) process. This technique allows reasonably complex electrode geometries (such as the segmented dc blades) to be machined within $\sim$ 10 μm tolerances. This technique is suitable for making tools from hardened steel. The tool electrode in wire EDM is simply a wire. The wire is wound between two spools so that the active part of the wire is constantly changing to avoid erosion of the wire, causing it to break. The finished surface after wire-cut EDM can be finely controlled.

In our design, the three dc blade segments are each 300 μm long and separated by a 50 μm

gap; the total length of the rf blade is around 1 mm. The final processed tip thickness is 100 μm for all blades. The exposed surface following wire-cut EDM processing can be markedly rough for sintered materials like tungsten. This can be problematic for trapped-ion systems since there is evidence in the previous paper that large surface roughness could significantly affect motional heating rates [77, 78, 79, 80]. Moreover, rough electrode surfaces could increase unwanted laser beam reflections, increase the background light collected by the imaging optics, and increase the random noise when we detect ion's signal when we do an experiment. Thus, we target an initial 300 μm tip thickness during wire-EDM machining. Fig. 3.4(a) shows an image of a blade electrode just after wire-EDM machining. Using a stylus profilometer (Bruker DektakXT), we characterized the arithmetic average surface roughness R_a of this blade to be approximately 5 μm over a 1 mm region near the tip as shown in Fig. 3.4(b).

To smooth the tungsten blade surface after machining and also decrease the thickness of the blade tip to our target 100 μm, we implement a two-stage polishing process.

1). We use self-terminated electrochemical etching to remove the most significant surface features [81], as well as to erode most of the thickness of the blade tip. A typical experimental procedure is described as follows. A sodium hydroxide solution is used to pre-clean the surface of the tungsten blade. We adjust the length immersed in the solution so that it is a little longer than the desired length of the electrode tip. The blade is carefully positioned so that it is perpendicular to the solution surface, with a distance between the cathode and anode (blade) is 4 cm. The blade is immersed in sodium hydroxide solution (NaOH, 400 ml of 2 mol/L) and connected to the cathode of a power supply (10 V, 1.5 A) for 2 minutes of etching. This process lowers the surface roughness to $R_a < 1$ μm and reduces the tip thickness from 300 μm to $\sim$ 100 μm. After etching, the blade is taken out and washed with distilled water before being kept in an argon gas box to protect the electrode's freshly etched surface from oxidation by the argon gas. (People should be careful if they want to repeat this process, a high concentration of NaOH is dangerous, please avoid contacting the chemical with eyes, skin, and clothing when doing the electrochemical etching).

2). Following that electropolishing stage, the electrodes are hand-polished using 3 μm, 1 μm, and 0.3 μm stages of Aluminum Oxide polishing paper. This process can remove the small bumps on the surface and polish the surface like a mirror. A mirror surface is helpful to reduce the background noise (mainly from the laser), reflecting the light in a certain direction that will not accept by our image system. Fig. 3.4(c) shows an image of the blade electrode after processing. As measured by a profilometer, the surface roughness is reduced from $R_a \approx 5$ μm to $R_a \approx 8$ nm after these polishing processes (Fig. 3.4(d)).

3.4 Trap Assemble

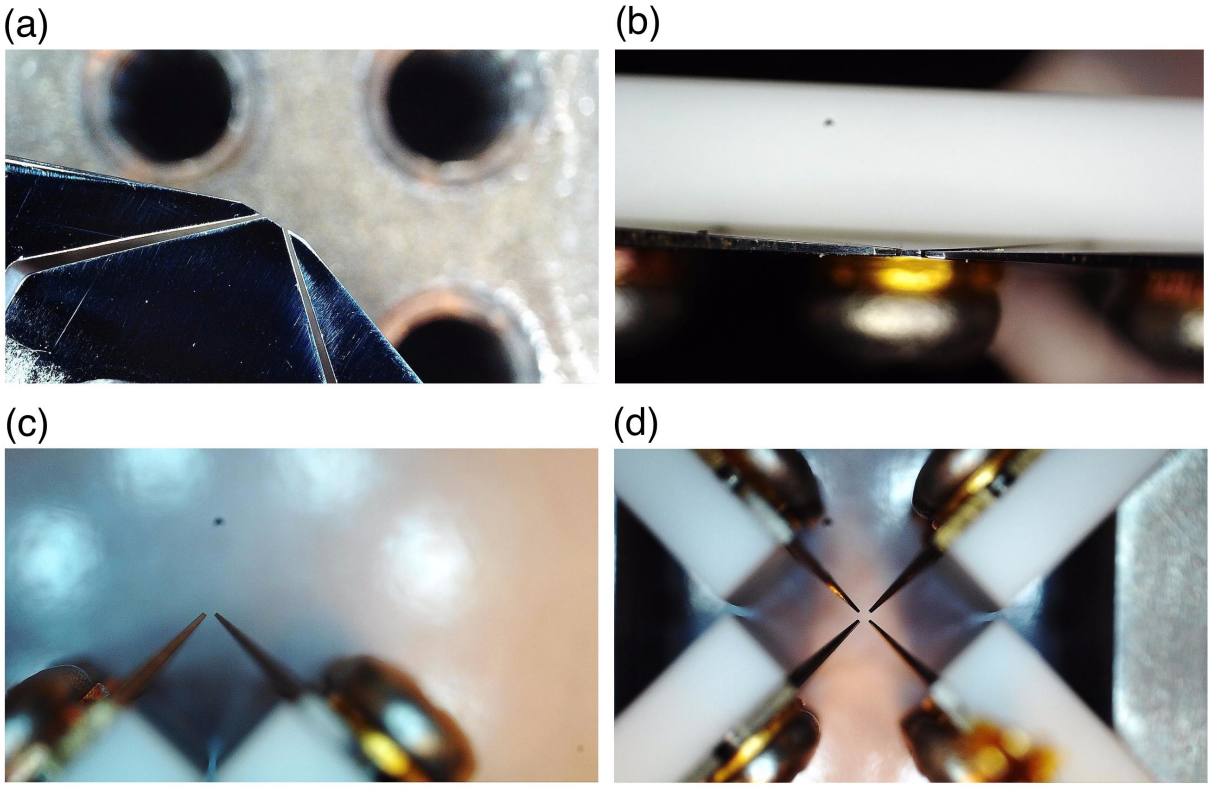

Figure 3.5: (a) The dc blade piece alignment. (b) top view of the dc blade piece. (c) align the height of the dc blade piece and rf blade. (d) an image of the trap center after alignment.

The trap is assembled in a clean room to avoid dust contamination. The blades are mounted on

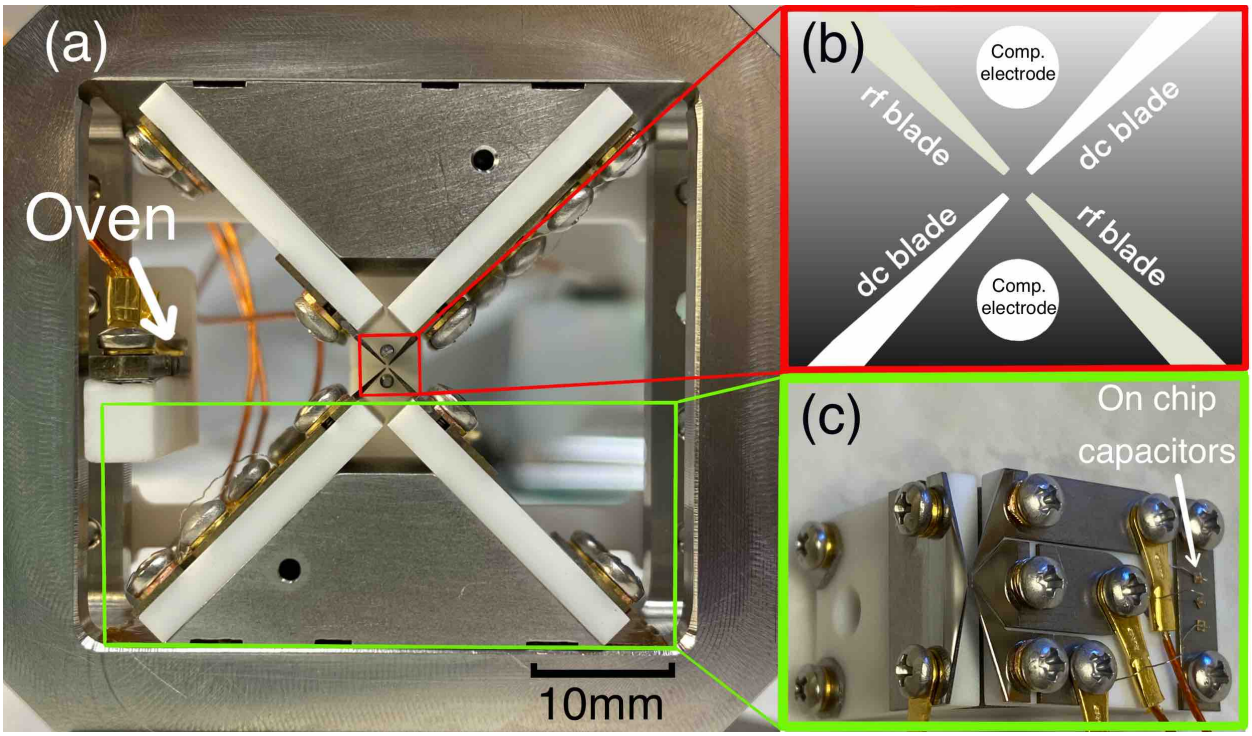

Figure 3.6: Assembled blade trap mounted in its vacuum chamber, taken along the imaging direction. The blades are mounted on insulating macor plates, which are fastened to a stainless steel frame and support structure (connected to the ground). ^{171}Yb and ^{174}Yb ovens are placed to the left of the trap. (b) Sketch of the blade configuration near the trap center. Rf and segmented dc blades provide the trap potentials; two rod-style electrodes provide compensation in the vertical/horizontal directions. (c) Image of an rf blade and segmented dc blade mounted on their macor supports. Blades are machined from a 500 μm-thick piece of solid tungsten and polished after machining. On-chip capacitors (800 pF) on each dc segment provide filtering of rf pickup.

Macor plates fastened to trapezoidal stainless-steel blocks. The dc segments are hand-aligned under a microscope to keep a 50 μm gap between segment(Fig. 3.5(a)), and Fig.3.5(b) shows the top view of the dc segment. The rf blade is mounted parallel to the dc segments with a gap of 280 μm (Fig. 3.5(c)), and the tips of the two segments are at the same height. Two assembled triangular blocks are placed in a stainless-steel frame in a vertex-to-vertex orientation, with a vertical gap between blades of 300 μm (Fig. 3.6(a)). All dc electrodes are mechanically connected to gold-plated lugs, which are crimped to Kapton-coated wire and connected to Sub-C 9-pin feedthrough. The rf blades and atomic ovens connect with separate high-power electrical feed-throughs. The final view of the trap is shown in Fig. 3.6 a. We insert the trap in the main Chamber (cube chamber) of our vacuum system. The trap center is located 11.5 mm away from the front windows. It would give a relatively

large solid angle for EMCCD (Electron Multiplying Charge Coupled Device) camera imaging ions.

3.5 Ultra-High Vacuum System

The ion trapping experiment requires Ultra-high Vacuum (UHV) to reduce the background gas collisions, which can heat the trapped ions by transferring energy during an elastic collision. A conservative estimate for the heating rate can be given by the total collision cross section[22]

$$\sigma_{elastic} = \pi\Gamma(1/3)[\frac{\alpha q^2}{16\epsilon_0\hbar\nu}]^{2/3} \tag{3.3}$$

where α is the polarization ability from the ions' electrical field to the neutral background. ν and q are the relative velocity of the pair and charge. When the pressure on the order of 10^{-11} Torr, the collision rate of the background gas is estimated $\gamma \approx 0.03\ \ s^{-1}$. Although a large amount of energy will transfer to the ions from each collision, the average energy from the whole collision event is small due to it rarely happens under the UHV pressure, and ion lifetimes in the trap can last from a few hours to a few days.

We used Conflat Flange hardware, the UHV-compatible bakable seal, to prevent the slightest leakage. Any operations on the vacuum hardware must be careful to avoid damage to the knife edge of the Conflat Flange. A small notch on the knife edge means the whole part is scrapped. Acetone and isopropyl alcohol ultrasonic pre-cleaning is required for all vacuum parts. Gloves must be worn for all operations, any remaining organic components, such as oil contamination or fingerprints, will continue to outgas and prevent reaching UHV levels after our cleaning process. Pre-baking vacuum components can accelerate the pumping process, creating a chromium oxide layer that stops water from diffusing from the vacuum components' surface. The procedure to prepare the vacuum parts includes these steps:

1). Ultrasonic cleaning of all parts is submerged in acetone for 1 hour.

2). Replace the Acetone with the Iso-propyl alcohol and repeat step 1.

3). Wipe all residual liquid with Kimwipers.

4). Wrap all parts with aluminum foil and pre-bake them at under 240 degree Celsius for two days (Only stainless steel components need to be pre-baked).

Step 1 removes the organic contamination on the surface and shakes the dust off the vacuum parts; step 2 removes the acetone that remains on the surface; pre-bake on step 4 will evaporate part of the water stored in the stainless steel lattice and form a chromium oxide layer on the inner surface. All vacuum components will store in a clean and safe place to prevent damage and contamination.

Typically, vacuum components containing stainless steel need to be cleaned and pre-baked, but we must carefully treat viewports with surface coatings. The viewports shipped from the manufacturer are pretty clean. We don't need to clean and pre-bake them. However, if these viewports are contaminated and need to be cleaned, follow the Thorlabs "Handling and Cleaning Procedures for Optical Components" procedure to prevent removing the anti-reflective coatings on the glass surface.

3.6 Vacuum Hardware

3.6.1 TPS Pump

UHV system needs a High-speed pump — possibly multiple vacuum pumps in series and/or parallel. The primary vacuum pump for a UHV system we used is Agilent Technologies TPS bench which embeds an 80 L/s turbo pump for operation down to 0.75×10^{-8} Torr. We also have a backup pump called Agilent Technologies TPS Mini (embeds 70 L/s turbo pump for operation down to 0.75×10^{-8} Torr). The TPS bench includes the scroll pump and a series of turbo pumps. The scroll pump initials the Chamber to 1×10^{-2} Torr; then, the turbo pump starts to work at full power and lowers the pressure to 10^{-8} Torr. All operations must be isolated from oil, any type of oil would contaminate our vacuum system and destroy the TPS pump.

3.6.2 Ion Pump

Ultra-high vacuum (UHV) is the vacuum regime characterized by pressures lower than about 10^{-11} Torr. To reach that pressure, the vacuum system needs another high-speed pump — an ion pump (the Agilent VacIon Plus 20 pump, P/N: 9115036). The ion pump works when the whole chamber is roughed to 10^{-7} Torr, it has two powerful ferrite magnets, which will create a high magnetic field (1200 Gauss) inside the vessel. The free electrons get pulled towards the anode inside but get caught in the magnetic field and rotate around it due to the Lorentz force, and the electrons get trapped in this motion until they hit something. With so many moving electrons, they are bound to hit a gas molecule, then ionizes them and create a positively charged molecule within the positive anode tube. The positively charged molecule accelerates towards the cathode at high velocity and then hits a grounded surface of the highly reactive sputtered material(like a titanium plate), and these molecules will chemically combine the titanium; for example, if the molecule is oxygen, it will create titanium oxide (TiO), from this way, the ion pump trapped most residual molecules and lower the pressure to UHV level.

3.6.3 Non-evaporable Getter

Most vacuum systems select stainless steel as the material of their chamber body; although the vacuum components are cleaned and form a chromium oxide layer on the inner surface, we still cannot remove the minor molecular gases stored in the body of vacuum components, such as hydrogen. Unfortunately, the ion pump is not sensitive to these minor molecular gases; as time goes on, the hydrogen will enter the vacuum system, making it difficult for the pressure to drop, causing a high collision rate. Non-evaporable getter (NEG, CapaciTorr-D 400-2 Pumps) helps to establish and maintain vacuums by soaking up or bonding to gas molecules (extremely effective for hydrogen) that remain within a partial vacuum. It is built with non-evaporable getter material (usually Zr, V, and Fe), the hydrogen dissociates and diffuses into the NEG material (as for residual water, the getter will dissociate it into hydrogen and oxygen at the surface, the hydrogen diffuses and the oxygen reacts to form zirconium oxides, and other gases' reaction can be checked on the

manual.) The NEG acts as a getter or a getter pump that is able to reduce the pressure to less than 1×10^{-12} mbar. It can achieve high pumping speed in a very compact configuration, and the pump time can be tremendously reduced. When activated, the getter can be operated at various temperatures according to a load of active gases. High-temperature operation is preferred when high gas loads are present but not compatible with UHV condition (above 10^{-7} Torr) due to the desorption of hydrogen from the getter material (as we mentioned above). Room temperature operation is mandatory when the gas load is low (below 10^{-8} Torr), which is our daily experiment work condition.

3.6.4 Ion Gauge

We use a hot filament ionization gauge (Ion gauge) to measure the pressure of our vacuum system. It is the most widely used low-pressure (vacuum) measuring device for the region to 10^{-10} Torr. As shown in Fig. 3.7, the functional parts of an ion gauge are the cathode filament, anode grid, and ion collector. The filament is heated to such a temperature that electrons are emitted and accelerated toward the grid by the potential difference between the grid and filament. When an energetic electron collides with a gas molecule, an electron may be dislodged from the molecule, leaving it with a positive charge. Most ions are then accelerated to the collector; this collision rate is proportional to the density of the gas; hence, the ion current is proportional to the gas density, which also means pressure. The Ion gauge we used in our Chamber is a Tungsten Nude Ion gauge (Duniway, T-NUDE-F).

3.6.5 Atomic Oven

The basic idea behind the atom source furnace is to generate neutral atoms vapor near the trap, which electrons can then ionize. Past experiments have used an electron gun to ionize neutral atoms, but it adds extra components to the vacuum system and makes it hard to control the ion number load by the trap. One clever way can ionize neutral atoms gas is by a UV laser. There are two advantages compared to atom-electron collision. First, it is a selective and sensitive ionization

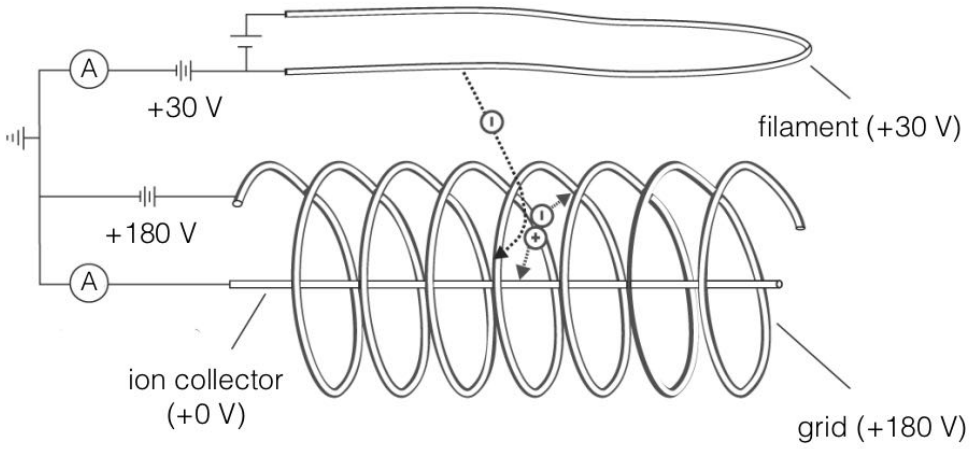

Figure 3.7: Electric circuits diagram of an ion gauge

Table 3.1: Oven test table

Current (amps)	**174 Oven (mins)**	**171 Oven (mins)**
5.0	10.0	12.0
4.5	20.0	24.0
4.0	35.0	40.0
3.5	50.0	53.0
3.0	>60.0	> 60.0

method; second, we don't need to introduce an extra device into a vacuum chamber which would add more inner of the surface and increase the difficulty of vacuuming. Fig. 3.8 (a) shows the energy schematic for ionizing a Yb atom, the 399 nm laser beam promotes the outer electron from the ground S state to the P state. A laser 369 nm (or 355nm) beam will excite the electron from the P state to the continuum spectrum, which means it ionizes the Yb. The design of our oven follows the previous Ph.D. thesis guidance[82], as shown in Fig. 3.8 (b).

We set two atomic ovens with ytterbium 174 and 171. The open end of the tubes is situated in the vacuum chamber to aim through the trap's center. By running a current through the tube and resistively heating it, an atomic "spray" is produced. The size of the tantalum heat sink, the length and thickness of the stainless steel tube, and the electrical current will all have a critical impact on

the thermal characteristics of each of these ovens. Each atomic oven is characterized before being put in the vacuum chamber because too much atomic flux can have detrimental consequences on the Chamber. The oven runs various currents to check its durability and vapor speed; the result is shown in Table 3.1. The feed-through of the oven should withstand 5A current due to the high current applied to the electrical circuit. The location of the oven inside the vacuum chamber is shown in Fig. 3.6 (a)

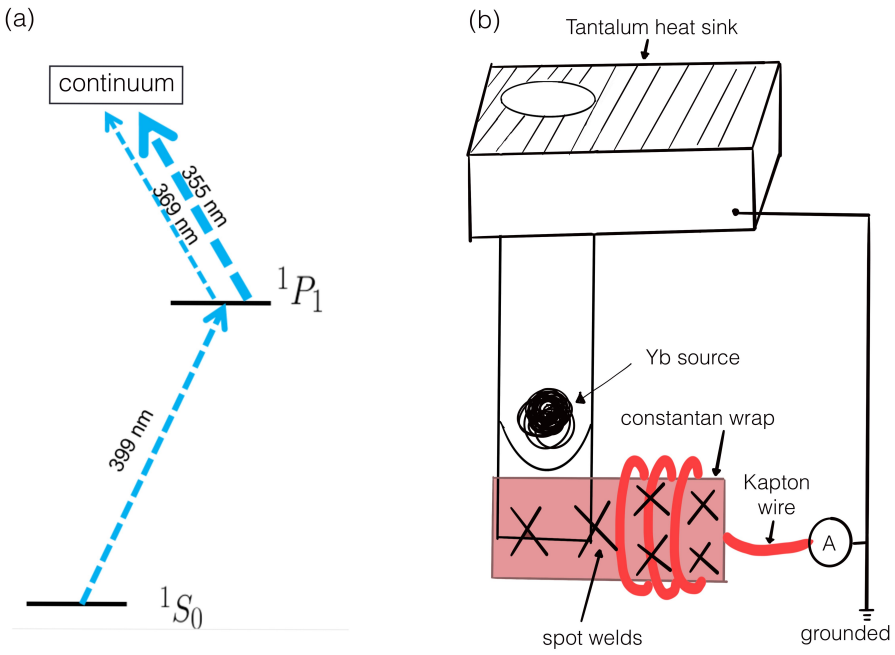

Figure 3.8: Yb ionization and atom oven design

3.6.6 Other Components

The UHV system has strict bounds on the materials used in trap construction, and all components must be UHV compatible (avoid degas) and cleaned well. There are many small items are used within our vacuum system design, and the table below lists all the small items we put inside the vacuum chamber:

Material List			
Items	Part Number	Vendor	Pre-bake
Kapton Wire 22 AWG	100680	Kurt J. Lesker	No
Kapton Wire 24 AWG	112615	Kurt J. Lesker	No
Kapton Tape	KPT2-1	Kurt J. Lesker	No
Epoxy H20E Part B	PB173809	EPO-TEK	No
Epoxy H20E Part A	PB173810	EPO-TEK	No
820pF Capacitor	116UL821M100TT	Mouser Electronics	No
Inline Barrel Connectors	FTAIBC072	McMaster-Carr	Yes
Ring Terminal	FTART1822-6	Kurt J. Lesker	Yes
Glass-Mica Ceramic (Macor)	8489K151	McMaster-Carr	No
316 Stainless Steel Rod	1335T43	McMaster-Carr	Yes
SS 316 2-56 Screws and Nuts		McMaster-Carr	Yes
SS 316 Trap Frame	Company Design		Yes
9 Pins Cable	FTACVR939M	Kurt J. Lesker	No

3.7 Vacuum Preparation

Fig. 3.9 shows the schematic overview of the entire vacuum system. After all vacuum components (including the ion trap) are well prepared, we assemble the parts in the cleaning room to avoid dust and contamination. In general, it is difficult to say that the system can't be pumped to the UHV level; as long as the vacuum chamber is continuously baked and vacuumed, the fingerprints or oil contamination will completely degas after a long enough time, and the vacuum system can still reach 10^{-11} Torr. When we Bake the vacuum system at the desired temperature, it removes water and hydrogen trapped in the stainless steel[83, 84], and the pumping time can be significantly reduced to achieve the UHV region.

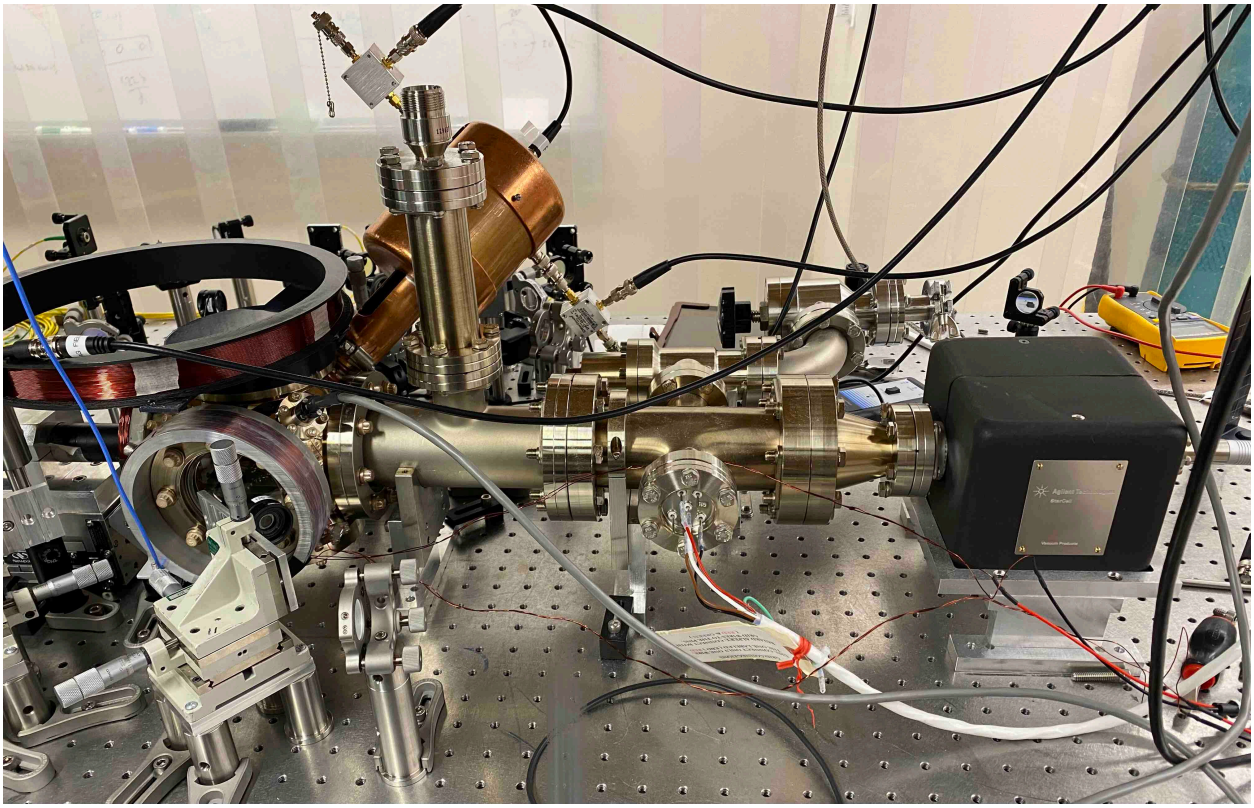

Figure 3.9: (a) Image of the Vacuum System

3.7.1 Baking Process

1. Initial pump down with Turbo/Scroll

When we initial the pump system, the vacuum chamber should be at room pressure, keep the ion pump off, NEG off, and ion gauge off. We attach the end of the turbo pump to the vacuum system using the quick flange(ISO-KF flange) and turn on the TPS bench to pump the system down. Once the pumps are going, wait a couple of minutes, then monitor the pressure with a Magnetic Shield Active gauge near the pump. When the pressure is lower than 10^{-5} Torr, we can measure the pressure inside the chamber by turning on the ion gauge and activating the filament, then the controller will do some automatic zeroing and convert the filament current to pressure. As we can see in the Fig.3.10, the pressure reads $2.0 * 10^{-5}$ Torr. One day of pumping will lower the pressure to 10^{-5} Torr and keep the TPS bench pumping down until the pressure is in the 10^{-6} range (usually needs 2 or 3 days). Typically. If the pressure remains near 10^{-4} Torr after 2 days, there is most

likely a leak. After 48 hours of pumping, the pressure will be in the high 10^{-6} or low 10^{-5} Torr.

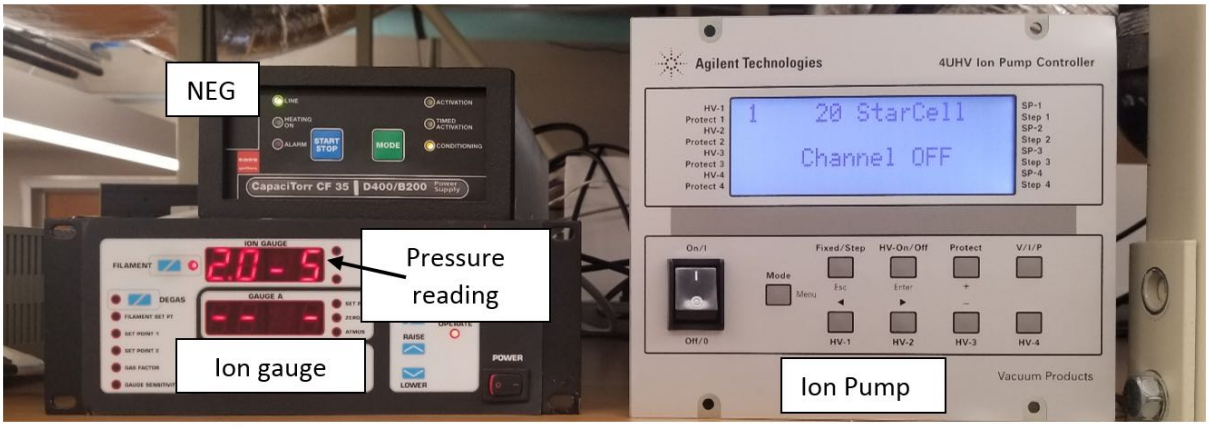

Figure 3.10: Image of ion gauge, NEG, and ion pump controllers.

2. Bake: Climb to 200 °C

Once the vacuum chamber is near low 10^{-5} or 10^{-6} Torr, the vacuum system is ready to bake. We first warp aluminum foil over the entire system except for the electrical connection part of the ion gauge to prevent shorting the pins sticking out. The aluminum foil can spread the heat, and the whole system is baked evenly. Over the aluminum layer, we wrap the vacuum system(including the ion pump) with heat strips (for safety reasons, don't let the heating strips stack up) and cover the system with a second layer of aluminum foil to slow heat dissipation. We connected the heat strip with the heat tape controller, which has a temperature probe to monitor the system's temperature. We place the probe near our interesting region and touch the metal of the vacuum system. There should be at least one probe directly touching the metal of the vacuum chamber head (where the trap is).

The heating process is controlled by the feedback loop as shown in Fig.3.11.Usually, there are several heating loops on a specific temperature set point to ensure the system is heated evenly. Heat loops are either on or off depending on whether the system temperature is at or below the set point of the heat tape controller. Since the heat tape controllers are either full blast or off, we'd prefer a smoother heating feedback cycle. The variacs (General Radio W5MT3 and W10MT3) are used to let us set how much of the full blast is sent into the heat tape. We start variacs at 20 V and increase

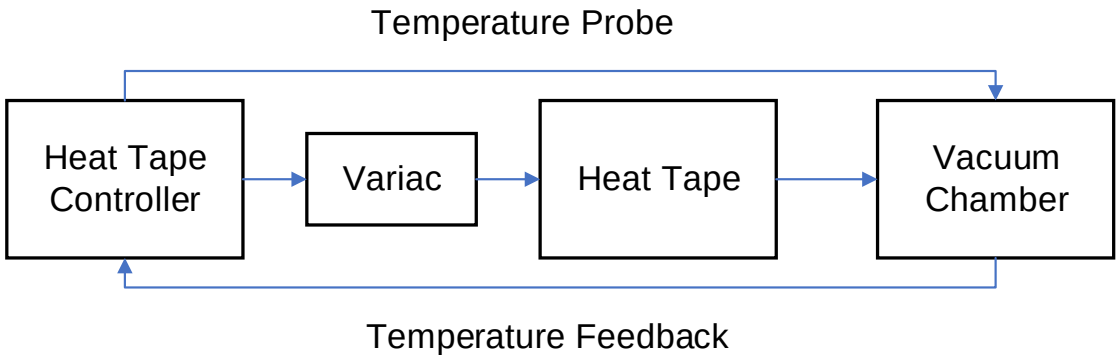

Figure 3.11: The feedback loop of heating process

the temperature set point of the heating tape controller. If the heat tape struggles to maintain the set temperature, increase the variacs voltage output (usually add 10 V each time) on the heat strip. Increase the temperature at a rate of 5 °C / 10 min until you get to 100 °C. We condition the NEG at 100 °C for 5 minutes or until pressure reaches 10^{-4} Torr. After conditioning the NEG at 100 °C, keep the same heating rate until the system is just below 200 °.

3. Bake: At 200 °C

Leave the system baking just under 200 °C until pressure reads 10^{-8} Torr, which will take several days. While waiting for the pressure to lower, condition the NEG again. If the pressure is above $5 * 10^{-4}$ Torr, stop the NEG conditioning, wait for the pressure to drop, then start the conditioning again. Repeat this process until we can turn on the NEG conditioning (pressure should be below $5 * 10^{-4}$ Torr all the time)for an hour straight. We activate the NEG by turning on the activation mode near the end of the bake and turning off the activation mode if the pressure exceeds $5 * 10^{-4}$ Torr. We continue turning on and off the activation mode until the pressure without going over $5 * 10^{-4}$ Torr for a straight hour under the activation mode. Once the activation mode doesn't exceed $5 * 10^{-4}$ Torr, turn on the timed activation mode which will automatically turn off in 1 hour. When the pressure has settled back down to $1.0 * 10^{-6}$ Torr, restart the ion gauge by turning off the filament, waiting 10 seconds, and turning it back on. This can help the ion gauge realize the pressure is actually in the 10^{-7} Torr range. Once the pressure measures the low 10^{-7} Torr range, the ion pump can be used instead of the turbo/scroll pumps. Turn on the ion pump by turning on the

power switch, then close the metal valve until it's snug to prevent a break. Turn off the turbo/scroll pump if everything looks good and has settled back down.

4. Bake: Fall to 30 °C

Lower the temperature by lowering the temperature 5 °C / 10 min until at room temperature and remove the heat strips and aluminum foil, the final pressure is under 10^{-11} Torr. The pressure as a function of time is shown in Fig.3.12.

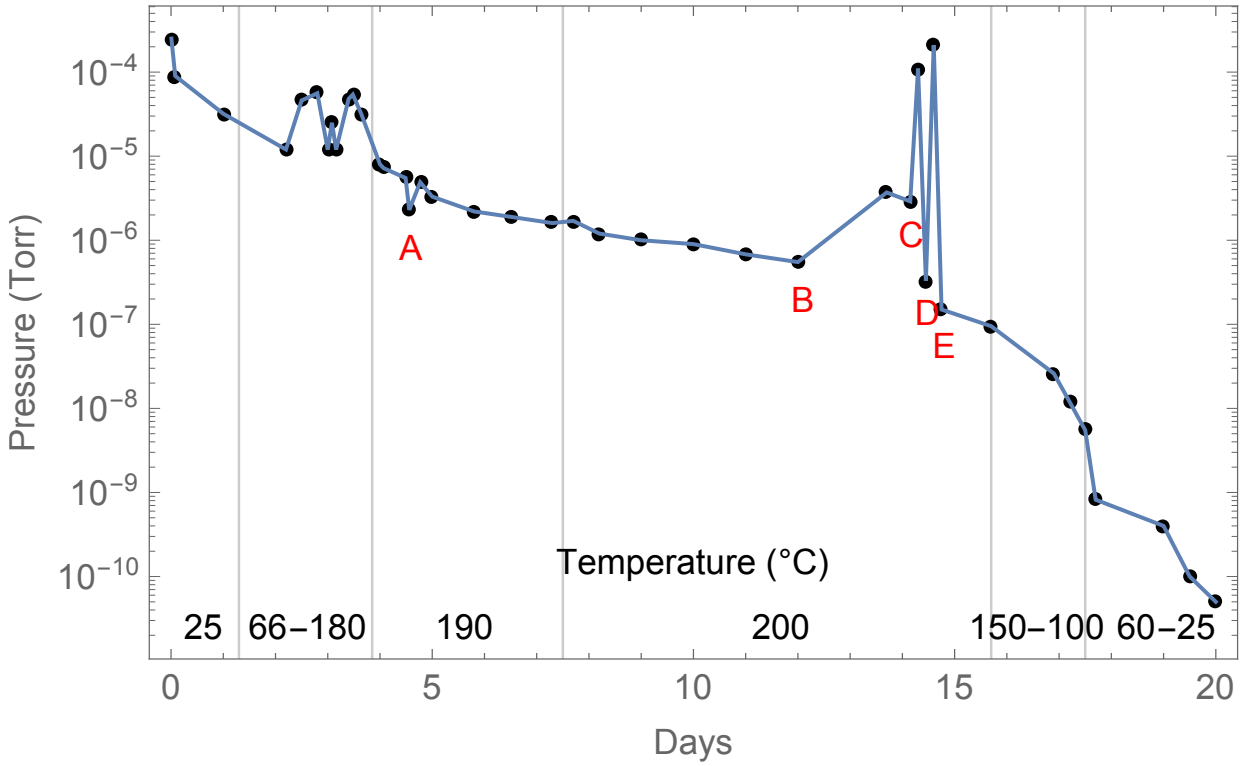

Figure 3.12: Ion trap bake, showing pressure (Torr) and temperature (°C) versus time (days). Operations we applied on each point on the graph; point A: turn on the ion pump for 10 mins; point B: turn on the NEG "conditioning" for 1 hour; points C and D: activate NEG to the max pressure (10^{-4} Torr), then stop; point E: Turn on the ion pump and after half of the day, then turn off the metal valve.

3.8 Electrical Circuit

To perform quantum simulation, we need a reliable control system. Generating a stable high rf signal with less noise and obtaining stable static voltage is crucial during the experiment. In

this section. I will introduce how to generate and amplify a less noisy rf signal, briefly discuss the electrical circuits of our rf and dc voltages, and summarize our control system.

3.8.1 Helical Resonator

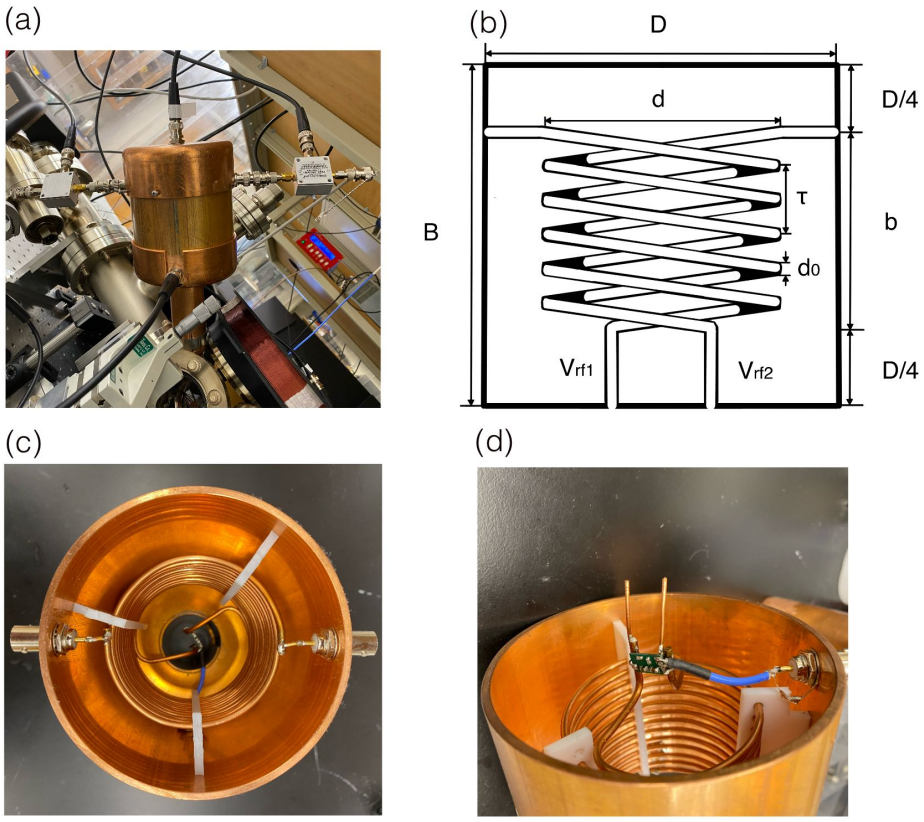

Figure 3.13: Graphs of the two coils helical resonator

Ions confined by a Paul trap require a stable, high voltage, and low noise rf potential. The rf signal can be generated by a signal generator (HP 8648A), but we cannot directly apply it to our experiment; the raw signal produced by the generator has these disadvantages: low power, too much noise, and no concentration. Thus we need a helical resonator to amplify voltage while filtering noise injected into the system [85] and make an impedance match between the rf source and the ion trap. To construct a single coil helical resonator with the expected resonate frequency, the design parameter can be calculated in this way[85]:

The height of the main coil b in units of meters can be obtained

$$\begin{aligned} b \approx & \frac{C_{\sum} + K_{cd}}{K_{C_s} + K_{cb}} \\ & \times \left(\frac{K_{C_s} + K_{cb}}{(C_{\sum} + K_{cd})^2 K_{L_c} \Omega_T^2} - \frac{1}{2}\right) \end{aligned} \tag{3.4}$$

Where the capacitance of the wires and ion trap $C_{\sum} = C_{wire} + C_{trap}$ and the capacitance measured in units of farads between the coil wire (the diameter of the coil d) and the outer shield (the shield diameter D) is provided by:

$$\begin{aligned} C_s &\approx b K_{C_s}(d, D) \\ K_{C_s}(d, D) &= 39.37 \frac{0.75}{\log(D/d)} \times 10^{-12} \ \ F/m \end{aligned} \tag{3.5}$$

The inductance of the main coil when couple with outer shield ($d/b \ll 1$):

$$\begin{aligned} L_c &\approx b K_{Lc}(d, D, \tau) \\ K_{Lc}(d, D, \tau) &= 39.37 \frac{0.25 d^2 (1 - (d/D)^2)}{\tau^2} \times 10^{-6} \ \ H/m \end{aligned} \tag{3.6}$$

where τ is the winding pitch of the coil. The linear approximation to the coil self-capacitance is $C_c \approx K_{cb} b + K_{cd}$ where $K_{cb} = 11.26 \times 10^{-12} \ \ F/m$ and $K_{cd} = 35d \times 10^{-12} \ \ F$. Based on this calculation, the voltage on the trap is related to the quality factor Q and the input power P: $V = 10\sqrt{PQ}$.

Our 2D trap design requires us to build a two-coil resonator that allows for independent dc biasing of the rf blades so that the trap may be compensated along the rf blades' orientation, as we can see in Fig. 3.13 (a) and (c), we connect two bias tees (Mini-Circuit ZFBT-42GW+) to achieve the compensation with the main coil. A cross-sectional drawing of the two-coil resonator is shown in Fig. 3.13(b). The main coil connects with two BNC adaptors as output ports for compensation bias and is stabled by the Teflon holder, which only absorbs a tiny portion rf signal. Under the same desired resonate frequency, the winding pitch of every single coil of the two-coil helical resonator

need to meet $\tau_{two} = 2 \times \tau_{one}$, and τ_{one} is the pitch of the standard helical resonator(single coil helical resonator).

We measure the capacitance of the connection wire and ion trap C_{trap} at the trap feedthrough, select a copper shield and coil wire with the proper size and then assemble all components. And the chosen design parameters are listed in the table below. Under these conditions, the resonant frequency is $\Omega_t = 2\pi \times 27.51$ MHz and a Q-factor of about 110 when connected to our blade trap. The input power to the helical resonator is approximately 30 dBm or 1 W; this would generate a radio-frequency voltage of about 200- 300 Volts. All parameters for the helical resonator design are listed in the table below.

Trap Parameters	
Parameters	Value
Trap Capacitance C_{trap}	7 pF
Wire Capacitance C_{wire}	3 pF
Shield Diameter D	97.8 mm
Shield Length D/2+b	97.8 mm
Winding Pitch τ	10 mm
Wire Diameter d_0	2.58 mm
Coil Length	40 mm
Resonate Frequency Ω_T	$2\pi \times 27.51$ MHz

The two coils helical resonator allows us to bias the trap in rf direction, which would provide more flexibility for our ion control. However, it has some disadvantages. First, under the same resonant frequency, the quality factor Q is lower than that of a single coil helical resonator. This weakness can be overcome by injecting more rf power. The second drawback is the two coils will separately couple with the antenna coil causes the rf outputs with phase differences due to the mechanical asymmetry. To combat this, we designed the circuit shown in Fig. 3.14 (a) and Fig. 3.13 (d) to balance the phase difference. The balance circuit includes two capacitors C_1 and C_2

(KEMET, SMD Comm X5R series, 10 μF) to bridge between the resonator's two outputs V_{rf1} and V_{rf2} which cause the phase different is less than 1%.

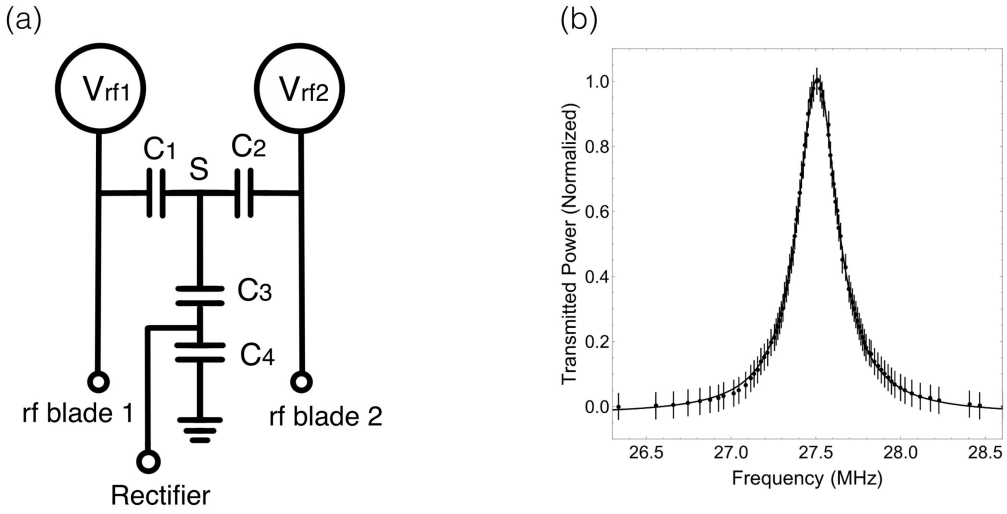

Figure 3.14: Sampler circuit and the quality factor diagram

And the circuit in Fig. 3.14 (a) can appropriately sample the transmitted rf voltage, too. We put a capacitive divider connected to point S, which is used to scale down the high rf-voltage for sampling, the advantage of this way is the potential at the probing point S is the average value of the outputs. The divider consists of two high voltage-tolerance capacitors, C_3 (AVX Corporation, SQ series, 0.2 μF) and C_4 (AVX Corporation, UQ series, 20 μF). The combination picks off 1% of the high voltage signal (down to the $\sim 1-5$ V range). Then we measured the power of the rf pickup signal from the sampling port as a function of input rf frequency. with this circuit, the Q factor of the resonator can be calculated ~ 100 (as shown in Fig. 3.14 (b)), only decrease by 10%.

3.8.2 rf Locking and Stability

There is a rectifier between capacitor C_3 and C_4, and the pickoff signal after the rectifier will go to the feedback loop to help stabilize rf power. Our feedback loop is controlled by a Proportional-Integral-Derivative controller(PID controller) as shown in Fig.3.15. The PID is a control loop mechanism employing feedback that is widely used in industrial control systems and a variety of other applications requiring continuously modulated control. The feature of the PID controller is

the ability to use three terms proportional, integral, and derivative influence on the controller output to apply accurate and optimal control. The proportional term **P** is proportional to the current error with the gain factor "K_p". The Integral term **I** accounts for past error values and integral them over time to produce the term **I**. When the error is eliminated, the integral term will cease to grow. The derivative term D estimates the future trend of the error based on its current rate of change.

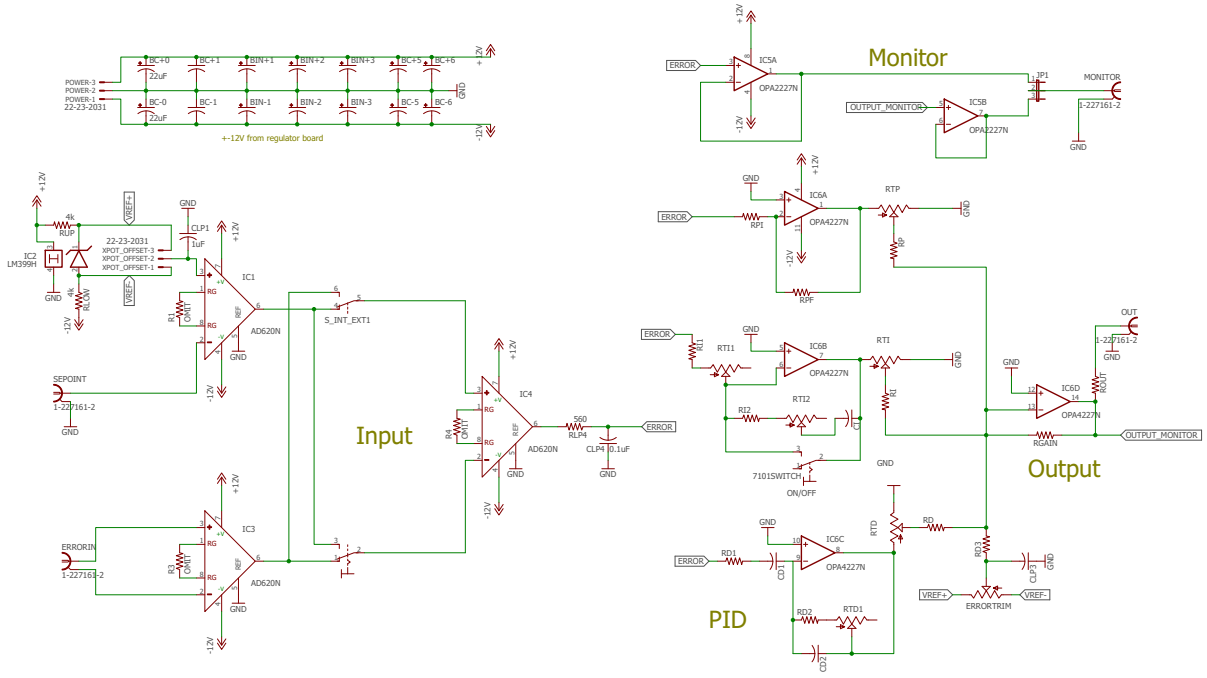

Figure 3.15: Electrical diagram of the PID loop.

The fidelity of quantum operations is sensitive to the amplitude of the rf signal. Noise on the rf power may be introduced in any steps of the rf circuit, e.g., the rf amplifier, mechanical vibrations of the helical resonator, and the temperature drifts. From Eq. 2.23, we know the trap secular frequencies depend on the V_0/Ω_T, and the driven frequency produced by the rf signal generator is typically well-stabilized, so it is vital to keep the rf amplitude stabilized to increase the fidelity of

our quantum experiments. The stabilization circuit is shown in Fig. 3.16 [86].

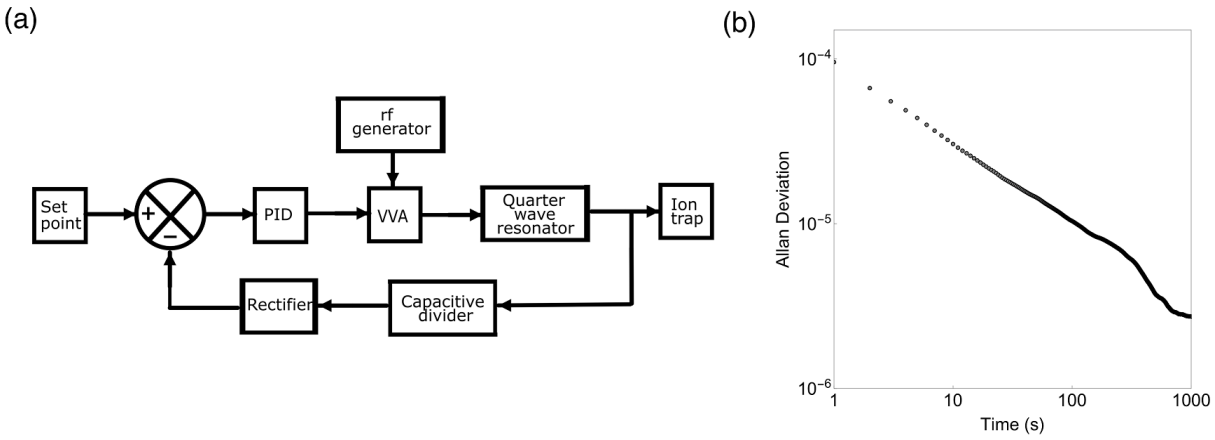

Figure 3.16: (a) Servo loop block diagram for active stabilization of the rf voltage amplitude. VVA: voltage variable attenuator, PID: proportional–integral–derivative controller. (b) Allan deviation of the rf signal amplitude during operation of the servo loop in (a)

The detail of our servo loop block diagram is shown in Fig. 3.16(a). We stabilized the rf confinement potential by sampling the high voltages from the helical resonator output ports, and we fed back it by a voltage variable attenuator (VVA) (Mini-Circuits ZX73-2500-S+). The schematic of the servo loop is present as follows: an rf signal at frequency $\Omega_t = 2\pi \times 27.51$ MHz and power -8 dBm is produced by our rf generator. It first passes through the VVA and then is sent to the rf amplifier (Mini-Circuits ZHL-5W-1+), which grants a gain of 40 dB. The amplifier signal is fed to the helical resonator, which provides impedance matching between the rf source and the trap. A capacitive divider samples roughly 1% of the helical resonator output by the ceramic capacitors C_3 and C_4, the picked-off signal from the capacitive divider passes through a rectifier circuit which would rectify the rf signal, and it is fed as the input of a closed proportional–integral–derivative (PID). The rf amplitude is thus stabilized concerning the set point value. We perform long-term monitoring of the dc signal after the rectifier engages the servo. These measurements represent the scale of rf amplitude fluctuations over time. The Allan deviation of rf amplitude scales with time τ as $\approx 1/\sqrt{\tau}$; at 1000 s, the relative stability is $2.74 \pm 0.04 \times 10^{-6}$, which translates to a ~ 30 Hz RMS fluctuation of the radial secular frequencies.

3.8.3 Dc Circuits

As we see in Fig.4.8, The trapping potential is controlled by the static voltage DC1 through DC6, RF1, RF2, and compensation 1, 2. The static voltages are provided by the Zotino modular of Artiq, which we will introduce later. Linear combinations of the static voltages are used to control the ions' position. The endcap average voltage $V_{end} = (V_1 + V_3 + V_4 + V_6)/4$ and the central average voltage $V_{central} = (V_2 + V_5)/2$ control the overall strength of the trapping potential, where V_i is the static voltage applied on the electrodes labeled DCi. We also define the average bias voltage $V_{bias} = (V_{rf1} + V_{rf2})/2$ to slightly adjust ion position. The combination of these voltages with different ratios controls the principal axes of the trap along the radial direction. The axial push voltage $V_z = [(V_1 + V_4) - (V_3 + V_6)]/2$ can push ions position along axial direction. The voltage difference $V_{diff} = [(V_1 + V_3) - (V_4 + V_6)]/2$ and $V_3 - V_5$ are used to minimize the micromotion of ions[61]. And voltages on two compensation rods can push the ions up and down vertically.

A stable, low noise voltage applied to the dc trap electrodes is also crucial to the experiments. We apply these voltages using static dc power supplies (Matsusada R4G series) that can output 0-120 V with one mV RMS ripple. Given the small dimensions of our blade trap means that we do not need applied high voltages on the electrodes. However, all electrodes (especially dc electrodes) are too close to pick up unwanted rf signals from the rf electrodes. To mitigate this pickup effect, each dc blade segment is connected to an 800 pF capacitor (Muser 100 Volts 800 pF 20%) to shunt rf pickup to the ground (see Fig. 3.6(c)), we planned to do wire bond between the blades and the 800 pF capacitors. However, any light touch would break the connection due to the weak connection strength; soldering is generally not allowed in the UHV system so we adapt the UHV-compatible epoxy (details are listed in the previous section) to glue the wire and capacitors.

To model the practical in-vacuum circuit, we treat the ion trap as a capacitor (C_{trap}) and consider the contributions from two aspects: the on-trap filter elements (C_{filter} and R_{filter}); and vacuum feed-throughs (R_{feed}, C_{feed} and L_{feed}), as shown in Fig. 3.17. By using this model, The estimation of the rf pickup on the static dc blades shows in this way, the impedance of the whole system is

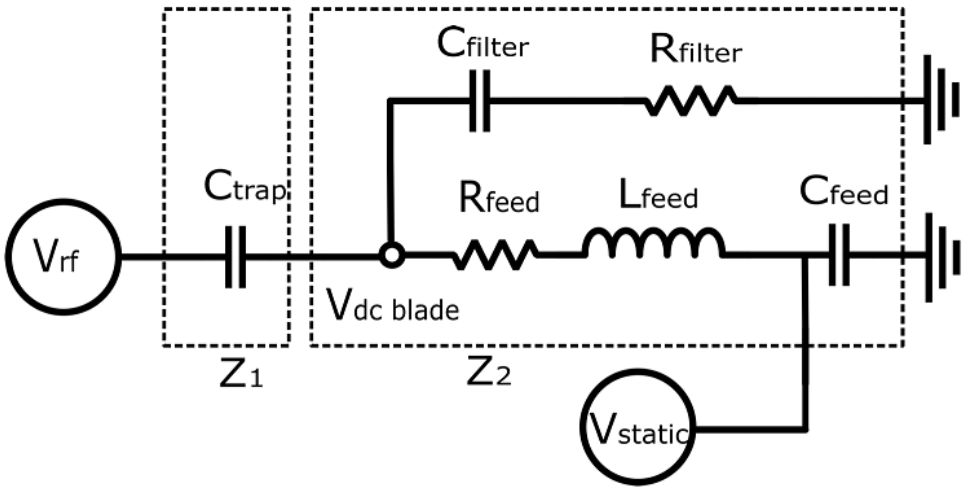

Figure 3.17: Dc circuit diagram of our ion trap. The in-vacuum filter is designed to reduce the rf pickup on the static dc blades. See text for details and component values.

$$Z_2 = \left(\frac{1}{Z_{C,filter} + Z_{R,filter}} + \frac{1}{Z_{C,feed} + Z_{R,feed} + Z_{L,feed}} \right)^{-1} \tag{3.7}$$

where , $Z_{C_{feed}} \approx R_{feed} \ll 1\ \Omega$, $|Z_{C_{feed}}| = 1/(\Omega_t C_{feed}) \approx 1.8\ \Omega$ and $|Z_{L_{feed}}| = \Omega_t L_{feed} \approx 52\ \Omega$. We measured the resistance of the filter $R_{filter} \ll 1\ \Omega$, which is negligible compared with the capacitive filter impedance $|Z_{C,filter}| = 1/(\Omega_t C_{filter}) = 7.2\ \Omega$ ($C_{filter} = 800$ pF). Thus, the impedance estimation of the whole system is $|Z_2| = 6.4\ \Omega$. The measured trap capacitance of 10 pF (including the capacitance of the wire connection) leads to an impedance $|Z_1| = 600\ \Omega$ at our trap drive frequency. Therefore, the estimated rf pickup on the dc blades is then $|Z_2|V_{RF}/(|Z_1| + |Z_2|) = 0.01V_{RF}$. We note that in the absence of the on-trap filter capacitors, the rf pickup on the dc blades would be approximately a factor of 8 larger.

3.9 Control System

Modern research presents many challenges in controlling and measuring the quantum system. A complete quantum system needs the following requirements: first, it can receive and generate a large number of high-precision timing signals. Second, it can measure quantum states with high

precision and low reaction latency. Third, it can implement quantum gates in the algorithm. And the field-programmable gate arrays(FPGA) architecture allows us to fulfill the requirements; there are dozens of FPGAS schematic designs for quantum simulation. Still, most of them are home built, which usually requires vast space and is hard to organize after running for many years. We chose our FPGA-based solution from Artiq to exploit our 2D quantum simulation.

Artiq is an open source project for controlling quantum physics experiments(`https://m-labs.hk/experiment-control/artiq/`). It contains packages of hardware and software. The hardware facilities are shown in Fig.3.18, which are composed of the main control module and a large number of auxiliary control modules. The main control module is called Kasli. Kasli can be used as a standalone core device or as a DRTIO satellite or repeater. The signal of the Kasli can be transformed by an SFP connector for Gigabit Ethernet to connect to your computer network. The auxiliary modules can be purchased selectively from M-lab. This "family" of electronics that kasli controls are called the Sinara hardware; they are usually insert-type integrated circuit slats, which can be easily installed on the main control box. So we can customize our Artiq box by ordering the modules we need and then installing or replacing the slats in the main control system.

Main module introduction:

Artiq Modules		
Modules	Controls	Features
Kasli EEM Controller	Control other modules	Core device; kernels on a 1GHz CPU with a hardware FPU
Crabber Camera Input	Andor iXon Ultra/Life EMCCD 888/897, Andor X3.	Base transfers 28 bits (4 control and 24 data) per clock cycle; Maximum clock frequency: 85 MHz

SMA-DIO TTL IO	PMT; RF Period; Microwave Horn; 355 nm Laser Switch; Camera External Trigger	Min pulse width 5ns; Max 150MHz toggle rate with 50% duty cycle; Panel width: 4HP
Urukul 4x1GS/s DDS	Doppler Cooling Beam AOM; Optical Pumping Beam AOM; Detection Beam AOM; Protection Beam AOM; 355nm Beam AOM	Output frequency (-3 dB): <1 to >400 MHz;Digital step attenuator resolution: 0.5 dB (0 to -31.5 dB); see other details on Artiq website.
Smapler 8x1MS/s ADC		Width: 8HP; Resolution: 16-bit; Sample rate: up to 1.5 MHz
Zotino 32x16 Bits DAC	Compensation Voltage Control; DC Voltage Remote Control; Beam Shutter; Mirror Flipper	Width: 4PH; Resolution: 16-bit; Update rate: 1MSPS; Output voltage: ±10V
Artiq Modules		
Modules	Controls	Features
IDC-BNC ADAPTER		IDC to BNC adapter for Zotino DAC
Phaser Upconverter	355 AOm	4 channel 625 MS/s from FPGA; 4 channels of 1.25 GS/s 16-bit parallel DAC.

Artiq is also the name of the software package where you can write python code to control the Sinara family electronics (auxiliary control modules). During the process of describing an

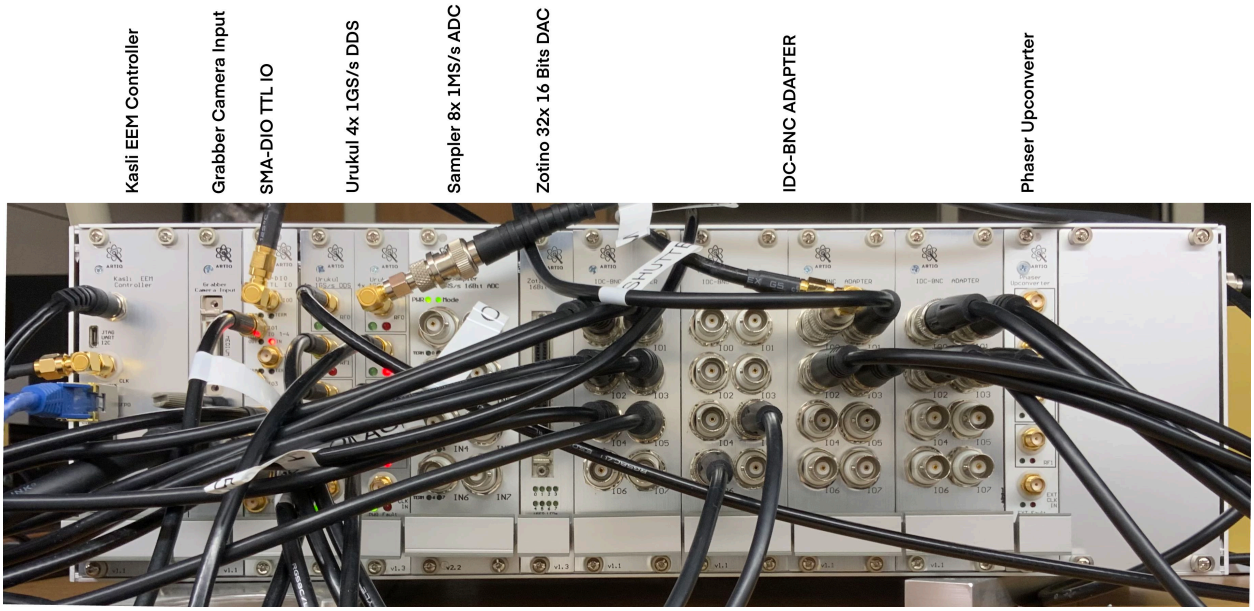

Figure 3.18: Diagram of the Artiq box

experiment, Python compiles and executes the auxiliary modules with nanosecond timing resolution and sub-microsecond latency. Python files can be imported into the Artiq dashboard, and we can run a completed file as a single application. With parameters typed in the application, trigger signals and pulses can be sent to our ion trap experiment hardware. The Artiq doc can be found in `https://m-labs.hk/artiq/manual/index.html`. However, the docs are very limited in explaining/showing what Artiq is capable of doing and what functions relate to what actions the electronics take. There are some example codes on the GitHub `https://github.com/m-labs/artiq`.

3.10 Image system

The imaging system provides 40 times magnification with a numerical aperture of 0.24. As Fig.3.19, light form an ion in our system gives a diffraction-limited spot size $0.61\lambda/N.A. = 0.8\mu$m. The light after the front viewport will pass through an objective which contains three lenses and a best-form lens; then, a pinhole is designed to cut the background noise light, the further magnified and projected onto an EMCCD camera(Andor iXon 897). After the doublet, light passes

two spectral light filters and enters a dark box to prevent background light. There is a flipping mirror controlled by a TTL pulse that can swap the light pathway; the light is sent to either a photo-multiplier (PMT) or the EMMCCD camera.

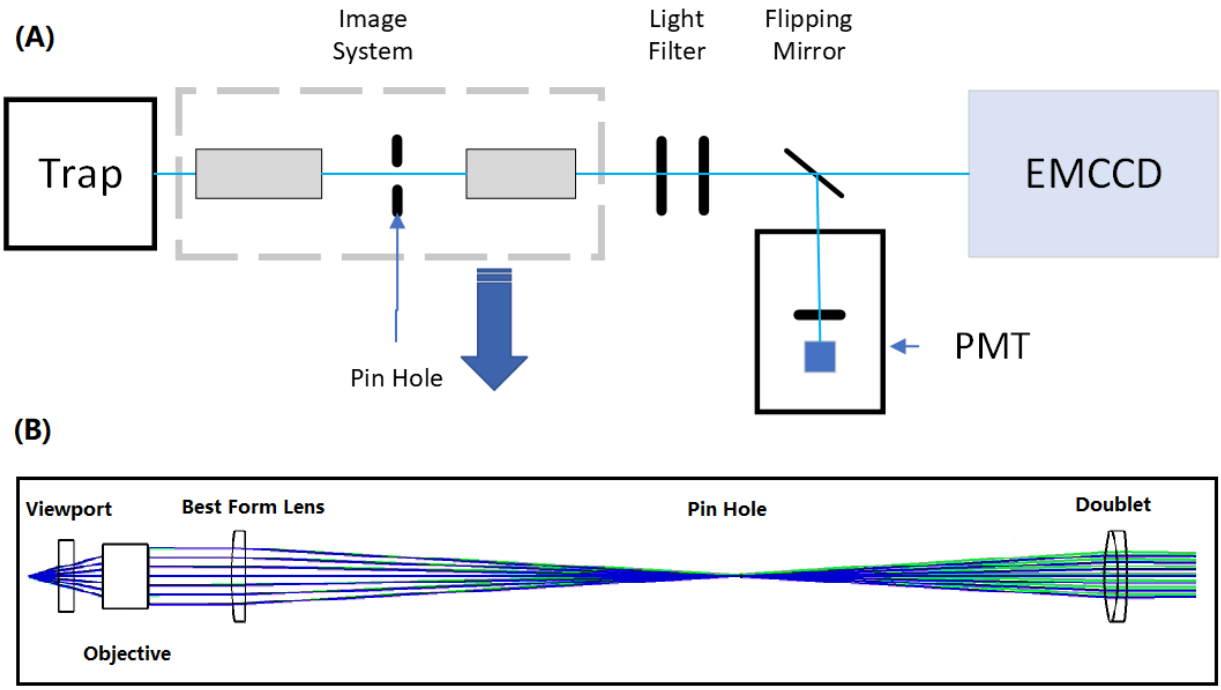

Figure 3.19: Image System: (A) The pathway of the ion fluorescence from the ion to the EMCCD camera or PMT. (B) Light is magnified(X5) by the objective, focused by the best form, then goes through a 100 mm pinhole and is further magnified(x8) by the doublet.

CHAPTER 4

Experimental Preparation of Yb Ion Crystals

4.1 Hyperfine qubit

For quantum simulation experiments, Ytterbium (Yb) 171 ion is especially attractive because the nuclear spin is 1/2, allows for fast and efficient preparation and detection of the hyperfine ground states, and the Yb is heavy enough to offset the impact from background gas to an extent. Fig. 4.1 shows the energy level of a Yb 171 ion. In the quantum simulation experiments, we define the two hyperfine states $^2S_{1/2}|F = 1, m_F = 0\rangle$ and $^2S_{1/2}|F = 0, m_F = 0\rangle$ as qubit $|\uparrow\rangle$ and $|\downarrow\rangle$. These two states are first-order insensitive to external magnetic field noise and can yield coherence times of over 10 min [87]. In our experiment, we applied external magnetic field $B_Y \approx 5$ G, the hyperfine frequency splitting between them is $\omega_{hf}/2\pi$ = 12642812118.5 Hz + $B_Y^2 * 310.8$ (Hz/G^2) [88]. The natural abundance of Ytterbium isotope-171 is around 14.09%; we bought the Yb 171 with enrichment 87-95 % from the Oak Ridge National Laboratory.

Ytterbium (Yb) 174 ion can be used to troubleshoot optics alignment problems. With HeNe laser 632.992 nm as a reference, we applied one 369.5 nm (811.29114 THz) beam, the 935 nm (320.572021 THz) beam, and the 399 nm (751.527300 THz) beam to load Yb 174 ion. It requires that all beams are approximately passing through the trapping region. Once we trap Yb 174 ion, we can switch to load Yb 171 ion by setting the frequencies of the 369nm beam at 811.28874 THz, the 399 nm at 751.528200 THz, and the 935 nm beam at 320.569295 THz to load Yb 171 ion and filter other isotopes.

4.2 Doppler Cooling, Detection and Optical pumping

4.2.1 Doppler Cooling

In Yb 171 ion energy level diagram, $^2S_{1/2}$ to $^2P_{1/2}$ transition with Gaussian beam at wavelength 369.5261 nm is sett as Doppler cooling scheme, it is red detuned from resonance by about 10 $\sim$ 20 MHz. When one of those photons comes close to the ion, due to the red detune, the ion move towards the light source has a high possibility of absorbing that photon, then emitting an identical photon in some random, unpredictable direction; then ion lose a momentum equal to the momentum of the photon absorbed[89], and therefore the kinetic energy of the ion, will be reduced.

For Yb 171 ion, in order to cool both the spins $|\uparrow\rangle$ and $|\downarrow\rangle$, we use an EOM (Electro-optic Modulator) frequency modulate the Doppler cooling beam with 0.95 W, at 14.747811 GHz sideband which couples the $^2S_{1/2}|F = 1, m_F = 0\rangle$ state to $^2P_{1/2}|F = 1, m_F = 0\rangle$ state. An AOM (Acousto-optic modulator, Brimrose CQF-420-100-369) upshift 420 MHz created sidebands for optimal cooling; we set the first order sideband of this AOM as Doppler cooling beam which is 10 MHz red detuned from the resonance frequency. The 0th-order beam produced by this AOM is set as the Protection Plus beam, which is used to help trap ions and maintain ion crystallization. What's more, efficient cooling needs an extra beam to cool ions when ions look fuzzy, and we call it the Protection beam with 100 MHz detuning of its AOM. This Protection beam is far detuned to help with recrystallizing after collision events[90]. Yb 171 ion's hyperfine states require that Doppler beams contain σ^+, σ^-, and π light that can be optimized with an HWP (half-wave plate) before the fiber coupler port.

Another necessary laser with a wavelength of 935 nm helps to cool the ions efficiently; as the energy diagram Fig.4.1 shows, there is a 0.5% branch ratio for ions in P state decay to D state. This beam is sent through a 3.1 GHz fiber EOM (EOSpace Lithium Niobate) driven at 3.07 GHz, which is powered by an HP 8648C rf generator, to repump $^2D_{3/2}$ that leaks from $^2P_{1/2}$ states[83]. The 935 nm beam will pump the $^2D_{3/2}$ to a virtual bracket state $^3\,[3/2]_{1/2}$, then spontaneously decay back to $^2S_{1/2}$ state, which would prevent ions are trapped at D state for a long time.

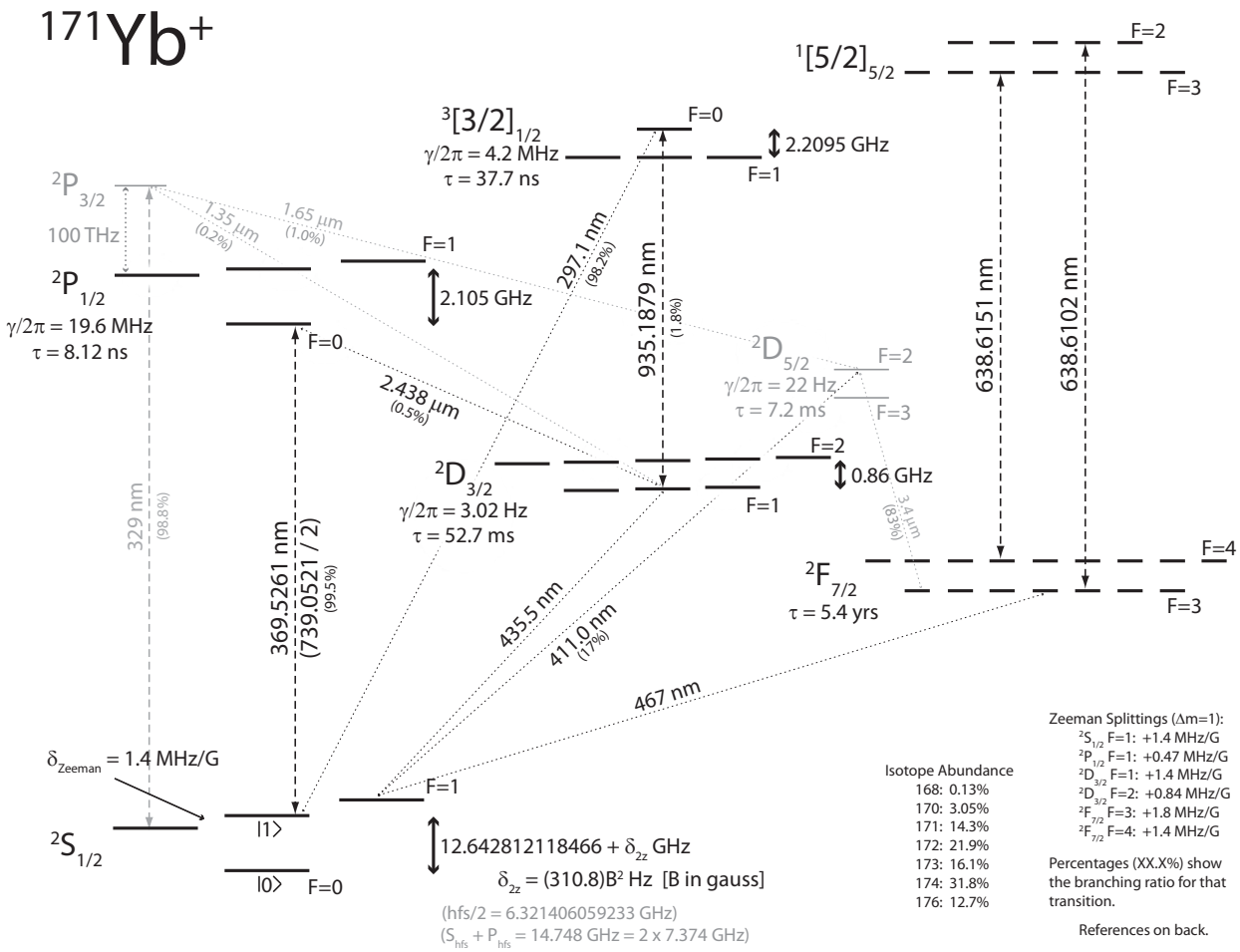

Figure 4.1: Diagram of the electronic energy levels of Yb^+ that are relevant for our experiments. The transition between the $^2S_{1/2}$ and $^2P_{1/2}$ states occurs at 369.5261 nm; the lifetime of the $^2P_{1/2}$ state is 8.12 ns, and it decays to $^2S_{1/2}$ 99.5% of the time, 0.5 % to the D state. The 935 nm will repump the D state to a bracket state $^3\,[3/2]_{1/2}$, then decay back to the S state.

4.2.2 Detection

We define the $^2S_{1/2}|F=1, m_F=0\rangle$ as spin state $|\uparrow\rangle$ and $^2S_{1/2}|F=0, m_F=0\rangle$ as spin state $|\downarrow\rangle$. The detection beam is on resonant excited the $^2S_{1/2}|F=1, m_F=0\rangle$ and $^2P_{1/2}|F=0, m_F=0\rangle$, it has all the polarization components(π, σ^+, σ^-) and hence ions in the $|\uparrow\rangle$ and the Zeeman states can be excited to the $^2P_{1/2}|F=0, m_F=0\rangle$ state, once the ions excited to the $^2P_{1/2}|F=0, m_F=0\rangle$ state, ions spontaneously decay to one of the three $^2S_{1/2}|F=1, m_F=0, \pm1\rangle$. Then the spin state $|\uparrow\rangle$ (and the Zeeman states) appears as a 'bright' state. Since $^2P_{1/2}|F=0, m_F=0\rangle$ to $^2S_{1/2}|F=0, m_F=0\rangle$ transition is forbidden, the transition loop won't jump into state $|\downarrow\rangle$[57]. Meanwhile, the detection

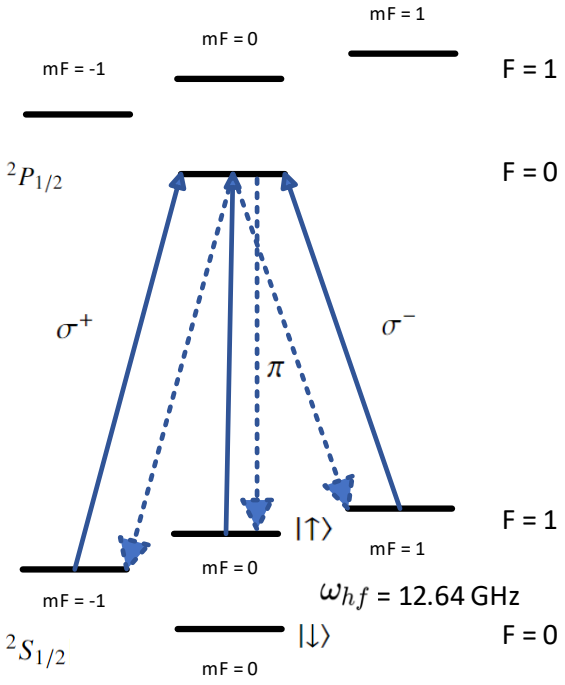

Figure 4.2: Detection: a near-resonant laser beam at 369 nm couple the $|\uparrow\rangle$ state to $^2P_{1/2}|F = 0, m_F = 0\rangle$, then decay back to the $|\uparrow\rangle$ or two Zeeman state, but not the $|\downarrow\rangle$ state, the detection contains all polarization components thus all states in $^2S_{1/2}|F = 1\rangle$ can be excited back to $^2P_{1/2}|F = 0, m_F = 0\rangle$ state

beam appears off-resonate to the spin state $|\downarrow\rangle$ by about 12.64 GHz, which means $|\downarrow\rangle$ will not be excited; it appears as a 'dark' state on the camera system. We collect the fluorescence with with our image system (NA = 0.24, magnification = 40) on a photo-multiplier tube (PMT) or a EMCCD camera. The detection beam is on for 800 us, and we collect about ten photons on average with the PMT, and Fig. 4.3 shows the histogram of dark and bright ions from a single ion detection.

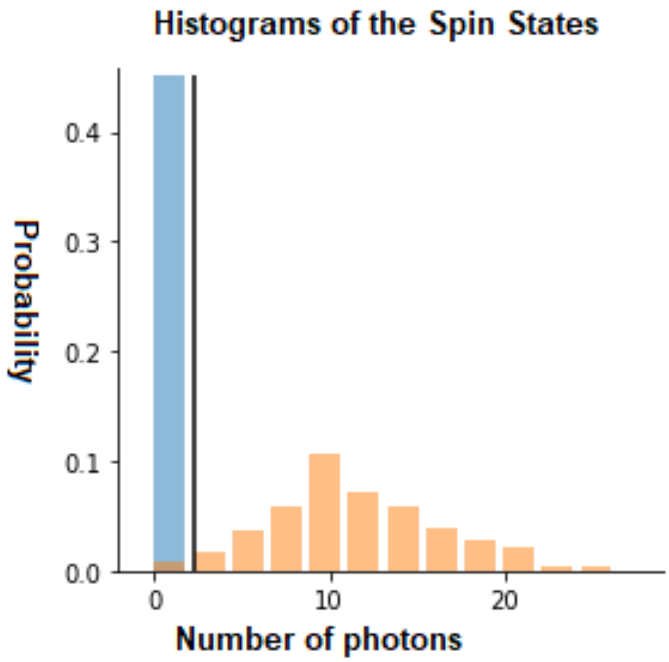

Figure 4.3: Fluorescence histograms of the spin states: we collect the fluorescence of the ion on a photo-multiplier tube (PMT) for 800 us. A histogram of the photon counts is shown for the bright state $|\uparrow\rangle$ in yellow. The spin state $|\downarrow\rangle$ appears dark (blue histogram)

4.3 Optical Pumping

The state of the qubit is initialized in the $|\downarrow\rangle$ by optical pumping technique. An amplified HP8664A rf generator powers the 2.105 GHz EOM, which generates the first sideband couples with ${}^2S_{1/2}|F = 1, m_F = 0\rangle \leftrightarrow {}^2P_{1/2}|F = 1, m_F = 0, \pm 1\rangle$ transition, then ions decay into the spin $|\downarrow\rangle$ states (Fig. 4.4). The spin $|\downarrow\rangle$ is off resonated 12.64 GHz from the ${}^2P_{1/2}$, and won't be excited; thus, ions are trapped in the $|\downarrow\rangle$ state. The trapping events increase with the number of scattering events rise. When this optical pumping is repeated, almost all population transfers to the spin $|\downarrow\rangle$ and initializes our state. Our trap optical pumping characteristic time is around 0.4, and the efficiency is about 99% for 2 μs optical time.

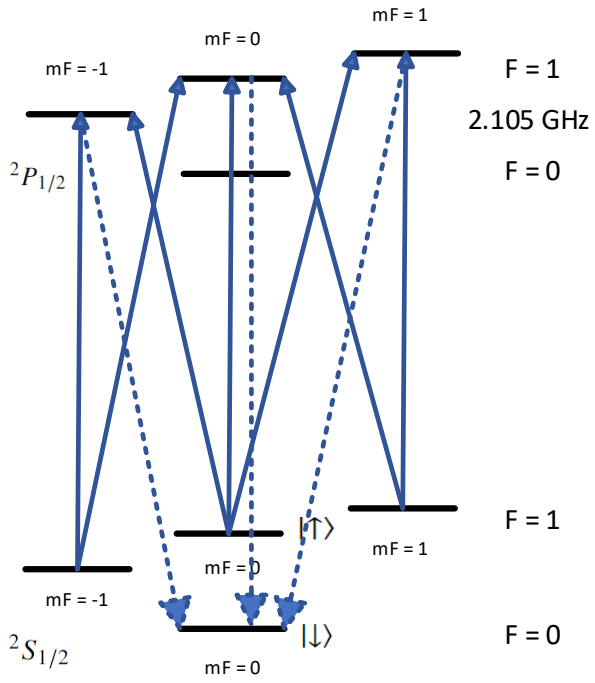

Figure 4.4: Diagram of the optical pumping strategy to initialize the $|\downarrow\rangle$ state.

4.4 Laser Arrangement

An optical pathway diagram for lasers is shown in Fig. 4.5. The Moglabs continuous wave (CW) produces 399 nm and 935 nm light, and their beam pathways include isolators to prevent back-reflection into the laser cavity, and both of these beams are sent to the trap through fiber coupling. The Lighthouse Photonics Sprout laser generates a beam with a wavelength of 532 nm CW with an output of up to 10 W, and this green light is aligned into the SolsTiS-SRX from M Square, which subsequently outputs frequency-locked 740 nm light. An external cavity doubler (ECD-X) frequency doubles 740 nm light with output less than 1 W(10 W Sprout output causes 1W ECD output). The 369 nm light output from the ECD is split into four beams, which are Doppler, Protection, Detection, and Optical Pumping, by polarizing beamsplitter (PBS) cubes. The 14.7

GHz EOM(Qubig EO-WG14.7M-VIS) and 2.1 GHz EOM (Qubig EO-EO-Yb171+) are set along the pathway of Doppler and Optical Pumping beam, respectively. We set half-wave plates (HWP) to control relative power of each beam and these beams are focused into the AOMs with 100 mm telescoping lenses. The 399 nm, 935 nm, and 369 nm beams are combined along the same pathway through the final 150 mm best-form lens with a minimum waist size of 100 um at the ion in the trap center. The output power at the last fiber coupler is listed here, Doppler: 100 uW, Detection: 40 uW, Optical pumping 350 uW, 399 nm: 2 mW, and 935 nm: 11 mW. A small portion of all these lasers, called pickoff, are sent to the Wavelength Meter (HighFinesse WS8-10), which can give absolute accuracy within 10 MHz.

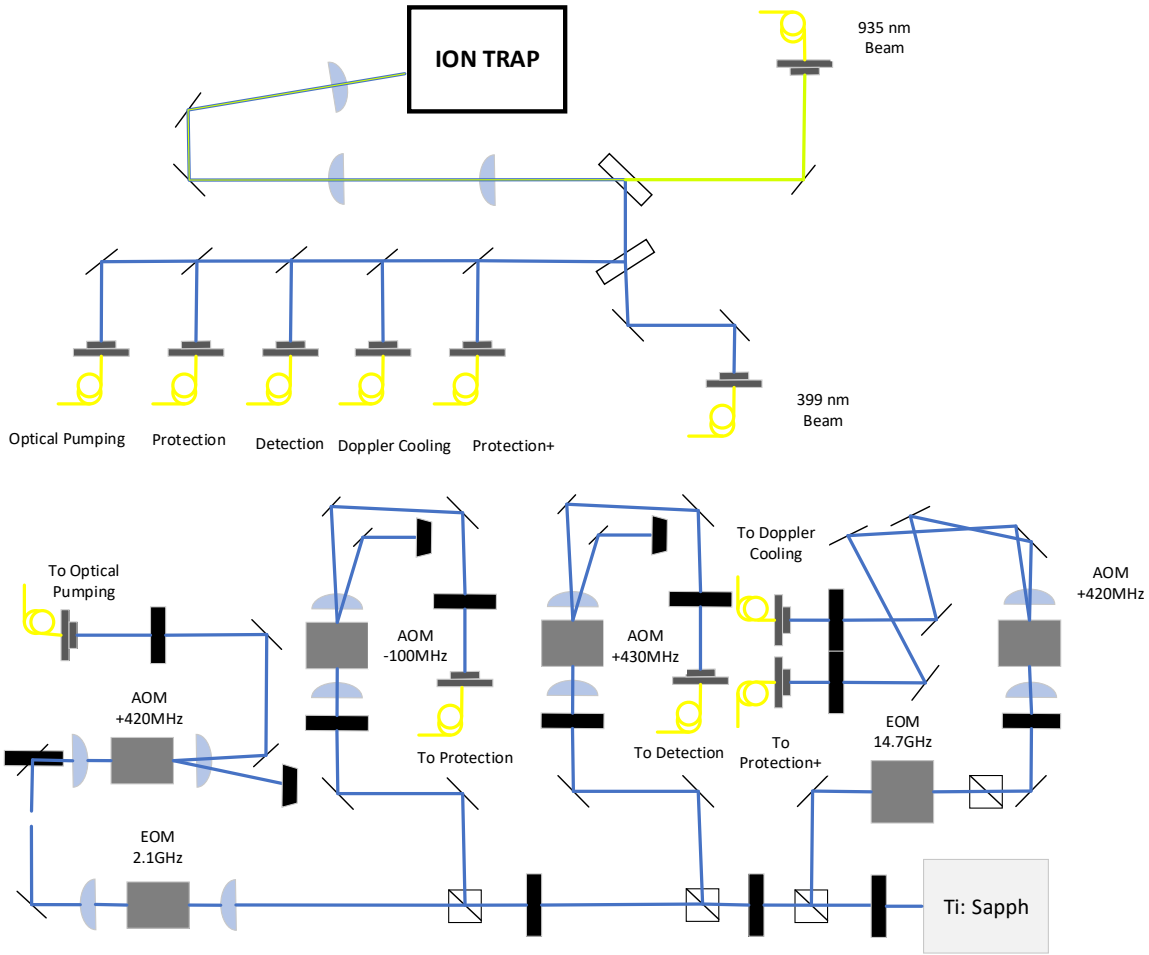

Figure 4.5: Optical pathways of near-resonant lasers.

4.5 Coherent Operations

4.5.1 Stimulated Raman Transition

Once the population concentrate into state $|\downarrow\rangle$ by optical pumping, we can apply microwave magnetic fields or stimulated Raman beams to manipulate it. Since the microwave field does not have sufficient momentum to excite the vibrational modes of the ion crystal, stimulated Raman coupling is ideal for us to perform quantum simulation. As shown in Fig.4.6, the spin states $|\uparrow\rangle$ and $|\downarrow\rangle$ are coupled to the excited state $|e\rangle$, which are detuned by a frequency Δ, via the two CW laser field at frequency ω_1 and ω_2. This Λ system can approximate the dynamics of the two-level system with spin states $|\uparrow\rangle$ and $|\downarrow\rangle$. And the effective Hamiltonian is given by:

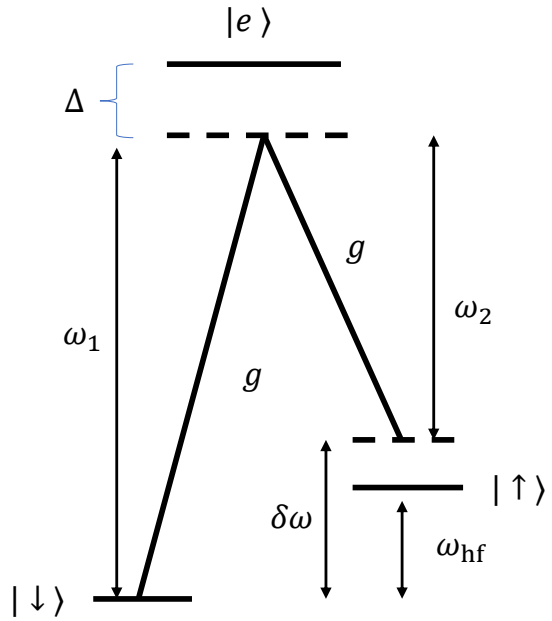

Figure 4.6: Two photon stimulated Raman transition in a Λ system:

$$H_{eff} = -\frac{|g|^2}{2\Delta}\mathbf{I} - \frac{\Omega}{2}e^{i(\Delta\mathbf{k}\cdot\mathbf{r}-[\omega_{hf}-\delta\omega]t-\phi)}\sigma^- - \frac{\Omega}{2}e^{i(\Delta\mathbf{k}\cdot\mathbf{r}+[\omega_{hf}-\delta\omega]t-\phi)}\sigma^+ \tag{4.1}$$

where g is the single photon Rabi frequency, $\Delta\mathbf{k}$ is the difference in momenta of the laser beams (Raman beat-note momentum), ϕ is the offset phase, and r is the atom's position vector. $\sigma^- = |\downarrow\rangle\langle\uparrow|$

and $\sigma^+ = |\uparrow\rangle\langle\downarrow|$ are the raising and lowering operators.

Setting the $\delta\omega = \omega_{hf} + \delta_{carr}$ and absorbing $\Delta\mathbf{k}$ in the phase ϕ, we get the effective Hamiltonian for carrier transition, as shown in Eq.4.2.

$$H_{eff} = -\frac{\Omega}{2}(e^{-i(\delta_{carr}t+\phi)}\sigma^+ + e^{i(\delta_{carr}t+\phi)}\sigma^-) \tag{4.2}$$

For $\delta_{carr} = 0$, it generates the resonant carrier transition between the spin states, at a Rabi frequency Ω.

$$\begin{aligned} H_{eff} &= -\frac{\Omega}{2}(e^{-i\phi}\sigma^+ + e^{i\phi}\sigma^-) \\ &= -\frac{\Omega}{2}(\sigma_x \sin\phi + \sigma_y \sin\phi) \\ &= -\frac{\Omega}{2}\sigma_\phi \end{aligned} \tag{4.3}$$

We assume the momentum difference is along the x direction, the position coordinate of the ion at frequency ω_X can be expressed as Eq.4.4 when the temperature of the ion is cold enough,

$$\hat{X}(t) = X_0(\hat{a}e^{-i\omega_X t} + \hat{a}^\dagger e^{i\omega_X t}). \tag{4.4}$$

where $X_0 = \sqrt{\hbar/2m\omega_X}$ is the characteristic length scale of the motional mode, and $\hat{a}$ and $\hat{a}^\dagger$ are phonon annihilation and creation operators. We set the detuning $\delta\omega = \omega_{hf} + \omega_X + \delta$ or $\delta\omega = \omega_{hf} - \omega_X - \delta$ to excited the vibrational mode, and generate effective blue and red sideband Hamiltonian[91] with Lamb-Dicke parameter $\eta = \Delta k X_0 \ll 1$[22].

$$H_{bsb} = -\frac{\eta\Omega}{2}(\hat{a}\sigma^- e^{i(\delta t+\phi)} - \hat{a}^\dagger\sigma^+ e^{-i(\delta t+\phi)}) \tag{4.5}$$

$$H_{rsb} = -\frac{\eta\Omega}{2}(\hat{a}^\dagger\sigma^- e^{-i(\delta t-\phi)} - \hat{a}\sigma^+ e^{i(\delta t-\phi)}) \tag{4.6}$$

H_{bsb} makes the transitions $|\downarrow, n\rangle$ to $|\uparrow, n+1\rangle$ with blud sideband Rabi frequency $\eta\Omega\sqrt{n+1}$, and H_{rsb} makes the transitions $|\downarrow, n\rangle$ to $|\uparrow, n-1\rangle$ with red sideband Rabi frequency $\eta\Omega\sqrt{n}$. One

application for stimulated Raman transition is sideband cooling which we will discuss in Chapter 5. We can also apply Raman laser beams to excite the vibrational modes off-resonantly to generate Mϕlmer-Sϕrensen (MS) gate to form entanglement and Ising Interactions[91, 22, 92].

4.5.2 Raman Beam

Our high power(up to 8 W) mode-locked COHERENT UV Paladin produces 355 nm picosecond pulse laser as Raman beams. The beam pathway is illustrated in Fig.4.7, the output is split into two beams, and each of the arms has its frequency comb with an 80.935 repetition rate. Two 200 MHz AOM (Brimrose CQF-210-40-355) are used to control the frequency, phase, and amplitude of Raman beams. The inner arm is used for beat note lock, driven by a single frequency AOM. The outer arm is driven with multiple frequencies. Both two beams are focused by the best-form lenses near the trap and generate the resultant wavevector $\Delta\mathbf{k} = k_1 - k_2$. There is a delay stage (not shown in Fig. 4.7) in one of the arms to adjust the beam path length to ensure the same path length to avoid phase difference, and every beam needs to align and overlap with the ion carefully. Once an ion is trapped, we perform Ramsey and Rabi experiments using the microwave horn[93] to do the spatial and temporal alignment of Raman beams.

Ramsey Experiment: we perform Ramsey experiments to align the Raman beam by using the microwave horn, the experiment sequence for Ramsey experiment:

Doppler cool $\rightarrow$ Optical pumping $\rightarrow$ $\pi/2$ microwave pulse $\rightarrow$ Delay time $\rightarrow$ $\pi/2$ microwave pulse $\rightarrow$ Detect

The bright state oscillates with frequency δ, which is the detuning of the qubits transition (ω_{hf}). Turning on the Raman beam during the delay time will create a two-photon Stark shift; better alignment means a more significant Stark shift, creating larger imperfections in the $\pi/2$ pulses and causing higher oscillating frequency.

Rabi Oscillation: we perform Rabi oscillation experiments to optimize the temporal alignment

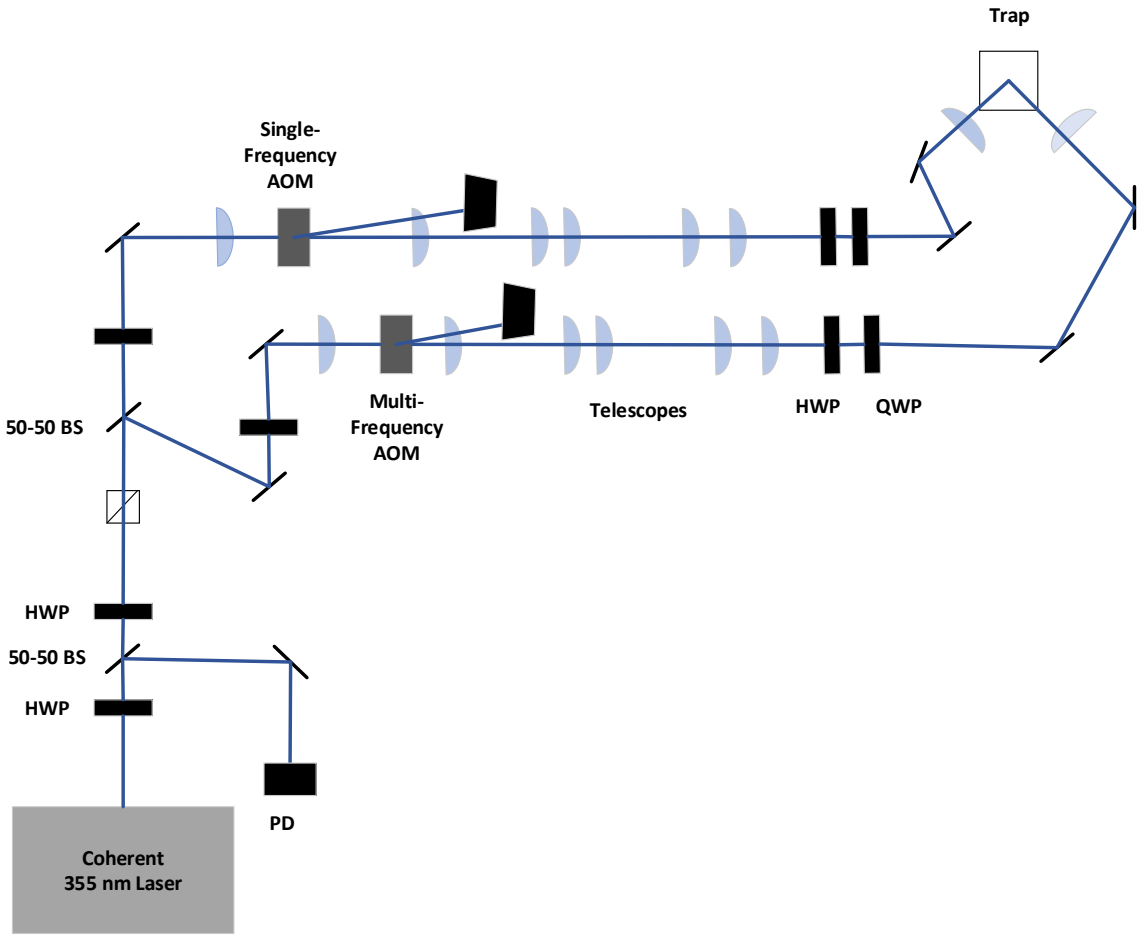

Figure 4.7: Optical pathways of 355nm beam.

of both arms, the experiment sequence for Rabi experiment:

Doppler cool → Optical pumping → Raman pulse of time t → Detect

The Rabi frequency scales with laser intensity$\Omega_R \propto \sqrt{I_1 I_2}$, we adjust the delay stage and beam alignment until the Rabi frequency can no longer be increased.

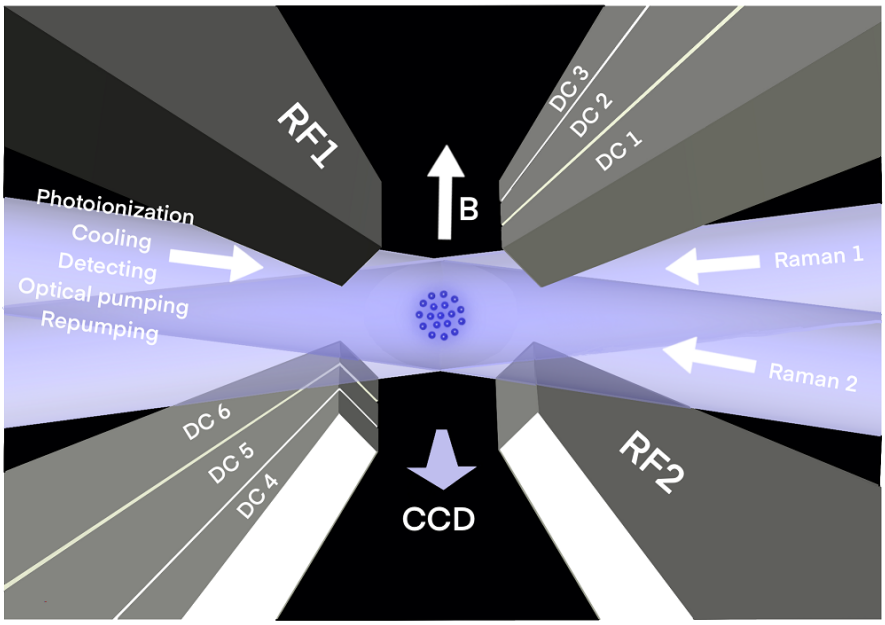

Figure 4.8: Concept drawing of the trap and laser beam configurations for photoionization (399 nm), cooling, optical pumping, and detection (369.5 nm), repumping (935nm), and two-photon Raman transitions (355nm). The CCD camera faces the crystal plane, and the magnetic field is oriented vertically. Oscillating voltages on electrodes RF1 and RF2 provide radial confinement, while static voltages applied to electrodes DC1, DC3, DC4, and DC6 provide axial confinement.

4.6 Trapping Ions with 2D Ion Trap

4.6.1 2D Ion Crystal

Ions may be confined in radial-2D crystals once the trap secular frequencies satisfy the inequality in Eq. 2.26. To create this ion geometry experimentally, we load the desired number of ions at low axial frequency ω_z, then increase the endcap voltages (DC1, DC3, DC4, DC6) to push the ions into the radial-2D phase. In practice, imperfect electrode fabrication, trap misalignments, and stray electric fields could cause ion heating during the transitions through different structural phases. To avoid losing ions and to minimize any excess micromotion, we compensate by applying small bias voltages to blade segments as needed. Once ions are in the 2D regime and Doppler-cooled to milliKelvin temperatures, they form a Wigner crystal as the system minimizes its configuration energy. As shown in Fig. 4.9, the final crystal geometry forms a triangular lattice in the radial plane.

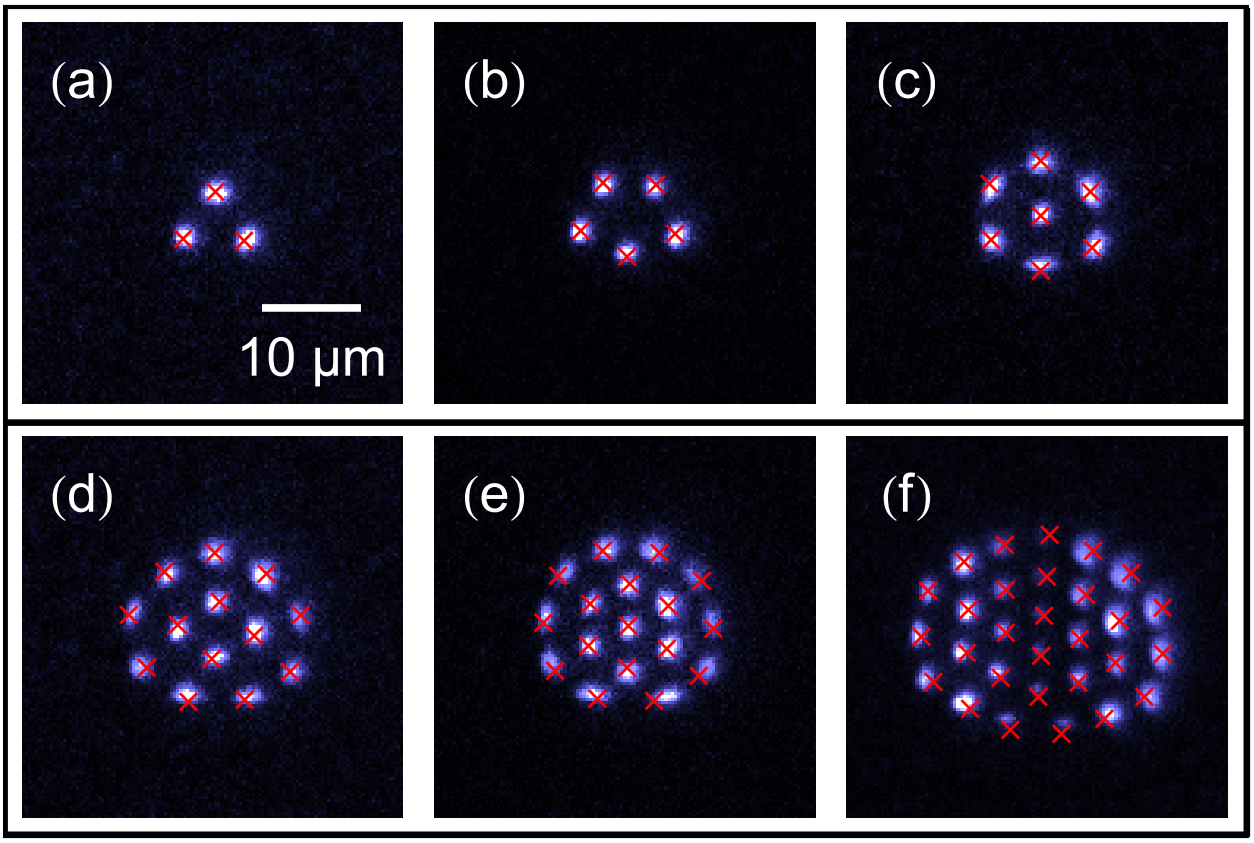

Figure 4.9: CCD images of crystals with 3, 5, 7, 13, 17, and 29 ions trapped in the radial-2D crystal phase, with measured center-of-mass frequencies $\omega_x = 2\pi \times 0.416$ MHz, $\omega_y = 2\pi \times 0.446$ MHz, $\omega_z = 2\pi \times 1.124$ MHz. Red crosses show the ion positions predicted under the pseudopotential approximation

Once the trap frequencies are experimentally known, the ion positions can be predicted under the pseudopotential approximation. To measure the ion secular frequencies for a set of applied trap voltages, we inject an additional small rf voltage on the trap electrode DC 3 following Doppler cooling. This electrode is chosen since its contribution to the electric field at the ion has components along the $\hat{x}$, $\hat{y}$, and $\hat{z}$ directions. Suppose the injected rf drive is in resonance with the ion's oscillation frequency. In that case, the ion will absorb energy and heat up, decreasing its fluorescence when probed with a detection laser beam [94]. Once the frequencies are determined, we use the procedure outlined in Sec 2.3 to predict the ion positions in the radial-2D crystal; results are shown as red crosses in Fig. 4.9.

Compared to the one-dimensional case, more complex processes are involved when laser

cooling ion crystals in two- and three-dimensions. Ions away from the trap center experience micromotion, which leads to Doppler-shifted cooling transitions which depend on the micromotion amplitude at each ion position. For large crystals, this micromotion-induced Doppler shift can lead to dramatically different cooling rates for a crystal's outermost ions compared to the inner ions [95]. Optimum Doppler cooling is often found further red-detuned than the typical single-ion detuning, which may result in relatively decreased fluorescence for the innermost ions (as seen in Fig. 4.9(f)). For huge crystals, it may be necessary to introduce multi-tone Doppler cooling to frequency-address ions at different radii, or to power-broaden the resonant transition as suggested in [95].

4.6.2 Ion Trajectories Analysis

In radial-2D crystals, ions located far from the original experience the largest amplitude of micromotion. Following the process outlined in Chapter 2, we calculate that the maximum radial micromotion amplitude in a 17-ion radial-2D crystal is < 650 nm, which is small compared to the ~ 1 μm diffraction-limited spot size of our imaging system as well as the 5 μm inter-ion spacing. The micromotion along the axial direction is calculated to be negligible due to the small Mathieu q_z parameter; this was confirmed in prior measurements using the "needle trap" geometry, where the radial-2D crystal was imaged from the side [55]. Since the out-of-plane axial modes remain micromotion-free in this geometry, these modes will be preferable for performing future quantum simulation experiments.

Close inspection of the ion trajectories in Fig. 4.9 reveals a convex curvature rather than the concave curvature which would be expected from driven micromotion (see Fig. 2.4(b)). We attribute this result to thermally-driven, small-angle rotations of the ion crystal. Consider, for instance, a radial-2D crystal in a perfectly-symmetric potential with degenerate radial secular frequencies. The crystal will be free to rotate with no energy penalty; when imaged on a CCD camera, the ions will appear as concentric rings. Although this degeneracy is explicitly broken in our trap, residual thermal energy in the crystal may still induce small azimuthal oscillations. Additionally, a

melting transition occurs for 2D crystals when the Mathieu a and q factor varies within the stability diagram [96]. This kind of orientational melting, which is brought on by thermal or quantum fluctuations[97], causes the system to stay radially localized while the particles are delocalized into concentric circular paths. As expected from the non-universality of the phenomena, previous experiments have found that adding or deleting a single particle can have drastically different collective features, and there are specific "magic numbers" of particles for which orientational melting is particularly unfavorable [98].

We calculate that the ion excursions observed in Fig. 4.9(e)-(f) are consistent with crystal temperatures of only $\approx$ 20 mK. We anticipate that this effect can be reduced by further breaking the degeneracy between the radial secular frequencies, by introducing multi-tone Doppler cooling [95], or by applying sub-Doppler cooling techniques such as resolved sideband cooling [22, 99] or Electromagnetically-Induced Transparency (EIT) cooling [54, 100, 101].

CHAPTER 5

Optimized pulsed sideband cooling and enhanced thermometry of trapped ions

5.1 Coherent manipulation and Sideband cooling

Laser cooling of trapped ions was briefly described in Section 4.2; this gives the lowest temperature scaling as $\hbar\Gamma/k_B$. It's in a limit where the natural width Γ of the excited state is large compared to the vibration frequency ω of the ions in the trap, the motion of the ion during the characteristic time $1/\Gamma$ is small compared to the amplitude of the vibrational motion of ions under this condition. There are several mechanisms proposed for going below the Doppler cooling limit. One prevalent method we present here, resolved sideband cooling[102] allows ions to be accumulated in the lowest vibrational level of the trap.

Resolved SBC enables sub-Doppler cooling of the ion temperature when a trapped ion of mass m is constrained to a one-dimensional harmonic potential of frequency ω. We assume that the ion has been Doppler cooled using a transition of linewidth to the Doppler cooling limit $\bar{n}_i = \Gamma/2\omega$ [103, 104], following the Doppler cooling, the thermal distribution well describes the probability of finding the ion in the nth harmonic-oscillator level

$$p_{th}(n) = \frac{\bar{n}^n}{(\bar{n}+1)^{n+1}} \tag{5.1}$$

which is solely parametrized by the average harmonic state of the ion $\bar{n}$.

5.2 Optimized pulsed sideband cooling

5.2.1 Classical Protocol

Typically, far-detuned Raman transitions of wavelength λ and linewidth $\Gamma \ll \omega$ are used to manipulate the electronic and motional states of the ion. Detuning the Raman frequency by integer multiples of the trap secular frequency ω excites a sideband transition, coupling spin flips to a change in motional state from $|n\rangle$ to $|n'\rangle$, at Rabi rate [22, 102]

$$\Omega_{n,n'} = \Omega e^{-\eta^2/2} \sqrt{\frac{n_<!}{n_>!}} \eta^{|n-n'|} \mathcal{L}_{n_<}^{|n-n'|}(\eta^2), \tag{5.2}$$

where $n_<$ ($n_>$) is the lesser (greater) of n and n',

$$\mathcal{L}_n^{(\alpha)}(X) = \sum_{i=0}^{n} (-1)^i \binom{n+\alpha}{n-i} \frac{X^i}{i!} \tag{5.3}$$

is the generalized Laguerre polynomial, and

$$\eta \equiv \Delta k x_0 = 2 \sin(\theta/2) \frac{2\pi}{\lambda} \sqrt{\frac{\hbar}{2m\omega}}. \tag{5.4}$$

is the Lamb-Dicke parameter for counter-propagating Raman beams intersect at an angle θ. In this article, we will refer to an $n - n' = 1$ transition as a first-order red sideband (RSB) transition and an $n - n' = -1$ transition as a first-order blue sideband (BSB) transition.

A traditional pulsed SBC protocol (which we will call the "classic" protocol) is executed as follows in the references [99, 105]. After Doppler cooling to an average harmonic occupation $\bar{n}_i$, and optical pumping to the qubit state $|\downarrow\rangle$, an initial motional level $n_i \gg \bar{n}_i$ is selected as the entry point for SBC. A first-order RSB π-pulse is then applied for $t = \pi/\Omega_{n_i,n_i-1}$ followed by fast optical pumping, to drive the transition $|\downarrow, n_i\rangle \rightarrow |\downarrow, n_i - 1\rangle$. Then another iteration is performed using $t = \pi/\Omega_{n_i-1,n_i-2}$, and so on, until the sequence concludes with a final $t = \pi/\Omega_{1,0}$ pulse, as we can see in Fig.5.1, this protocol sweeps the fraction of population for which $n \leq n_i$ into the motional

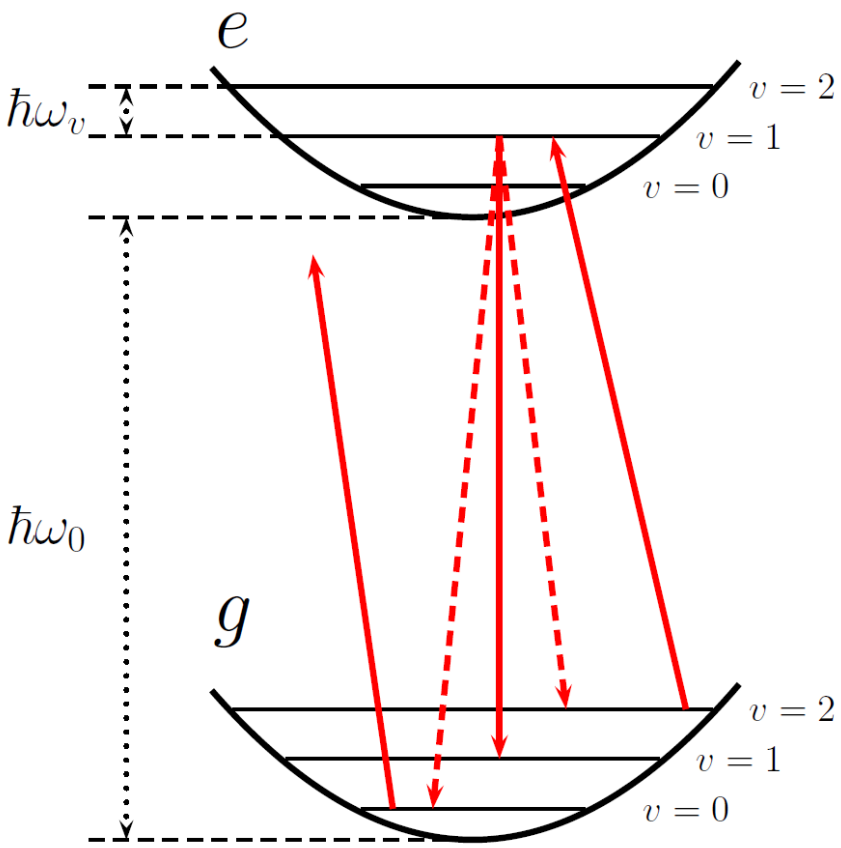

Figure 5.1: Principle of resolved sideband cooling.

ground state. In principle, sideband cooling works when the vibration frequency ω is larger than the natural width Γ of the excited state ($\omega \gg \Gamma$) and to the recoil frequency $E_{rec}/\hbar$ (Lamb-Dicke limit) $\omega \gg E_{rec}/\hbar$. By starting at larger n_i and iterating for more pulses, the classic SBC protocol can theoretically reach the SBC limit of $\bar{n}_{\min} \approx (\Gamma/2\omega)^2 \ll 1$ [22, 106, 102, 107]. To further improve the cooling efficiency, we propose several protocols.

5.2.2 Fixed protocol and Optimal protocol

Following the graph-theoretic framework[108], we have these fixed and optimal protocols. We start by thinking about a single-parameter optimization that we refer to as the "fixed" protocol. The duration of each SBC pulse is set to be the same $T_{\text{fixed}} = \{t_0, \ldots, t_0\}$, which is akin to SBC techniques used in several trapped-ion investigations [109, 64, 110]. The fixed protocol explicitly

seek to minimize the function

$$\bar{n}(t_0) = \sum_{n=0}^{n_{\max}} n \left[W^N(t_0) \vec{p}_{\text{th}} \right]_n \tag{5.5}$$

to find the time t_0 which yields the lowest possible $\bar{n}$ given N identical SBC pulses, where the upper triangular matrix $W(t)$ and the initial vertex values vector p_{th} are defined in Equation (5) of reference[108].

The optimal protocol is a full-parameter optimization, which treats each pulse duration as an independent variable. For each given value of η, $\bar{n}_i$, Ω, and N, it searches the whole parameter space of N distinct pulse times, returning the lowest possible $\bar{n}$. The optimal protocol executes as follows. First, the initial harmonic populations $\vec{p}_{\text{th}}$ and Rabi frequencies $\Omega_{n,n-1}$ are calculated over a truncated range of harmonic states $[0, n_{\max}]$ ($n_{\max} \gg \bar{n}_i$), based on the experimental parameters η, $\bar{n}_i$, and Ω. Next, a gradient descent algorithm is used to minimize the equation.

$$\bar{n}(t_0, t_1, \ldots, t_{N-1}) = \sum_{n=0}^{n_{\max}} n \left[W(t_{N-1}) \ldots W(t_1) W(t_0) \vec{p}_{\text{th}} \right]_n \tag{5.6}$$

to get the pulse schedule $T_{\text{optimal}} = \{t_0, t_1, \ldots, t_{N-1}\}$ that gives the lowest average harmonic occupation $\bar{n}(t_0, t_1, \ldots, t_{N-1})$ following N SBC pulses.

As shown in Fig. 5.2 (b), the total SBC time depends on the number of the pulses (we set 50 cooling pulses for our experiments), for the classic method, is higher than the fixed and optimal method and the fixed and optimal protocol are nearly identically in both overall cooling time and final ion temperature.

5.2.3 Multiorder optimization protocol

The classical and optimal protocol only considers the first order of sideband cooling, when outside of the low η-$\bar{n}_i$ regime and the harmonic population is trapped in high-n states, the first-order RSB cooling can be limited[64, 110, 111]. As shown in Fig. 5.2(c), the first-order RSB Rabi frequency approaches zero for specific high-n harmonic levels, which is approximately $n = 112$ for our chosen parameters. Consequently, any initial population $n \gtrsim 112$ will be trapped in these

high-n states, even while the remaining population $n \lesssim 112$ is swept towards the ground state. We apply 50 first-order SBC pulses, and as we can see, the population trapping effect is visible in Fig. 5.2(d). Near $n = 112$, a sizeable population is still uncooled, adding roughly 0.3 motional quanta to the final value of $\bar{n}$, which is an order of magnitude higher than the SBC cooling limit and larger than what is typically regarded as near-ground-state cooling. The trapped population contributions to $\bar{n}$ predominate at cooler temperatures; this effect also explains why the three first-order methods in Fig.5.2(a)-(b) begin to converge at large numbers of pulses.

To avoid population entrapment at high-n, higher-order RSB pulses can be introduced into the SBC protocol using our "multiorder" cooling approach. Larger portions of the initial population will be trapped at high-n as $\bar{n}_i$ climbs and the harmonic levels with near-zero RSB Rabi frequencies shift to smaller n as η increase, trapped populations are significant, especially in experimental regimes where η or $\bar{n}_i$ are large. Thus multiorder cooling is required to achieve near-ground-state temperatures [64, 110, 111]. The probability that the m^{th} order pulse takes $|n\rangle \rightarrow |n-m\rangle$ is calculated by $b_n(t) = \sin^2(\Omega_{n,n-m}t/2)$, then this probability is mapped to the m^{th} upper diagonal of $W(t)$. Once the $W(t)$ matrices are determined, the fixed and optimal protocols may be calculated for multiorder cooling.

We simulate and optimize a multiorder fixed protocol with N_3 third-order pules, N_2 second-order pulses, and N_1 first-order pulses and we fix the total number of SBC pulses $N = N_1 + N_2 + N_3$. The pulse time is allowed to vary per order $\bar{n}(t_1, t_2, t_3) = \sum_{n=0}^{n_{\max}} n \left[W^{N_1}(t_1)W^{N_2}(t_2)W^{N_3}(t_3)\vec{p}_{\text{th}}\right]_n$. N_1, N_2, and N_3 were selected by optimization of a block sequence[108]. Multiorder cooling (dash-dotted purple) works substantially more quickly than the optimal first-order approach, cooling from $\bar{n}_i = 15.36$ to a final $\bar{n} = 0.06$ after only 50 pulses (see Figure 5.2(b)). Additionally, the multiorder protocol avoids the high-n population trapping in the first-order sequences. This is demonstrated in Fig. 5.2(d), where the population is transferred from high-n to low-n far more effectively when multiorder pulses are used.

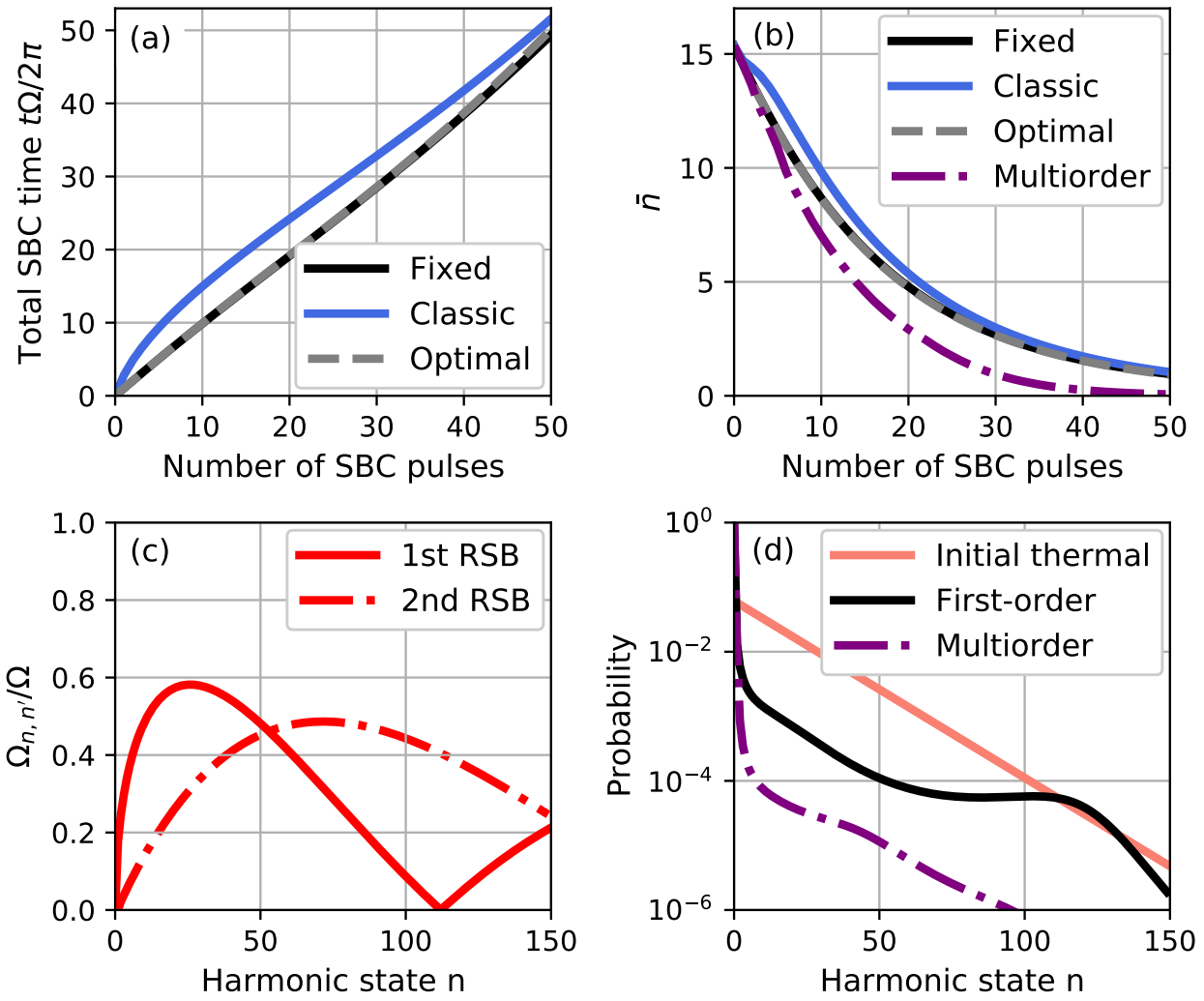

Figure 5.2: The classic, fixed, optimal, and multiorder protocols are compared for an initial temperature of $\bar{n}_i = 15.36$, and $\eta = 0.18$ (see text for definitions). (a) The total sideband cooling time (excluding optical pumping), and (b) the cooled $\bar{n}$ as a function of the number of SBC pulses. (c) Scaled frequencies for the first-order (solid) and second-order (dash-dot) RSB showing the near-zero frequency of the first-order RSB at $n = 112$. (d) Initial thermal distribution (solid light red) and distributions after 50 pulses of first-order fixed (solid black) and multiorder fixed (dash-dotted purple).

5.3 Thermometry of Sideband-cooled Distribution

Nearly all experiments measuring trapped-ion temperatures deep in the quantum regime follow the approach used in Ref. [99], which is the classical ratio method. The first-order red and blue sidebands are driven with the same power for the same duration once the ion has been initiated in the state $|\downarrow\rangle$. The ratio of RSB to BSB transition probabilities can be linked to the average harmonic

level occupation $\bar{n}$ if the ion motional distribution is thermal:

$$r \equiv \frac{P_{\uparrow}^{\mathrm{RSB}}(t)}{P_{\uparrow}^{\mathrm{BSB}}(t)} = \frac{\bar{n}}{\bar{n}+1}. \tag{5.7}$$

However, the ratio method assumes a thermal harmonic distribution that is inherently unsuitable to the motional distribution of ions following significant sideband cooling (see Fig. 5.2(d)). As we will show in Sec. 5.4, after only moderate sideband cooling, this assumption may result in an order-of-magnitude underestimation of the ultimate $\bar{n}$. Alternative thermometry techniques may offer a more accurate estimate of $\bar{n}$ when the underlying motional distribution is known to be non-thermal. One common technique analyzes a BSB Rabi oscillation in the frequency domain while extracting the harmonic level probability $p(n)$ via singular value decomposition (SVD)[112]. In this method, a BSB oscillation is described as a matrix of transition probabilities $b_n(t_i) = \sin^2(\Omega_{n,n-1}t_i/2)$ acting on the level probability vector $\vec{p}$ to yield the measured fluorescence at each timestep t_i. SVD is then used to pseudo-invert the transition probability matrix and isolate the vector of $p(n)$'s.[108]. This method has been used to measure $\bar{n}$ for both thermal states, and coherent states with success [112].

5.3.1 Time-average thermometry

We propose a “time-average" measurement protocol that provides a high-accuracy estimate of $\bar{n}$ following SBC. This approach is constructed to measure the individual probabilities of the first few harmonic levels. We observe that for long times ($t \gg 1/(\Omega_{n+m,n}^2 + \gamma^2)$), where decoherence effects at rate γ, the time average converge to a partial sum of motional state probabilities with the mth order red sideband pulse gives[108]:

$$\bar{P}_{\uparrow,m}^{\mathrm{RSB}}(t) \approx \frac{1}{2}\sum_{n=0}^{\infty} p(n+m). \tag{5.8}$$

To extract the individual harmonic probabilities, consider driving with a first-order RSB:

$$\begin{aligned}\bar{P}^{\mathrm{RSB}}_{\uparrow,1}(t) &\approx \frac{1}{2}\sum_{n=0}^{\infty} p(n+1) \\ &\approx \frac{1}{2}\left[1 - p(0)\right] \end{aligned} \tag{5.9}$$

from which $p(0)$ can be directly estimated

$$p(0) \approx 1 - 2\bar{P}^{\mathrm{RSB}}_{\uparrow,1}(t). \tag{5.10}$$

Higher harmonic state probabilities may then be estimated by driving with sequentially higher-order RSBs and applying the recursion relation

$$p(m-1) \approx 2(\bar{P}_{\uparrow,m-1} - \bar{P}_{\uparrow,m}). \tag{5.11}$$

This time-average method offers a reliable and effective way to extract populations of motional states. Compared to other methods, only a small number of data points are required to calculate the temporal average of the RSB oscillation. Although these points should be taken at long times (relative to the RSB Rabi frequency), we note that Eq. (5.8) does not depend on the decoherence rate γ, and indeed converges faster when decoherence is included. Rather, we anticipate that the largest errors in time-average measurements will arise from real-time changes in $p(n)$ driven by motional heating. Such trap heating effects have been comprehensively studied [80] and can be incorporated into the motional state analysis if needed.

5.4 Experimental Thermometry

We experimentally demonstrate the effectiveness of our time-averaged thermometry method. We begin by measuring the temperature of a trapped ion following Doppler cooling and comparing the time-average method to several existing techniques. Then, we repeat our measurements and

comparisons using an optimized sideband cooling sequence from Sec. 5.2, finding that the time-average method most closely agrees with theory predictions.

Thermometry experiments are performed on a single $^{171}Yb^{+}$ ion confined in a linear Paul trap with axial frequency $\omega_z = 2\pi \times 0.670 \pm 0.008$ MHz. In our setup, the Lamb-Dicke parameter $\eta = 0.18 \pm 0.01$, the Rabi carrier frequency $\Omega = 2\pi \times 64.9 \pm 0.5$ kHz, and the optical pumping time is 5 μs. Doppler cooling is performed with 369.5 nm light along the $^2S_{1/2}|F = 0\rangle \rightarrow {}^2P_{1/2}|F = 1\rangle$ and $^2S_{1/2}|F = 1\rangle \rightarrow {}^2P_{1/2}|F = 0\rangle$ transitions (linewidth $\Gamma = 2\pi \times 19.6$ MHz), while red and blue sideband transitions are performed with far-detuned Raman beams at 355 nm. After each experiment, the qubit state is determined by irradiating the ion with 369.5 nm light resonant with the $^2S_{1/2}|F = 1\rangle \rightarrow {}^2P_{1/2}|F = 0\rangle$ transition and capturing the spin-dependent fluorescence on a photomultiplier tube.

Fig. 5.3 shows the experiment results of thermally-distributed ion motional states; we compare different thermal evaluations. After Doppler cooling the ion, the calculated the Doppler cooling limit is $\bar{n}_{Dop} = 14.6$. Among these evaluations, the standard ratio, time average, and thermal fit method agree with the simulated Doppler limit result, except for the SVD method, which is overestimated. The thermometry methods comparison among sideband cooled ion proves that our time average method gives the most accurate results, and other methods are either over or under-estimated.

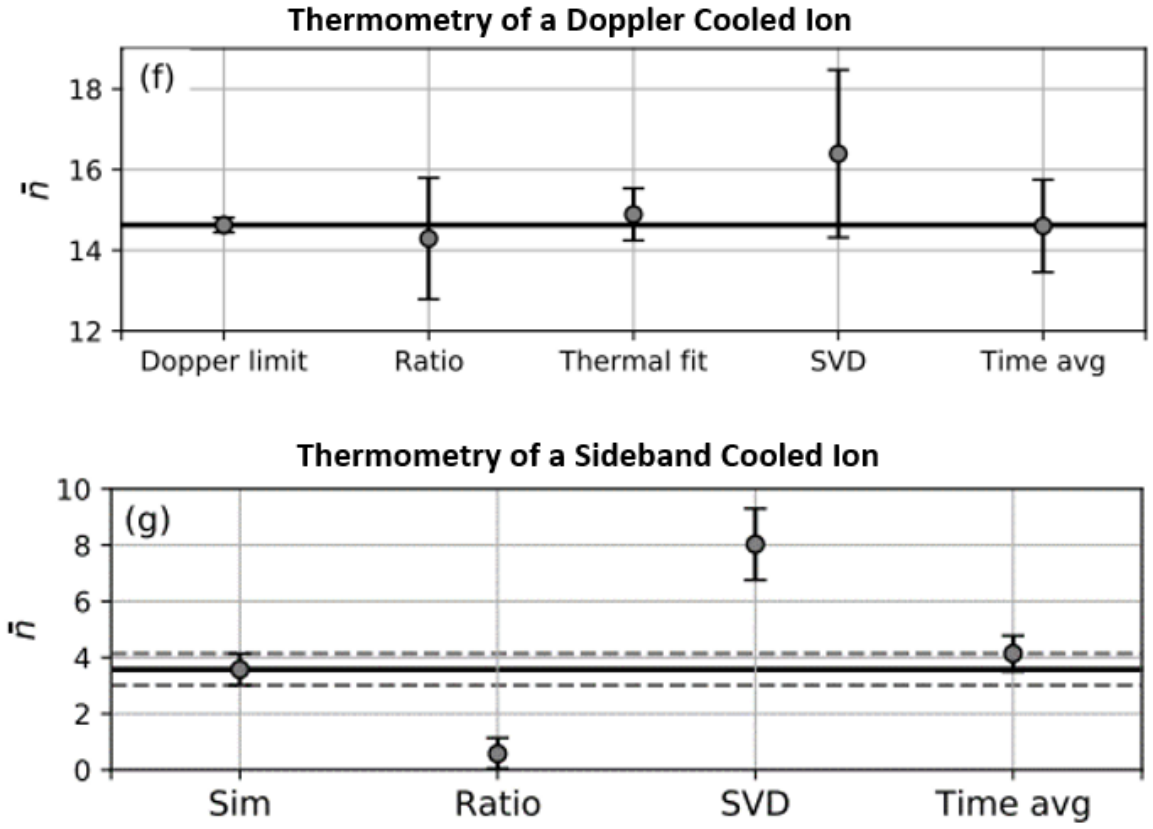

Figure 5.3: Thermometry comparisons of thermally-distributed ion motional states.

CHAPTER 6

Characterization of Radial-2D Crystals in a Linear Paul Trap

6.1 Overview

This section will introduce the thermal characterization of this radial two-dimensional crystal we created. This experiment was done before we fabricated the 2D trap. Thus the 2-dimensional crystal was created inside a regular rod trap (see Fig. 6.1), and we characterize the feature of the crystal from the side direction (radial direction). We first identified the structure phase transition caused by the different voltages we applied to the electrodes. Next, we measure the heating rate of the crystal to observe that micromotion-induced heating of the radial-2D crystal is confined to the radial plane, but this measurement is global and does not sensitive to axial direction; we look for evidence of heat transfer between the radial and axial directions, then we measure the axial heating rate of a single ion and a crystal with seven ions in 2 dimensions, and we find that the axial heating rate is over 200 times smaller than the radial heating rate.

In Radio-Frequency Trap, there are two types of methods to get a two-dimensional ion lattice: the lateral-2D configuration and d the radial-2D configuration. The lateral-2D configuration extends from the well-known "zig-zag" phase, its 2D plane defined by one axial and one radial trap axis; the crystal usually has an elliptical shape with the long axis of the ellipse along the trap axial axis, as shown in the left graph on Fig. 6.2. In this case, the rf-driven micromotion is present along one of the in-plane directions (along y axis in Fig.6.2).

Our radial 2D crystal has a different transverse plane, its 2D plane is defined by two radial trap axis(x-axis and y-axis), as shown in the right graph in Fig. 6.2, and micromotion only appears on

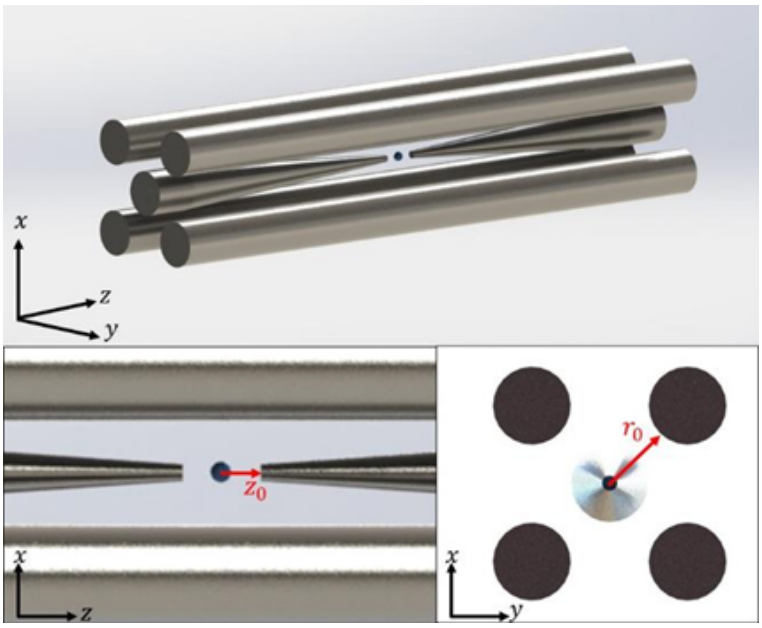

Figure 6.1: A picture of a regular rod-style Paul trap. In this design, we modified our trap to suit our case in that the distance between two endcap needles is around 335 um to avoid extremely high voltages applied to the electrodes. The trap's radius is around 460 um, the resonant frequency we applied on the trap is 21 MHz, the DC voltage is between 0.002 V to 30 V, and the rf voltage is around 340 V during the experiment.

the radial direction but micromotion free along the axial direction. This kind of phase also has been studied for several years[113]. However, experiments performed with radial-2D crystals had only demonstrated Doppler cooling [56]and probed the radial-2D phase boundary with 3-4 ions[65].

The lateral 2D and radial 2D crystal have different orientations of their transverse plane and micromotion, and micromotion-induced heating is a big concern in these studies. Our study with radial 2D crystal proves that the axial (transverse) modes of our radial 2D crystal remain cold, isolated, and well-suited for quantum simulation.

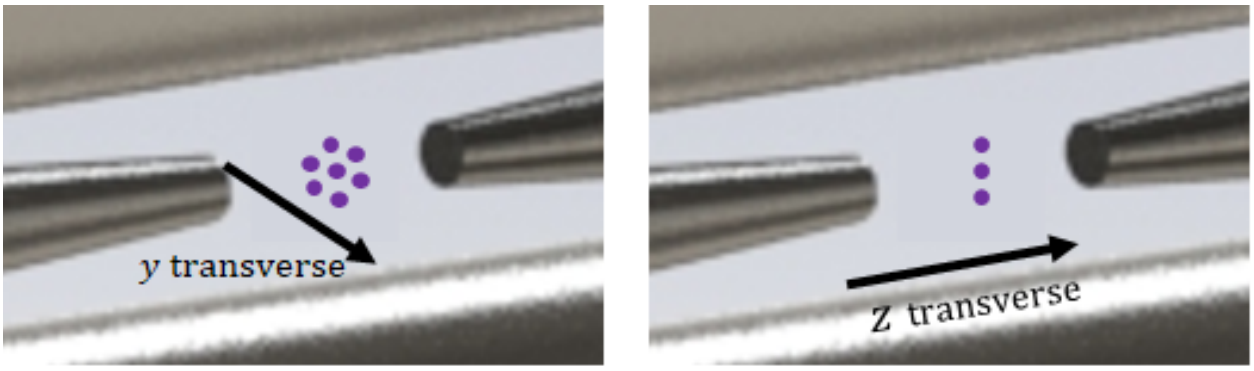

Figure 6.2: Lateral 2D and Radial 2D, the left graph shows the Lateral 2D crystal and its 2D plane defined by one axial and one radial trap axis. The right graph shows the Radial 2D crystal and its 2D plane defined by two radial trap axis.

6.2 Phase Transition and Mode Spectrum

The first study is the structure phase transition. Once we trap the desired number of ions, we can perform the phase transition process. As we defined in Chapter 2, we call the radial frequency $\omega_r = \text{Max}\ \{\omega_x, \omega_y\}$, here We introduced a slight difference between radial-x and radial-y secular frequency to prevent zero-frequency rotation mode. To describe the phase transition, we also defined the aspect ratio value $\alpha = \omega_z/\omega_r$, where ω_z is the axial secular frequency. In our experiment setup, a constant rf voltage $V_0 = 340V$ is applied on the rf electrodes which give a Mathieu q parameter $q = 0.10$, while the DC voltage varied between 0.012V to 30V.

6.2.1 Secular Frequency measurement

We take the way of injecting the rf voltage on one of the electrodes to measure the secular frequencies in three directions. Once the ion's mode resonates with the frequency we input by frequency scanning, the ion absorbs energy and begins vibrating, producing a dip in the collected fluorescence that is accurate within a kHz. Our trap design allows us to bias all electrodes. To excite the axial mode, we bias the endcap needles; to excite the radial modes, we bias one of the rf ground electrodes.

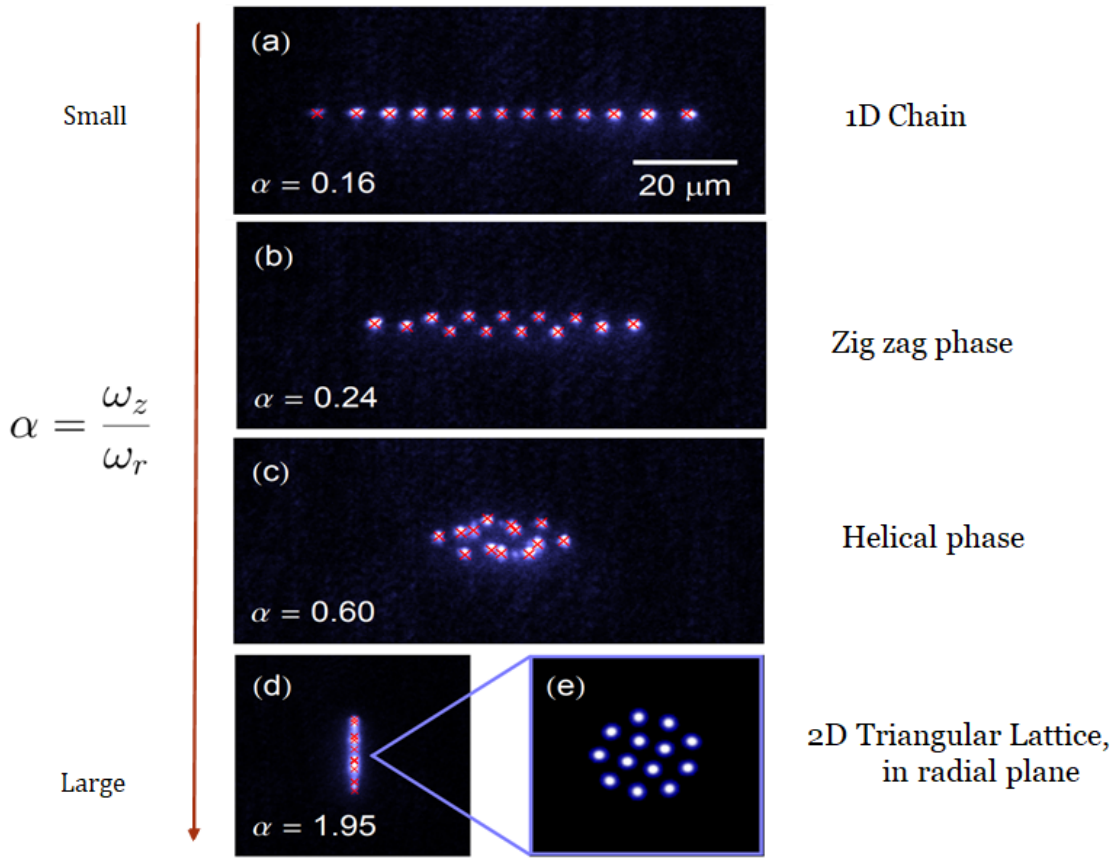

Figure 6.3: Actual photos of 13 ions from inside the trap with the blue circle are CCD images. The red crosses are the positions of the ions we simulated by pseudopotential approximation. As the DC voltage is raised, the aspect ratio $\alpha = \omega_z/\omega_r$ increases, the crystal transits from (a) 1D ion chain, (b) zig-zag phase, (c) 3D helical phase to (d) 2D triangular lattice. Simulated ion sizes in (e) correspond to the diffraction-limited spot size of our imaging optics and include effects from rf-driven micromotion.

In our experiment, we trap 13 ions to study the phase transition; we slowly increase the dc voltage to identify the boundary between different phases. When the aspect ratio α is small, ions form a 1D chain along the trap's axial axis (Fig. 6.3 (a)). As we increase the dc voltage, from equation 2.23, the axial frequency increase while radial frequency decrease a little bit, the ions pass through a zig-zag region (Fig. 6.3 (b)) and go to the 3D helical spheroidal configuration (Fig. 6.3 (c)). If push the ion cloud much more, the last stable configuration after the 3D helical phase is the 2D triangular configuration (Fig. 6.3 (d)), which is suited for our 2D quantum simulation. In our rod trap, the 2D configuration faces the endcap needle; thus, the image captured by the EMCCD camera is the side view of the crystal, Fig. 6.3(e) shows the simulated front view of the

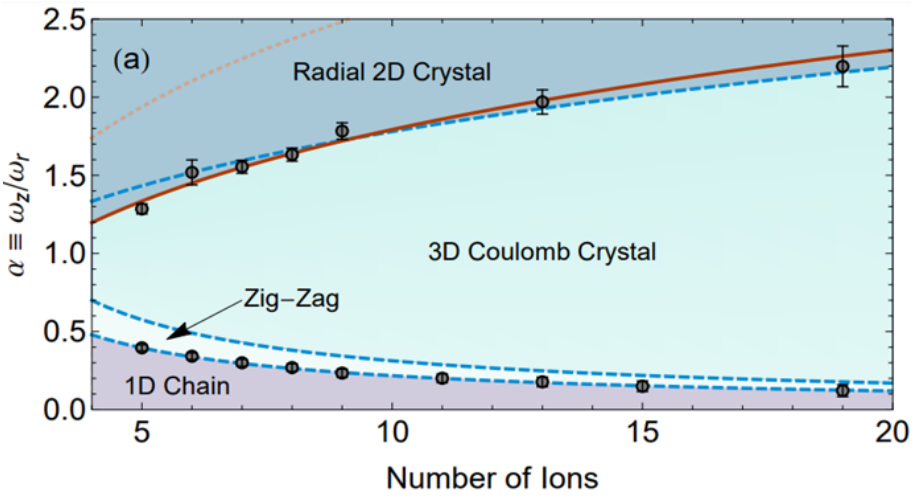

Figure 6.4: Phase boundaries of ion Coulomb crystal. Data show the measured α that separates the 1D/zig-zag and 3D/radial-2D phases as a function of ion number. Three theory predictions (with no adjustable parameters) are plotted for comparison. Blue dashed, pseudopotential; Red solid, Floquet-Lyapunov; Orange dotted, micromotion-destabilized.

same crystal. In the absence of micromotion, the equilibrium positions for a 2D ion crystal proceed similarly to the 1D case. Since at higher alpha phases, the ions are compressed to a single plane at the axial trap center, there is effectively no micromotion amplitude along the axial direction, but in the radial direction, ions away from the central trap axis will experience micromotion, and the calculation of micromotion amplitude is presented in Chapter 2.

6.2.2 Structural Phase Boundaries

The phase boundaries of the structural transition can be obtained by measuring the axial and radial frequencies at the different critical points. We manually adjust the dc voltages to identify these critical points of the 2D crystal. Because secular frequencies only depend on the trap dimension and voltages, we can measure the secular frequencies of a single ion under the same voltages of these critical points by applying the way of injecting the rf voltage on one of the electrodes. The 1D chain -> zig-zag transition[114, 67] is well understood, because micromotion does not play a role, the structural phase transition occurs at approximately $\alpha = 0.73N^{0.86}$, as found numerically[23], this boundary can be analytically scaled by $\alpha = 0.77N/\sqrt{\log N}$[67] for large system. When the

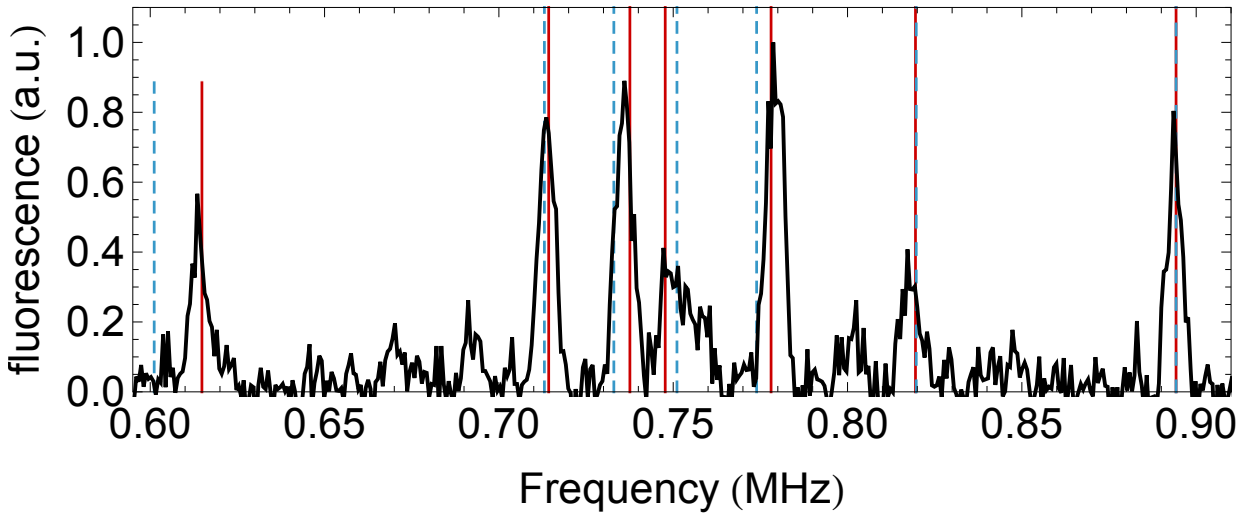

Figure 6.5: Axial mode spectrum for 7 ions in a radial-2D crystal at $\alpha = 2$. Vertical lines show predicted mode frequencies. Blue dashed, pseudopotential; Red solid, Floquet-Lyapunov.

radial confinement becomes strong compared to the axial confinement, the crystal buckles into three dimensions[67].The boundary of 3D helical and 2D triangular configuration is predicted by scaling weakly with the number of ions N in the trap[67]: $\alpha > (2.264N)^{1/4}$. However, this analysis didn't explicitly consider the rf traps, where micromotion appears and can have significant impacts. When taking the micromotion into account, the boundary scales weakly with the number of ions N with $\alpha \propto N^{0.27}$ (compared to $N^{0.25}$ previously)[49]. We measured these critical points with ions number up to 19. The blue dashed line is fitted with time-averaged pseudopotential [66], as shown in Fig. 6.4. A more accurate description, which accounts for the fully-coupled and time-dependent dynamics of ions position, called Floquet-Lyapunov (FL) transformation as described in Section 2, is shown as the solid red line in Fig. 6.4.

We applied a global, far-detuned Raman beam to excite the 2D ion crystal's transverse modes. In Fig. 6.5[115], we compare the measured axial mode frequency spectrum to frequencies calculated using the pseudopotential (blue dashed) and FL (red solid) approaches. These methods largely agree with the measured data within 2 kHz, and pseudopotential approximation may still provide reasonable accuracy for many experiments.

6.3 Micromotion Induced Heating

The presence of micromotion may have strong effects on crystal lifetimes and temperatures. When ions are confined into a 2D triangular lattice, ion-ion collisions can transfer micromotion energy into secular kinetic energy and result in rapid rf heating[116, 117]. This rf heating mechanism is anticipated to be dominated by other noise sources like electric field fluctuations and collisions with background gas molecules. First, we measured our crystal lifetimes. Similarly, we define lifetime as the time all ions remain in the crystal without cooling mechanisms, with $1/e$ probability. We find that it's longer than 5 seconds for crystals of up to 19 ions, which is long compared to typical experimental timescales[92, 118].

6.3.1 Voigt Fluorescence Profiles

Our measurements of the ion temperature begin by Doppler-cooling the ion crystal to around 0.5 mK, then extinguishing the cooling laser and allowing the crystal to heat for some time (with time step interval: 10 ms), then the temperature is re-measured. In this way, we measure the global heating rate of the crystal and determine the temperature of the radial-2D crystal by analyzing the ions' fluorescence line shape. The overall temperature of an ion crystal, related to thermal energy by $E = 3/2k_BT$, is described by a Voigt distribution (Eq. 6.1), is a convolution of Lorentzian and Gaussian profiles, where the Gaussian contribution is temperature-dependent. The Lorentzian contribution comes from the power-broadened natural linewidth, and the Gaussian contribution comes from doppler broadening as shown in Eq.6.2,6.3.

$$V(\delta;\sigma,\Gamma') = \int_{-\infty}^{\infty} G(\delta';\sigma)L(\delta-\delta';\Gamma')d\delta' \tag{6.1}$$

with power-broadened Lorentzian linewidth Γ' and Gaussian standard deviation σ,

$$\Gamma' = \Gamma\sqrt{1+s} = 2\pi \times 22MHz \tag{6.2}$$

$$\sigma = 2\sqrt{\frac{(2\ln 2)k_B}{m\lambda^2}}\sqrt{T_r \cos^2\theta + T_z \sin^2\theta} \tag{6.3}$$

where $\Gamma = 2\pi \times 19.6$ MHz is the nature linewidth, $s = 0.3$ is the laser saturation parameter, k_B is the Boltzmann constant, $\lambda = 369$ nm, $\theta = 45°$ comes from the intersect angle between fluorescence beam and the crystal plane, the T_r and T_z refer to the radial and axial temperatures. When ions doppler cooled, the Gaussian contribution is small, our first temperature point(Fig. 6.6 (a)) is around 0.5 mK. Then we extinguished the cooling beams for a specified time; the crystal acquires energy through rf heating, then the fluorescence profiles spread out, as in Fig. 6.6 (b) and (c). By performing a bunch of these temperature measurements at heating times increased, we determine the heating rate $\dot{T}_r = 1.04 \pm .08$ K/s. the linear nature of our data implies that short time scales, large ion masses, and low initial temperatures keep crystals far from this limit[117, 119].

6.3.2 Axial Heating Rate

Since the Voigt profiles measurement is global and doesn't sensitive to axial mode, we want to couple it with the Raman beam. We look for evidence of the heat transfer between the radial and axial direction; thus we measure the axial heating rate of the axial center-of-mass (COM) mode by resolved sideband spectroscopy[22]. We sideband cooling the our 7 ion crystal to $\bar{n} \leqslant 2.5$. Coherent oscillations of these sidebands result in profiles like those shown in Fig. 6.7(a) after the sideband cooling, where the average number of phonon occupation $\bar{n}$ defines from Eq. 5.7 $\bar{n} = r/(1-r)$, where r is the ratio of red to blue sideband transition probability amplitude.

We compare the axial COM heating rate of a single ion with a radial-2D crystal with seven ions under the same trapping condition. As shown in Fig. 6.7 (b), the axial heating rate of a single ion is $\dot{\bar{n}} = 100 \pm 20\ s^{-1}$. We determined the electrical field noise in the room-temperature rf trap of similar size[80], the noise is $S_E = 2.65 \times 10^{-12}\ V^2 m^{-2} Hz^{-1}$. This measurement with axial COM mode of a 7-ion crystal is repeated, finding that a heating rate $\dot{\bar{n}} = 125 \pm 75\ s^{-1}$ (Fig. 6.7 (c)). In temperature units, the rate is 200 times smaller than the measured radial heating(Fig. 6.6(d)).

Further evidence that electric field noise is not the primary heating process in our trap comes

from our measurements with one and seven ions. This is due to the expectation that the COM mode will be preferentially heated by electric field fluctuations, which are predicted to scale linearly with ion number and are highly correlated across the ions.[120, 80]. Instead, our findings point to mostly uncorrelated noise, which has also been seen in Penning traps using an analog to a radial-2D crystal[121].

In conclusion, our demonstration of stable, isolated, and low-noise axial modes establishes radial-2D crystals in linear Paul traps as a realistic platform for implementing several proposals in quantum simulation[50, 49]. Because long-range antiferromagnetic interactions between cotrapped ions are frequently implemented, and since ions in the radial-2D phase spontaneously form into a triangular lattice, this system is particularly well suited for research of highly frustrated quantum spin models[49, 48, 122]. We will be able to determine the excitation[122]and correlation functions of frustrated 2D spin models (which can distinguish, for example, between Neel states or valence bond solid states[123]) using only global laser beams. We can adjust the relative contributions of inherent geometric and long-range frustration.

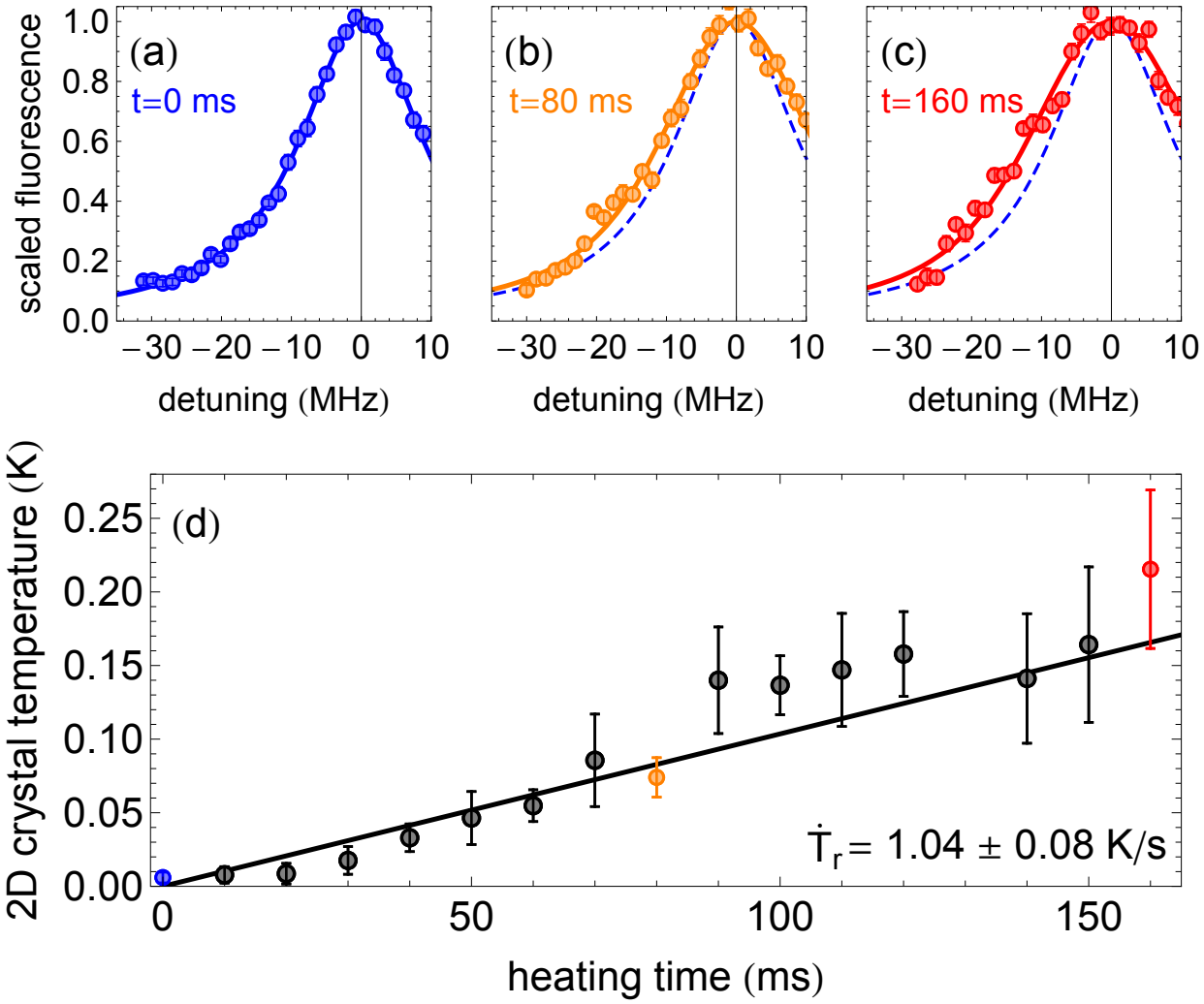

Figure 6.6: Voigt fluorescence lineshapes of a seven ion crystal exposed to rf heating are shown for heating times of (a) 0 ms, (b) 80 ms, and (c) 160 ms. The lineshape widens at later times due to increased contributions from Doppler broadening. A dashed blue line indicates the 0 ms profile (3 mK temperature) in panels (b) and (c) for reference. (d) A radial heating rate of T˙r = 1.04 ± .08 K/s is extracted from the Voigt profile fits ion fluorescence data.

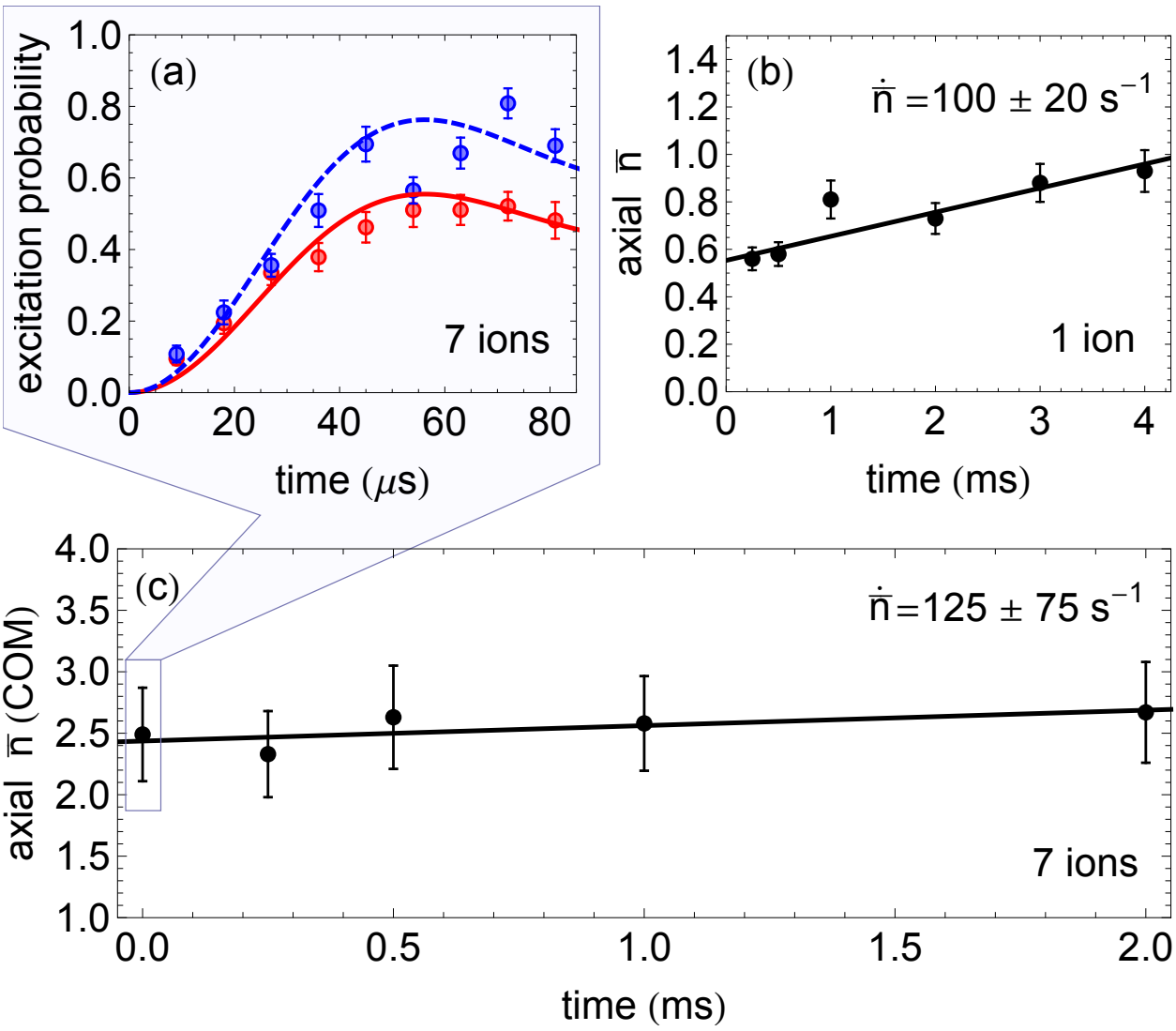

Figure 6.7: (a) A comparison of red (solid) and blue (dashed) sideband probability amplitudes is shown for a 7-ion crystal immediately following sideband cooling. The heating rate of the axial (transverse) COM mode for a single ion (b) is comparable to that of a 7-ion crystal (c). In both cases, the absolute heating rate is low compared to traps of similar size.

CHAPTER 7

Portable Trap with Radiation Study

7.1 Overview

Ionizing radiation from small-scale sources[124] and from cosmic rays[125] has recently been shown to limit the qubit coherence times and destroy quantum information stored throughout the chip. It is believed that ionizing radiation generates phonons in the chip substrate, breaking Cooper-paired electrons and producing large quasiparticle densities, which lead to qubit decoherence [126, 127]. These radiation events may result in broadly correlated errors between qubits, making it difficult or impossible to correct them using conventional fault-tolerant methods[128]. Trapped-ion quantum processors have not yet been used in any comparable radiation effects research. For instance, most ionizing radiation has enough energy to change the charge state of trapped ions, which would therefore destroy the qubit [129]. Even if the qubit survives, the presence of high-energy x-ray or γ photons may induce Stark shifts [130] or energy level fluctuations which reduce the qubit coherence time. Furthermore, high-energy radiation has the potential to ionize background gases, or release adsorbed atoms and photoelectrons from the vacuum chamber walls [131], which may lead to increased collisions or motional heating of the ions.

In this work, we study the effects of low-dose radiation on trapped-ion qubits. We first expose an ion-trap apparatus to an array of laboratory-scale α, β, and γ radiation sources to observe whether the ion-trapping lifetime is reduced. In the presence of those same sources, we next set limits on the changes in qubit coherence time and single-qubit rotation fidelity during exposure. Finally, we investigate whether low-dose radiation leads to increased motional heating rates of trapped ions.

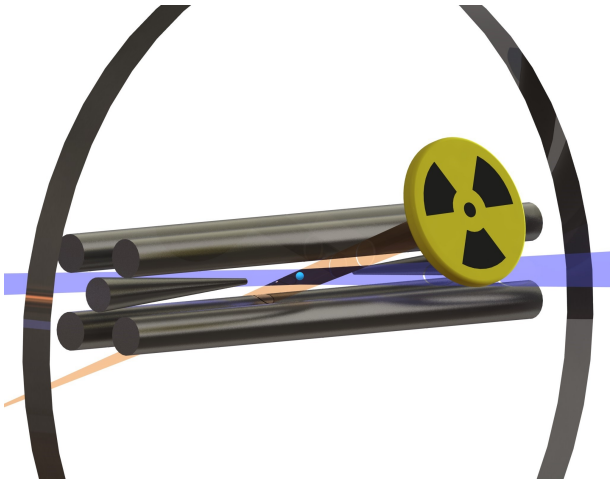

Figure 7.1: Sketch of the experimental arrangement (not to scale). Ions are confined in a “needle"-style rf trap housed inside a vacuum chamber. Laser beams (blue) are used for cooling and state-detection of the ions. Radiation (orange) emanates from a source outside the vacuum chamber and must pass through 4.65 mm of glass before interacting with the ions.

In all cases, our measurements of radiation effects are performed while the ion trap is in operation rather than irradiating the trap and testing afterward.

7.1.1 Experimental Apparatus

Ions are confined in a linear Radio Frequency (rf) trap with "needle"-style endcaps [57, 132]. Typical axial and radial trap frequencies for these experiments are $2\pi \times 390$ kHz and $2\pi \times 720$ kHz, respectively. The trap is housed within a vacuum chamber with pressures below 10^{-10} Torr so that collisions with background gas particles are minimized [22]. As shown in Fig. 7.1, radiation must also pass through one of the viewports before interacting with the ions.

Once the ion is created and trapped, lasers near 369 nm cool the ion to milliKelvin temperatures and initialize the qubit into the $|0\rangle$ state with $> 99\%$ fidelity [120]. Detection of the trapped ion qubits is performed optically using standard state-detection fluorescence techniques [27], with the collected light imaged onto a photo-multiplier tube (PMT) or EMCCD camera. Finally, qubit state manipulation in these experiments is performed by broadcasting 12.6 GHz radiation, resonant with the qubit states separation, using a microwave horn just outside the vacuum chamber.

Table 7.1: Radiation source table

Source	**Type**	**Activity**	**Energy (keV)**	**Irradiance (W/m^{-2})**
Polonium-210	α	0.1 μCi	5300	≈ 0
Americium-241	α	1 μCi	5490	≈ 0
Strontium-90	β	0.1 μCi	546	2×10^{-15}
Thallium-204	β	10 μCi	764	2×10^{-8}
Cobalt-60	β, γ	1 μCi	β: 318; γ: 1170, 1330	β: 1×10^{-18}; γ: 2×10^{-4}
Cesium-137	β, γ	5 μCi	β: 512, 1170; γ: 662	β: 4×10^{-7}; γ: 2×10^{-4}
Cadmium-109	γ	10 μCi	88	6×10^{-5}
Barium-133	γ	10 μCi	81, 276, 304, 356, 384	3×10^{-4}

7.2 Radiation Source

We use a variety of α, β, and γ radiation sources to test the ion trap hardware. The isotopes employed in these studies are listed in table 7.1 together with information about their radiation types, activities, and primary decay energies. Each source is encapsulated in a 1-inch "button" package of U.S. Nuclear Regulatory Commission exempt quantity and installed outside the ion trap vacuum chamber (Fig. 7.1). The radiation must pass through 45.5 mm of air, 4.65 mm of glass, and 10.5 mm of vacuum to ions.

The presence of the glass vacuum window is expected to cause significant variations in the radiation dose at the ion, depending on the radiation type. For instance, it is known that α-radiation can be stopped by a piece of paper, while thick lead shielding is often required to attenuate γ-rays [131]. Consequently, the source activity alone is not sufficient to determine the radiation dose at the ion; interactions between the radiation and the vacuum window must be considered as well. Several different numerical methods were implemented to estimate the attenuation of α, β, and γ particles through the vacuum window[133]. The estimation of the irradiance at the ion for each source in the radiation resource table above is equivalent to the radiative energy flux passing through the trapping region inside the vacuum chamber.

7.3 Results

7.3.1 Lifetime Measurements

We estimate the trapping lifetime of ions exposed to radiation sources as a first step in examining the effects of radiation on trapped ion qubits. The "ion lifetime" refers to the $1/e$ time for which an ion qubit remains confined within the rf trap in the absence of cooling mechanisms. If radiation causes the ion trap to rapidly depopulate, neither normal quantum error-correction codes [134, 135, 136, 137, 138] nor more specialized codes that account for qubitloss[139, 140] may be able to correct the situation. Although ions have been confined in many systems for months, this requires continuous laser cooling, which is forbidden while a quantum computation is in process [24]. Without active cooling, there is the potential for collisions to cause unmitigated ion heating and eventual loss of the qubit. Radiation effects may further increase the local background gas pressure and collision rate, as well as further ionize Yb^+, which in both cases would lead to reduced trapping lifetimes. Our measurements find that ion lifetimes remain more than one second when exposed to every source of radiation listed in table 7.1. For each experiment, one ion is initially Doppler cooled to 0.5 mK, confined without any cooling for 1 second, then illuminated to confirm its survival in the trap, and ten trials are performed for each data point in each experiment. The 100% measured survival probability at one second indicates that the true $1/e$ lifetime is longer than one minute in all cases. We note that for ion-trap experiments, one second is already orders of magnitude longer than the typical $\sim 1 - 10$ millisecond timescales of quantum computation and simulation studies [118, 92].

7.4 Coherence time and Single-Qubit Gate Fidelity Measurements

We examine whether our system's coherence time is long enough to apply a single-qubit rotation in the presence of radiation and whether the radioactive sources have any discernible effects on the single-qubit gate fidelity. The single-qubit gates it the rotations around the $\hat{x}$ axis of the Bloch Sphere, $U(t) = e^{-i\sigma_x \Omega t/2}$, where σ_x is the Pauli X matrix and Ω is the Rabi frequency. Rotations

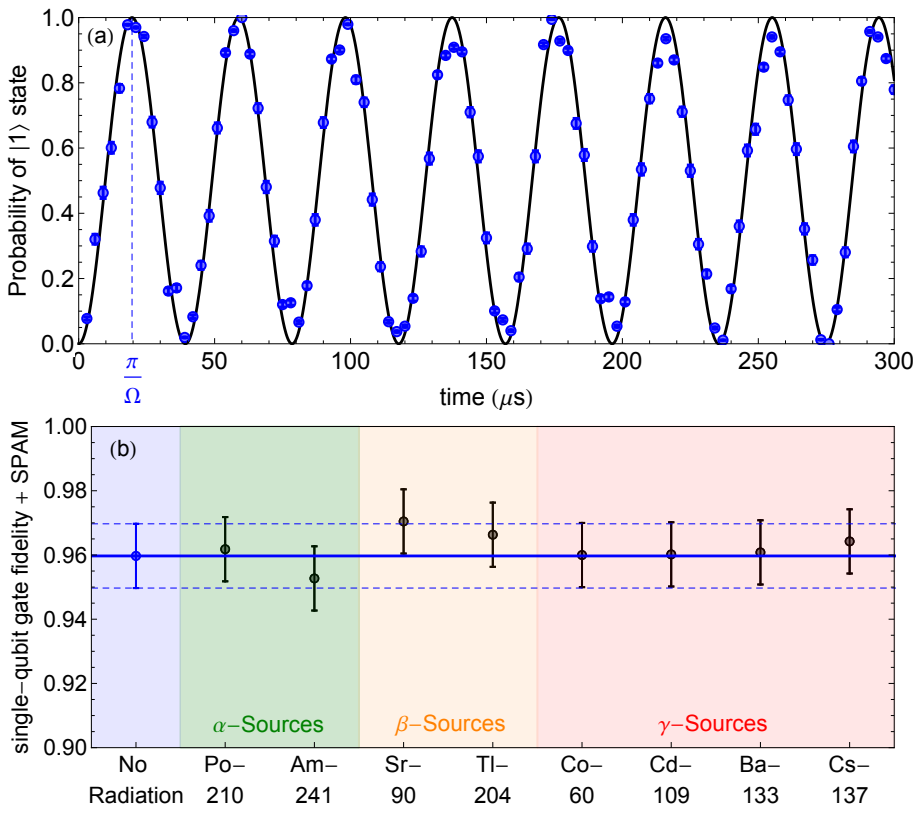

Figure 7.2: (a) Oscillations between qubit states $|0\rangle$ and $|1\rangle$ when driven with microwave pulses at 12.6 GHz, with no radiation present. (b) The single-qubit X-gate fidelities (including all state-preparation and measurement errors) remain unchanged within experimental error when various types of low-dose radiation are introduced. The solid blue line indicates the results of the control (no radiation) trial; the blue dashed lines indicate one s.d. measurement uncertainty.

are driven using microwaves resonant with the 12.6 GHz frequency splitting between qubit levels. When the qubit is initialized in $|0\rangle$ and microwaves are left on continuously, the qubit state oscillates between the $|0\rangle$ and $|1\rangle$ states at Rabi frequency $\Omega \approx 25$ kHz, as shown in Fig. 7.2(a). To estimate the average single-qubit X-gate fidelity, we apply the 12.6 GHz radiation for a time $t = \pi/\Omega$ and measure the population fraction transferred from the $|0\rangle \rightarrow |1\rangle$ state.

We measured the single-qubit X-gate fidelities (including SPAM errors), as shown in Fig. 7.2(b). We repeated our experimental trial by 1000 times to keep quantum projection noise errors at the level of $\sim 10^{-2}$. In comparison to our control trial, we found no difference in the single-qubit gate fidelity in the presence of radiation within experimental error. We, therefore, conclude that

(a) the coherence time of the trapped ion remained sufficient for single-qubit gate operations, and (b) there was no measurable effect from any isotope or dose of radiation applied in our trials. If radiation effects were indeed present, our measurements limit the resulting decrease in single-qubit gate fidelity to $< 1\%$.

7.5 Heating Rate Measurements

In a final set of experiments, we quantify the effects of radiation on the trapped ion temperature. Our measurements of the ion temperature begin by Doppler-cooling the ion to ≈ 0.5 mK. As we mentioned in Chapter 6, the cooling laser is turned off, and the ion is allowed to heat for 100 ms (much longer than the typical gate time of an ion-trap quantum computer [118]). Finally, the temperature is re-measured after 100 ms such that the heating rate can be determined. We then repeat this sequence in the presence of all radioactive sources listed in the radiation source table 7.1.

Temperature measurements of a trapped ion are performed by observing its fluorescence as a function of detuning δ from resonance. Such resonance lineshapes have two primary contributions, The Lorentzian contribution Eq. 6.2, and the Gaussian contribution Eq. 6.3, the fluorescence profile is most appropriately fit to a Voigt function Eq. 6.1. By fitting this lineshape to the measured fluorescence as a function of laser detuning, the only free parameter is the Gaussian width σ, which uniquely determines the ion temperature T.

Characteristic lineshapes for the control case (no radiation) and for α, β, and γ sources are shown in the top insets of Fig. 7.3. For the no-radiation case, the linewidth yields a fitted temperature of 25 mK after 100 ms of heating, corresponding to a heating rate of 0.25 K/s. This lineshape is replicated as a blue dashed line in the other three inset panels but is almost entirely covered by the radiation-present data. For each isotope and dose of radiation, we have fit a lineshape profile to extract a temperature and heating rate, plotting the summary of results in the bottom panel of Fig. 7.3. We observe no statistically significant increase in the heating rates when the ion trap is irradiated with low-dose α, β, or γ sources. Likewise, we observe no increase in the background

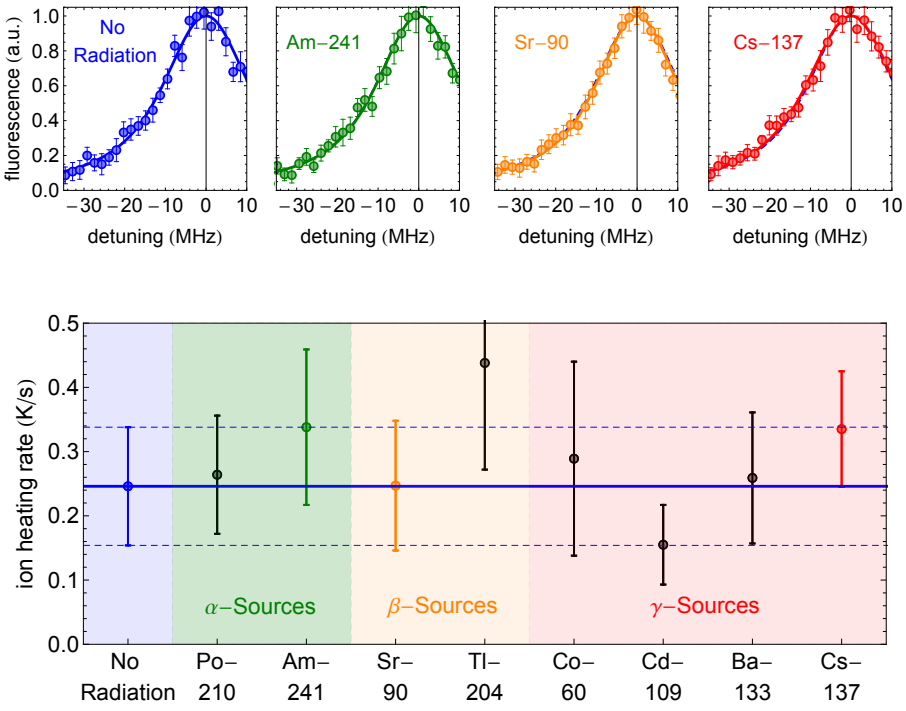

Figure 7.3: (Insets): measured ion fluorescence vs. detuning from resonance. The width of the lineshape determines the ion temperature. (Bottom) The extracted ion heating rates for various radiation sources. No statistically significant deviation in the heating rate is observed compared to the no-radiation case. The solid blue line indicates the results of the control (no radiation) trial; the blue dashed lines indicate one s.d. measurement uncertainty.

gas pressure at the 10^{-10} Torr level (which would increase the collisional heating rate), nor do we find that the ion shifts position in the trap due to unwanted charge accumulation (which would increase the electric field noise heating rate).

7.6 Further study: a Portable Trap for Radiation Study

We've studied the influence of low-dose radiation. However, the resiliency of ion trap systems to extreme radiation environments, as may be found in space, remains largely unknown. Such investigations are primarily complicated by the difficulty of integrating high-dose radiation sources within standard atomic-physics laboratories. Here, we report on the development of a portable ion trap specifically designed to fit within test chambers located at high-dose radiation test facilities. This platform is still based on laser-cooled Ytterbium ions, and the entire system is accommodated

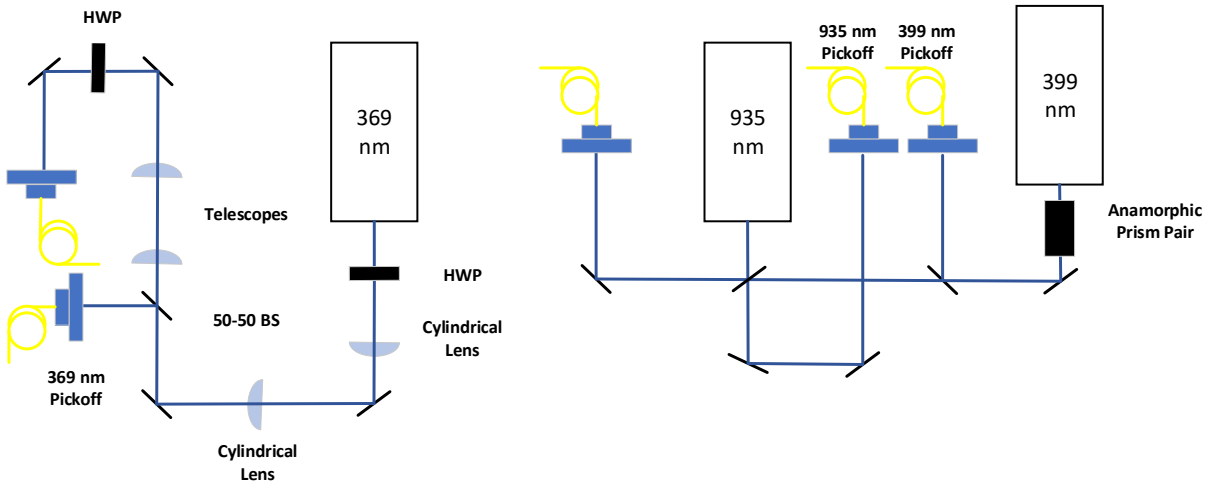

Figure 7.4: Optical pathways of the portable laser system.

into two mobile rack units which comprise a laser, electronics, and physics package subsystems. This study examines whether or not high-dose radiation causes correlated ion-qubit errors that are difficult to be corrected by using conventional fault-tolerant protocols, as well as more accurately quantifying the single-qubit gate errors using randomized benchmarking.

7.7 Optical Arrangement

An optical pathway diagram for our portable laser system is shown in Fig. 7.4. The Moglabs continuous wave (CW) produces 369 nm, 399 nm, and 935 nm light. The beam shape after the 369 nm and 399 nm light generator extends in the vertical direction. To increase the fiber coupling efficiency, the beam light reshape is necessary. Thus, there are two cylindrical lenses in the pathway of 369 nm to reshape the beam shape, as well as an anamorphic prism pair in front of the output port of 399nm, which has the same reshape effect. After the two cylindrical lenses, there is a 50-50 beamsplitter to separate a 369 nm light pickoff to the wavelength meter, and a telescope inside the pathway also contributes to increasing the fiber coupling efficiency. 399 nm and 935 nm beams are combined along the same pathway to the trap through fiber, 369 nm beam crosses with 399 nm and 935 nm beams and overlap on the ion. The output power at the final fiber coupler is listed here, Doppler: 100 uW, 399 nm: 2 mW, and 935 nm: 11 mW.

7.8 Portable Ion Trap

Fig. 7.5 (a) shows our "rod" style portable ion trap. The electrodes are fabricated by stainless steel rod with a diameter of 0.5 mm and assembled between two "H" shape Macor pieces. We put two Macor ceramic spacers mounted on the electrodes o keep the alignment of the dc endcap needle. The rf and rf ground electrodes form a square cage with a separation of 1.0 mm (r_0 = 0.207 mm), and the distance between two endcap needles is around 3 mm. The atomic oven sits in the back of the trap, and the tube's open end is situated in the chamber to aim through the trap's center. All dc electrodes are mechanically connected to gold-plated lugs, which are crimped to Kapton-coated wired and connected to Sub-C 9-pin feed-through. The rf electrodes and atomic ovens connect with separate high-power electrical feed-throughs. Fig. 7.5 (b) shows the Yb 174 ion cloud trapped by the portable ion trap, with a dc voltage of 1.2 V and rf voltage of 150 V.

Fig. 7.6 shows our portable miniature vacuum system, confined in a 10in.x 10in. x 18in. Box. To suit such a tiny box, as shown in Fig. 7.6(a), we have selected minor vacuum components, such as a 2.75" Spherical Hexagon (Kimball Physics Part #:53-160100), 1.33" mini all-metal angle valve (VAT 54.1 series UHV), NEG-ion combination pump(sae NEXTORR), and a CMOS camera (FLIR BFLY-PGE-23S6M-C). The hexagon main chamber has six 1.33" Conflat flange ports for either viewport or feedthrough connection. The radiation source towards the front viewport, high radiation would damage the camera and increase the detection noise; thus, there is a 0.5 cm thickness lead (the red plate in Fig.7.6) between the vacuum system and radiation source to prevent radiation from being received by CMOS camera. There is a 1.33" hole aligned with the front viewport to allow the radiation particle to fly to the trap. Two 1.33" viewports near the front viewport are connected with fiber couplers to focus the 399nm, 935nm, and 369nm beams to the ion trap center. Ion fluorescence passes the top 2.75" viewport, then through high refraction index image system with an optical path length 9" and magnification 30 times, there is a translation stage connected with the CMOS camera to give the ability to adjust the best image detection. We adopt a Sae NEXTORR ion pump that integrates a Non-evaporable getter (NEG) to our portable system; it has a small size but a high pump ability to pump the system to 10^{-10} Torr.

(a)

(b)

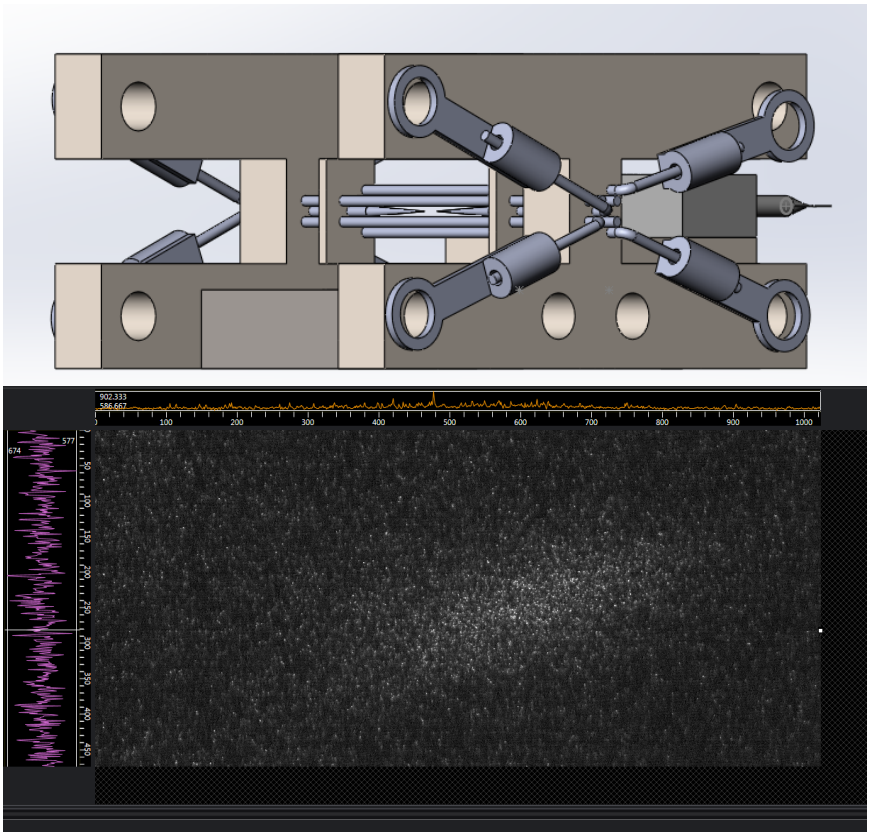

Figure 7.5: Trap design and ion cloud

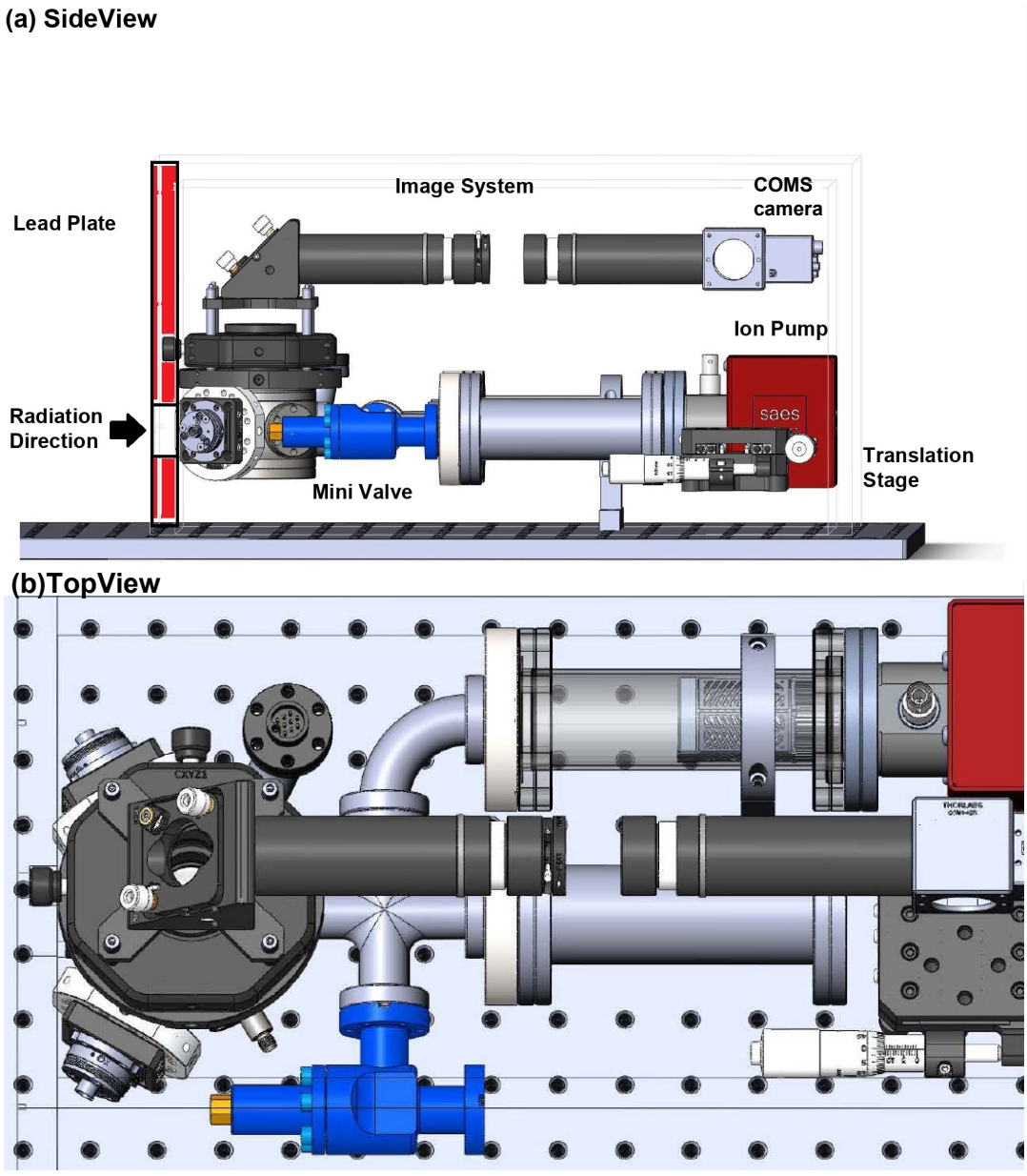

Figure 7.6: Topview and sideveiw of the Portable trap design

7.9 Integral System

The Control system and Laser system are compactly fitting a 23.6in. x 33.5in. x 35.5in. wheeled rack, as shown in Fig. 7.7, all lasers, laser controllers, Artiq box, and wavelength meter(not shown in the Figure) are mounted on the rack. The modules of the Artiq control system include Urukul, Zotino, SMA-DIO TTL, and Sampler, which can provide dc voltages and rf signals. Every laser has its own draw to set the beam pathway as shown in Sec.7.7. The pickoff of the laser goes to the wavelength meter, and the main beams are coupled with the fibers to the trap. We plan to test the stability of our system by loading the whole system on the truck and driving for around 30 mins, then measure the laser coupling efficiency and frequency modes stability, load an ion and check its brightness and position. In the coming months, the trapped ion will be exposed to a variety of α, β, and γ laboratory high-dose radiation sources. We will measure the changes in ion lifetimes, coherence times, gate fidelities, and motional heating rates. The low-dose radiation results show trapped ion-based quantum systems may be robust in extreme environments. With this project, we seek to determine the limits by applying high-dose radiation experiments still in progress.

Figure 7.7: Compact mobile system

CHAPTER 8

Outlook

Trapped ion quantum systems offer the ability to control and manipulate the quantum spin models, which have concentrated on studies of the Ising model. In this thesis, I presented a well-controlled, scalable quantum simulator for studying the behavior of a complex, 2- dimensional quantum spin system. This tunable and reconfigurable apparatus allows us to simulate more complex spin models, such as Heisenberg couplings [141], spin liquids[142], frustration, and high-Tc superconductivity. For ions not located at an rf null, which is restricted to a point or a line in space, 2D or 3D ion crystals in an rf trap must be accompanied by significant rf micromotion[60], Although micromotion introduces a collection of adjusting on laser cooling, ion detection, gate operation, and the micromotion effects can be mitigated by proper gate design[143]. Our quantum simulator currently can trap up to 29 ions in radial-2D crystals, and it can scale the system up to hundreds of ions crystal. This needs to characterize the voltages applied on the electrodes to get a stable crystal and minimize the micromotion amplitude. A native 2D crystal created by the 2D trap is the natural platform for realizing rich spin Hamiltonian in a more complex shape and the lasers are also made simpler with 2D lattice because only global beams are needed to produce 2D interactions. Additionally, the outputs have considerably higher fidelity due to fewer operations being needed. At the end of this article, for future research, I think there are two aspects that can be considered.

We have presented the optimized protocol for pulsed sideband cooling; however, even with the optimization, the sideband cooling is still the most extended experiment time component because of all collective modes of the coupled harmonic oscillator system cooling becomes slow as the

system size increases[144]. There are two different ways may help us optimize the cooling process, and we may try them in our later experiments. First, the continuous Raman sideband cooling [145] to the motional ground state beyond the Lamb-Dicke (LD) regime. If we simultaneously apply weak pumping lights to lower phonon occupancy and reset the qubits while driving multiple RSB transitions continually, this would have the dual benefits of offering robustness to timing faults and an extensive bandwidth that is not limited by the number of ions. The second plan is to introduce the Electromagnetically-Induced Transparency (EIT) cooling[146]. This idea comes form the restricted excitation range of resolved-sideband transitions, it is challenging to conduct simultaneous ground-state cooling for several motional modes of large crystals. Additionally, some sideband transitions triggered by high-power lasers[147], which is exacerbated for UV laser beams, are also introduced as a charging issue. The EIT cooling has been demonstrated that crystals are cooled down close to their ground states in hundreds of microseconds with cooling rates equivalent to that cooling rate of a single ion for multiple motional modes[146].

We identify lateral and radial 2D crystals by their direction of the crystal and micromotion. Since the lateral 2D crystal has micromotion along the transverse direction (perpendicular to the crystal plane) will couple with the Raman beams, which will affect the outcome of a quantum simulation. However, proper design of the trap[26] can cancel this micromotion to the first order, and the residual effects of micromotion in 2D traps can be well characterized. Previous evidence[120] shows that the size of the 2D crystal and its stability are sensitive to the electrode alignment. When ions are squeezed into a 2D plane, the rf null position no longer exists for the whole crystal; any misaligned electrode will induce strangeness rf heating. A monolithic micro-fabricated trap is ideal for trapping lateral 2D crystals with a large number of ions[26] because laser engraving is much more accurate than hand alignment. With the micro-fabrication techniques, recent works about this configuration have been conducted in characterization[148] with over 20 ions, then scaling the system up to 91 ions recently in Innsbruck university's group, it would be a direction worth trying for 2D crystal.

Bibliography

[1] Richard P. Feynman. Simulating physics with computers. *International Journal of Theoretical Physics*, 21(6):467–488, Jun 1982.

[2] Michael J. Hartmann, Fernando G. S. L. Brandão, and Martin B. Plenio. Strongly interacting polaritons in coupled arrays of cavities. *Nature Physics*, 2(12):849–855, Dec 2006.

[3] Andrew D. Greentree, Charles Tahan, Jared H. Cole, and Lloyd C. L. Hollenberg. Quantum phase transitions of light. *Nature Physics*, 2(12):856–861, Dec 2006.

[4] D. Jaksch and P. Zoller. The cold atom hubbard toolbox. *Annals of Physics*, 315(1):52–79, 2005. Special Issue.

[5] Jean Dalibard, Fabrice Gerbier, Gediminas Juzeliūnas, and Patrik Öhberg. Colloquium: Artificial gauge potentials for neutral atoms. *Rev. Mod. Phys.*, 83:1523–1543, Nov 2011.

[6] Immanuel Bloch, Jean Dalibard, and Sylvain Nascimbène. Quantum simulations with ultracold quantum gases. *Nature Physics*, 8(4):267–276, Apr 2012.

[7] E. Manousakis. A quantum-dot array as model for copper-oxide superconductors: A dedicated quantum simulator for the many-fermion problem. *Journal of Low Temperature Physics*, 126(5):1501–1513, Mar 2002.

[8] Tim Byrnes, Na Young Kim, Kenichiro Kusudo, and Yoshihisa Yamamoto. Quantum simulation of fermi-hubbard models in semiconductor quantum-dot arrays. *Phys. Rev. B*, 78:075320, Aug 2008.

[9] T. Yamamoto, M. Watanabe, J. Q. You, Yu. A. Pashkin, O. Astafiev, Y. Nakamura, F. Nori, and J. S. Tsai. Spectroscopy of superconducting charge qubits coupled by a josephson inductance. *Phys. Rev. B*, 77:064505, Feb 2008.

[10] J. Q. You and Franco Nori. Atomic physics and quantum optics using superconducting circuits. *Nature*, 474(7353):589–597, Jun 2011.

[11] J. Q. You and Franco Nori. Superconducting circuits and quantum information. *Physics Today*, 58(11):42–47, Nov 2005.

[12] John Clarke and Frank K. Wilhelm. Superconducting quantum bits. *Nature*, 453(7198):1031–1042, Jun 2008.

[13] Andrew A. Houck, Hakan E. Türeci, and Jens Koch. On-chip quantum simulation with superconducting circuits. *Nature Physics*, 8(4):292–299, Apr 2012.

[14] Sebastian Schmidt and Jens Koch. Circuit qed lattices: Towards quantum simulation with superconducting circuits. *Annalen der Physik*, 525(6):395–412, Jun 2013.

[15] Diego Porras and J Ignacio Cirac. Effective quantum spin systems with trapped ions. *Physical review letters*, 92(20):207901, 2004.

[16] Diego Porras and J Ignacio Cirac. Quantum manipulation of trapped ions in two dimensional coulomb crystals. *Physical Review Letters*, 96(25):250501, 2006.

[17] J. Chiaverini and W. E. Lybarger. Laserless trapped-ion quantum simulations without spontaneous scattering using microtrap arrays. *Phys. Rev. A*, 77:022324, Feb 2008.

[18] Kihwan Kim, M-S Chang, Simcha Korenblit, Rajibul Islam, Emily E Edwards, James K Freericks, G-D Lin, L-M Duan, and Christopher Monroe. Quantum simulation of frustrated ising spins with trapped ions. *Nature*, 465(7298):590–593, 2010.

[19] R. Gerritsma, G. Kirchmair, F. Zähringer, E. Solano, R. Blatt, and C. F. Roos. Quantum simulation of the dirac equation. *Nature*, 463(7277):68–71, Jan 2010.

[20] B. P. Lanyon, C. Hempel, D. Nigg, M. Müller, R. Gerritsma, F. Zähringer, P. Schindler, J. T. Barreiro, M. Rambach, G. Kirchmair, M. Hennrich, P. Zoller, R. Blatt, and C. F. Roos. Universal digital quantum simulation with trapped ions. *Science*, 334(6052):57–61, 2011.

[21] Rainer Blatt and David Wineland. Entangled states of trapped atomic ions. *Nature*, 453(7198):1008–1015, Jun 2008.

[22] David J Wineland, C Monroe, Wayne M Itano, Dietrich Leibfried, Brian E King, and Dawn M Meekhof. Experimental issues in coherent quantum-state manipulation of trapped atomic ions. *Journal of Research of the National Institute of Standards and Technology*, 103(3):259, 1998.

[23] A Steane. The ion trap quantum information processor. *Applied Physics B*, 64(6):623–643, 1997.

[24] Christopher Monroe and Jungsang Kim. Scaling the ion trap quantum processor. *Science*, 339(6124):1164–1169, 2013.

[25] Kenneth R Brown, Jungsang Kim, and Christopher Monroe. Co-designing a scalable quantum computer with trapped atomic ions. *Nature Quantum Information*, 2(1):1–10, 2016.

[26] Pengfei Wang, Chun-Yang Luan, Mu Qiao, Mark Um, Junhua Zhang, Ye Wang, Xiao Yuan, Mile Gu, Jingning Zhang, and Kihwan Kim. Single ion qubit with estimated coherence time exceeding one hour. *Nature Communications*, 12(1):233, Jan 2021.

[27] Rachel Noek, Geert Vrijsen, Daniel Gaultney, Emily Mount, Taehyun Kim, Peter Maunz, and Jungsang Kim. High speed, high fidelity detection of an atomic hyperfine qubit. *Optics Letters*, 38(22):4735–4738, Nov 2013.

[28] C J Ballance, T P Harty, N M Linke, M A Sepiol, and D M Lucas. High-fidelity quantum logic gates using trapped-ion hyperfine qubits. *Physical Review Letters*, 117(6):060504, 2016.

[29] John P Gaebler, Ting Rei Tan, Y Lin, Y Wan, R Bowler, Adam C Keith, S Glancy, K Coakley, E Knill, D Leibfried, et al. High-fidelity universal gate set for be 9+ ion qubits. *Physical Review Letters*, 117(6):060505, 2016.

[30] Patrik Henelius and Anders W. Sandvik. Sign problem in monte carlo simulations of frustrated quantum spin systems. *Phys. Rev. B*, 62:1102–1113, Jul 2000.

[31] Anders W. Sandvik. Ground states of a frustrated quantum spin chain with long-range interactions. *Phys. Rev. Lett.*, 104:137204, Mar 2010.

[32] I M Buluta, M Kitaoka, S Georgescu, and S Hasegawa. Investigation of planar coulomb crystals for quantum simulation and computation. *Physical Review A*, 77(6):062320, 2008.

[33] IM Buluta and S Hasegawa. The structure of planar coulomb crystals in rf traps. *Journal of Physics B: Atomic, Molecular and Optical Physics*, 42(15):154004, 2009.

[34] Iulia Buluta and Franco Nori. Quantum simulators. *Science*, 326(5949):108–111, 2009.

[35] C. Monroe, W. C. Campbell, L.-M. Duan, Z.-X. Gong, A. V. Gorshkov, P. W. Hess, R. Islam, K. Kim, N. M. Linke, G. Pagano, P. Richerme, C. Senko, and N. Y. Yao. Programmable quantum simulations of spin systems with trapped ions. *Rev. Mod. Phys.*, 93:025001, Apr 2021.

[36] C. Monroe, D. M. Meekhof, B. E. King, W. M. Itano, and D. J. Wineland. Demonstration of a fundamental quantum logic gate. *Phys. Rev. Lett.*, 75:4714–4717, Dec 1995.

[37] Ferdinand Schmidt-Kaler, Hartmut Häffner, Mark Riebe, Stephan Gulde, Gavin P. T. Lancaster, Thomas Deuschle, Christoph Becher, Christian F. Roos, Jürgen Eschner, and Rainer Blatt. Realization of the cirac–zoller controlled-not quantum gate. *Nature*, 422(6930):408–411, Mar 2003.

[38] F. Schmidt-Kaler, H. Häffner, S. Gulde, M. Riebe, G. P. T. Lancaster, T. Deuschle, C. Becher, W. Hänsel, J. Eschner, C. F. Roos, and R. Blatt. How to realize a universal quantum gate with trapped ions. *Applied Physics B*, 77(8):789–796, Dec 2003.

[39] M. Riebe, K. Kim, P. Schindler, T. Monz, P. O. Schmidt, T. K. Körber, W. Hänsel, H. Häffner, C. F. Roos, and R. Blatt. Process tomography of ion trap quantum gates. *Phys. Rev. Lett.*, 97:220407, Dec 2006.

[40] Thomas Monz, Philipp Schindler, Julio T. Barreiro, Michael Chwalla, Daniel Nigg, William A. Coish, Maximilian Harlander, Wolfgang Hänsel, Markus Hennrich, and Rainer Blatt. 14-qubit entanglement: Creation and coherence. *Phys. Rev. Lett.*, 106:130506, Mar 2011.

[41] K. Kim, M.-S. Chang, R. Islam, S. Korenblit, L.-M. Duan, and C. Monroe. Entanglement and tunable spin-spin couplings between trapped ions using multiple transverse modes. *Phys. Rev. Lett.*, 103:120502, Sep 2009.

[42] T. Choi, S. Debnath, T. A. Manning, C. Figgatt, Z.-X. Gong, L.-M. Duan, and C. Monroe. Optimal quantum control of multimode couplings between trapped ion qubits for scalable entanglement. *Phys. Rev. Lett.*, 112:190502, May 2014.

[43] Robin C Sterling, Hwanjit Rattanasonti, Sebastian Weidt, Kim Lake, Prasanna Srinivasan, SC Webster, Michaël Kraft, and Winfried K Hensinger. Fabrication and operation of a two-dimensional ion-trap lattice on a high-voltage microchip. *Nature Communications*, 5:3637, 2014.

[44] Frederick Hakelberg, Philip Kiefer, Matthias Wittemer, Ulrich Warring, and Tobias Schaetz. Interference in a prototype of a two-dimensional ion trap array quantum simulator. *Phys. Rev. Lett.*, 123:100504, Sep 2019.

[45] Joseph W Britton, Brian C Sawyer, Adam C Keith, C-C Joseph Wang, James K Freericks, Hermann Uys, Michael J Biercuk, and John J Bollinger. Engineered two-dimensional

ising interactions in a trapped-ion quantum simulator with hundreds of spins. *Nature*, 484(7395):489–492, 2012.

[46] Martin Gärttner, Justin G Bohnet, Arghavan Safavi-Naini, Michael L Wall, John J Bollinger, and Ana Maria Rey. Measuring out-of-time-order correlations and multiple quantum spectra in a trapped-ion quantum magnet. *Nature Physics*, 13(8):781–786, 2017.

[47] Elena Jordan, Kevin A. Gilmore, Athreya Shankar, Arghavan Safavi-Naini, Justin G. Bohnet, Murray J. Holland, and John J. Bollinger. Near ground-state cooling of two-dimensional trapped-ion crystals with more than 100 ions. *Phys. Rev. Lett.*, 122:053603, Feb 2019.

[48] R Nath, M Dalmonte, A W Glaetzle, P Zoller, F Schmidt-Kaler, and R Gerritsma. Hexagonal plaquette spin–spin interactions and quantum magnetism in a two-dimensional ion crystal. *New Journal of Physics*, 17(6):065018, jun 2015.

[49] Philip Richerme. Two-dimensional ion crystals in radio-frequency traps for quantum simulation. *Physical Review A*, 94(3):032320, 2016.

[50] Bryce Yoshimura, Marybeth Stork, Danilo Dadic, Wesley C. Campbell, and James K. Freericks. Creation of two-dimensional coulomb crystals of ions in oblate paul traps for quantum simulations. *EPJ Quantum Technology*, 2(1):2, Jan 2015.

[51] S-T Wang, Chao Shen, and L-M Duan. Quantum computation under micromotion in a planar ion crystal. *Scientific Reports*, 5:8555, 2015.

[52] M Block, A Drakoudis, H Leuthner, P Seibert, and G Werth. Crystalline ion structures in a paul trap. *Journal of Physics B: Atomic, Molecular and Optical Physics*, 33(11):L375, 2000.

[53] Ye Wang, Mu Qiao, Zhengyang Cai, Kuan Zhang, Naijun Jin, Pengfei Wang, Wentao Chen, Chunyang Luan, Botao Du, Haiyan Wang, Yipu Song, Dahyun Yum, and Kihwan

Kim. Coherently manipulated 2d ion crystal in a monolithic paul trap. *Advanced Quantum Technologies*, 3(11):2000068, 2020.

[54] Mu Qiao, Ye Wang, Zhengyang Cai, Botao Du, Pengfei Wang, Chunyang Luan, Wentao Chen, Heung-Ryoul Noh, and Kihwan Kim. Double-electromagnetically-induced-transparency ground-state cooling of stationary two-dimensional ion crystals. *Physical Review Letters*, 126(2):023604, 2021.

[55] Marissa D'Onofrio, Yuanheng Xie, AJ Rasmusson, Evangeline Wolanski, Jiafeng Cui, and Philip Richerme. Radial two-dimensional ion crystals in a linear paul trap. *arXiv preprint arXiv:2012.12766*, 2020.

[56] MK Ivory, A Kato, A Hasanzadeh, and BB Blinov. A paul trap with sectored ring electrodes for experiments with two-dimensional ion crystals. *Review of Scientific Instruments*, 91(5):053201, 2020.

[57] Steve Olmschenk, Kelly C Younge, David L Moehring, Dzmitry N Matsukevich, Peter Maunz, and Christopher Monroe. Manipulation and detection of a trapped yb+ hyperfine qubit. *Physical Review A*, 76(5):052314, 2007.

[58] CJ Foot. *Atomic physics*. Oxford University Press, USA, 2005.

[59] M. G. Raizen, J. M. Gilligan, J. C. Bergquist, W. M. Itano, and D. J. Wineland. Ionic crystals in a linear paul trap. *Phys. Rev. A*, 45:6493–6501, May 1992.

[60] H. G. Dehmelt. *Radiofrequency Spectroscopy of Stored Ions I: Storage**Part II: Spectroscopy is now scheduled to appear in Volume V of this series.*, volume 3, pages 53–72. Academic Press, Jan 1968.

[61] D. J. Berkeland, J. D. Miller, J. C. Bergquist, W. M. Itano, and D. J. Wineland. Minimization of ion micromotion in a paul trap. *Journal of Applied Physics*, 83(10):5025–5033, May 1998.

[62] J. Keller, H. L. Partner, T. Burgermeister, and T. E. Mehlstäubler. Precise determination of micromotion for trapped-ion optical clocks. *Journal of Applied Physics*, 118(10):104501, Sep 2015.

[63] Chao Shen and L-M Duan. High-fidelity quantum gates for trapped ions under micromotion. *Physical Review A*, 90(2):022332, 2014.

[64] Yong Wan, Florian Gebert, Fabian Wolf, and Piet O. Schmidt. Efficient sympathetic motional-ground-state cooling of a molecular ion. *Phys. Rev. A*, 91:043425, Apr 2015.

[65] H Kaufmann, S Ulm, G Jacob, U Poschinger, H Landa, A Retzker, M B Plenio, and F Schmidt-Kaler. Precise experimental investigation of eigenmodes in a planar ion crystal. *Physical Review Letters*, 109(26):263003, 2012.

[66] Yuanheng Xie, Jiafeng Cui, Marissa D'Onofrio, A J Rasmusson, Stephen W Howell, and Philip Richerme. An open-endcap blade trap for radial-2d ion crystals. *Quantum Science and Technology*, 6(4):044009, sep 2021.

[67] Daniel H E Dubin. Theory of structural phase transitions in a trapped coulomb crystal. *Physical Review Letters*, 71(17):2753, 1993.

[68] H Landa, M Drewsen, B Reznik, and A Retzker. Modes of oscillation in radiofrequency paul traps. *New Journal of Physics*, 14(9):093023, 2012.

[69] H Landa, M Drewsen, B Reznik, and A Retzker. Classical and quantum modes of coupled mathieu equations. *Journal of Physics A: Mathematical and Theoretical*, 45(45):455305, 2012.

[70] Klaus Mølmer and Anders Sørensen. Multiparticle entanglement of hot trapped ions. *Physical Review Letters*, 82(9):1835, 1999.

[71] David Hucul, Ismail V Inlek, Grahame Vittorini, Clayton Crocker, Shantanu Debnath, Susan M Clark, and Christopher Monroe. Modular entanglement of atomic qubits using photons and phonons. *Nature Physics*, 11(1):37–42, 2015.

[72] Guido Pagano, PW Hess, HB Kaplan, WL Tan, Phil Richerme, Patrick Becker, Antonis Kyprianidis, Jiehang Zhang, Eric Birckelbaw, MR Hernandez, et al. Cryogenic trapped-ion system for large scale quantum simulation. *Quantum Science and Technology*, 4(1):014004, 2018.

[73] RC Sterling, MD Hughes, CJ Mellor, and WK Hensinger. Increased surface flashover voltage in microfabricated devices. *Applied Physics Letters*, 103(14):143504, 2013.

[74] Anthony Micheal Ransford. Old dog, new trick: High fidelity, background-free state detection of an ytterbium ion qubits. *Ph.D. thesis*, 2020.

[75] L. Deslauriers, S. Olmschenk, D. Stick, W. K. Hensinger, J. Sterk, and C. Monroe. Scaling and suppression of anomalous heating in ion traps. *Phys. Rev. Lett.*, 97:103007, Sep 2006.

[76] Tridib Ray, S. Jyothi, N. Bhargava Ram, and S. A. Rangwala. A thin wire ion trap to study ion–atom collisions built within a fabry–perot cavity. *Applied Physics B*, 114(1):267–273, Jan 2014.

[77] Kuan-Yu Lin, Guang Hao Low, and Isaac L. Chuang. Effects of electrode surface roughness on motional heating of trapped ions. *Phys. Rev. A*, 94:013418, Jul 2016.

[78] D.A. Hite, Y. Colombe, A.C. Wilson, D.T.C. Allcock, D. Leibfried, D.J. Wineland, and D.P. Pappas. Surface science for improved ion traps. *MRS Bulletin*, 38(10):826–833, 2013.

[79] D. A. Hite, Y. Colombe, A. C. Wilson, K. R. Brown, U. Warring, R. Jördens, J. D. Jost, K. S. McKay, D. P. Pappas, D. Leibfried, and D. J. Wineland. 100-fold reduction of electric-field noise in an ion trap cleaned with in situ argon-ion-beam bombardment. *Phys. Rev. Lett.*, 109:103001, Sep 2012.

[80] M Brownnutt, M Kumph, P Rabl, and R Blatt. Ion-trap measurements of electric-field noise near surfaces. *Reviews of Modern Physics*, 87(4):1419, 2015.

[81] Zhao Wang, Le Luo, Karthik Thadasina, Kim Qian, Jinming Cui, and Yunfeng Huang. Fabrication of ion-trap electrodes by self-terminated electrochemical etching. *EPJ Techniques and Instrumentation*, 3(1):3, Mar 2016.

[82] Martin John Madsen. Advanced ion trap development and ultrafast laser-ion interactions. *Ph.D. thesis*, 2006.

[83] Steven Matthew Olmschenk. Quantum teleportation between distant matter qubits. *Ph.D. thesis*, 2009.

[84] K. Odaka and S. Ueda. Dependence of outgassing rate on surface oxide layer thickness in type 304 stainless steel before and after surface oxidation in air. *Vacuum*, 47(6):689–692, Jun 1996.

[85] J. D. Siverns, L. R. Simkins, S. Weidt, and W. K. Hensinger. On the application of radio frequency voltages to ion traps via helical resonators. *Applied Physics B*, 107(4):921–934, Jun 2012.

[86] K. G. Johnson, J. D. Wong-Campos, A. Restelli, K. A. Landsman, B. Neyenhuis, J. Mizrahi, and C. Monroe. Active stabilization of ion trap radiofrequency potentials. *Review of Scientific Instruments*, 87(5):053110, 2016.

[87] P.T.H. Fisk, M.J. Sellars, M.A. Lawn, C. Coles, A.G. Mann, and D.G. Blair. Very high q microwave spectroscopy on trapped /sup 171/yb/sup +/ ions: application as a frequency standard. *IEEE Transactions on Instrumentation and Measurement*, 44(2):113–116, 1995.

[88] P.T.H. Fisk, M.J. Sellars, M.A. Lawn, and G. Coles. Accurate measurement of the 12.6 ghz "clock" transition in trapped /sup 171/yb/sup +/ ions. *IEEE Transactions on Ultrasonics, Ferroelectrics, and Frequency Control*, 44(2):344–354, 1997.

[89] D. J. Wineland. Trapped ions, laser cooling, and better clocks. *Science*, 226(4673):395–400, Oct 1984.

[90] Martin W. van Mourik, Pavel Hrmo, Lukas Gerster, Benjamin Wilhelm, Rainer Blatt, Philipp Schindler, and Thomas Monz. rf-induced heating dynamics of noncrystallized trapped ions. *Phys. Rev. A*, 105:033101, Mar 2022.

[91] Kazi Rajibul Islam. Quantum simulation of interacting spin models with trapped ions. *Ph.D. thesis*, 2012.

[92] Philip Richerme, Zhe-Xuan Gong, Aaron Lee, Crystal Senko, Jacob Smith, Michael Foss-Feig, Spyridon Michalakis, Alexey V Gorshkov, and Christopher Monroe. Non-local propagation of correlations in quantum systems with long-range interactions. *Nature*, 511(7508):198–201, 2014.

[93] J. Uckert and Simon Stellmer. Fast raman transitions for ramsey interferometry. 2019.

[94] HC Nägerl, D Leibfried, F Schmidt-Kaler, J Eschner, and Rainer Blatt. Coherent excitation of normal modes in a string of ca+ ions. *Optics Express*, 3(2):89–96, 1998.

[95] RG DeVoe, J Hoffnagle, and RG Brewer. Role of laser damping in trapped ion crystals. *Physical Review A*, 39(9):4362, 1989.

[96] Lucia Duca, Naoto Mizukami, Elia Perego, Massimo Inguscio, and Carlo Sias. Orientational melting in a mesoscopic system of charged particles, 2022.

[97] M. Bonitz, P. Ludwig, H. Baumgartner, C. Henning, A. Filinov, D. Block, O. Arp, A. Piel, S. Käding, Y. Ivanov, A. Melzer, H. Fehske, and V. Filinov. Classical and quantum coulomb crystals. *Physics of Plasmas*, 15(5):055704, May 2008.

[98] Vitaly A. Schweigert and François M. Peeters. Spectral properties of classical two-dimensional clusters. *Phys. Rev. B*, 51:7700–7713, Mar 1995.

[99] F. Diedrich, J. C. Bergquist, Wayne M. Itano, and D. J. Wineland. Laser cooling to the zero-point energy of motion. *Phys. Rev. Lett.*, 62:403–406, Jan 1989.

[100] Regina Lechner, Christine Maier, Cornelius Hempel, Petar Jurcevic, Ben P Lanyon, Thomas Monz, Michael Brownnutt, Rainer Blatt, and Christian F Roos. Electromagnetically-induced-transparency ground-state cooling of long ion strings. *Physical Review A*, 93(5):053401, 2016.

[101] L Feng, WL Tan, A De, A Menon, A Chu, G Pagano, and C Monroe. Efficient ground-state cooling of large trapped-ion chains with an electromagnetically-induced-transparency tripod scheme. *Physical Review Letters*, 125(5):053001, 2020.

[102] D. J. Wineland and Wayne M. Itano. Laser cooling of atoms. *Phys. Rev. A*, 20:1521–1540, Oct 1979.

[103] J.-S. Chen, S. M. Brewer, C. W. Chou, D. J. Wineland, D. R. Leibrandt, and D. B. Hume. Sympathetic ground state cooling and time-dilation shifts in an $^{27}Al^{+}$ optical clock. *Phys. Rev. Lett.*, 118:053002, Jan 2017.

[104] Jürgen Eschner, Giovanna Morigi, Ferdinand Schmidt-Kaler, and Rainer Blatt. Laser cooling of trapped ions. *J. Opt. Soc. Am. B*, 20(5):1003–1015, May 2003.

[105] C. Monroe, D. M. Meekhof, B. E. King, S. R. Jefferts, W. M. Itano, D. J. Wineland, and P. Gould. Resolved-sideband raman cooling of a bound atom to the 3d zero-point energy. *Phys. Rev. Lett.*, 75:4011–4014, Nov 1995.

[106] W. Neuhauser, M. Hohenstatt, P. Toschek, and H. Dehmelt. Optical-sideband cooling of visible atom cloud confined in parabolic well. *Phys. Rev. Lett.*, 41:233–236, Jul 1978.

[107] D. J. Wineland, Wayne M. Itano, J. C. Bergquist, and Randall G. Hulet. Laser-cooling limits and single-ion spectroscopy. *Phys. Rev. A*, 36:2220–2232, Sep 1987.

[108] A. J. Rasmusson, Marissa D'Onofrio, Yuanheng Xie, Jiafeng Cui, and Philip Richerme. Optimized pulsed sideband cooling and enhanced thermometry of trapped ions. *Phys. Rev. A*, 104:043108, Oct 2021.

[109] L. Deslauriers, P. C. Haljan, P. J. Lee, K-A. Brickman, B. B. Blinov, M. J. Madsen, and C. Monroe. Zero-point cooling and low heating of trapped $^{111}Cd^{+}$ ions. *Phys. Rev. A*, 70:043408, Oct 2004.

[110] H. Che, K. Deng, Z. T. Xu, W. H. Yuan, J. Zhang, and Z. H. Lu. Efficient raman sideband cooling of trapped ions to their motional ground state. *Phys. Rev. A*, 96:013417, Jul 2017.

[111] J.-S. Chen, S. M. Brewer, C. W. Chou, D. J. Wineland, D. R. Leibrandt, and D. B. Hume. Sympathetic ground state cooling and time-dilation shifts in an $^{27}Al^{+}$ optical clock. *Phys. Rev. Lett.*, 118:053002, Jan 2017.

[112] D. M. Meekhof, C. Monroe, B. E. King, W. M. Itano, and D. J. Wineland. Generation of nonclassical motional states of a trapped atom. *Phys. Rev. Lett.*, 76:1796–1799, Mar 1996.

[113] A. Mortensen, E. Nielsen, T. Matthey, and M. Drewsen. Observation of three-dimensional long-range order in small ion coulomb crystals in an rf trap. *Phys. Rev. Lett.*, 96:103001, Mar 2006.

[114] J P Schiffer. Phase transitions in anisotropically confined ionic crystals. *Physical Review Letters*, 70(6):818, 1993.

[115] W C Campbell, J Mizrahi, Q Quraishi, C Senko, D Hayes, D Hucul, D N Matsukevich, P Maunz, and C Monroe. Ultrafast gates for single atomic qubits. *Physical Review Letters*, 105(9):090502, 2010.

[116] Vladimir L Ryjkov, Xian Zhen Zhao, and Hans A Schuessler. Simulations of the rf heating rates in a linear quadrupole ion trap. *Physical Review A*, 71(3):033414, 2005.

[117] Chaobo B Zhang, D Offenberg, B Roth, M A Wilson, and S Schiller. Molecular-dynamics simulations of cold single-species and multispecies ion ensembles in a linear paul trap. *Physical Review A*, 76(1):012719, 2007.

[118] Norbert M Linke, Dmitri Maslov, Martin Roetteler, Shantanu Debnath, Caroline Figgatt, Kevin A Landsman, Kenneth Wright, and Christopher Monroe. Experimental comparison of two quantum computing architectures. *Proceedings of the National Academy of Sciences*, 114(13):3305–3310, 2017.

[119] Kuang Chen, Scott T Sullivan, Wade G Rellergert, and Eric R Hudson. Measurement of the coulomb logarithm in a radio-frequency paul trap. *Physical Review Letters*, 110(17):173003, 2013.

[120] Marissa D'Onofrio, Yuanheng Xie, A. J. Rasmusson, Evangeline Wolanski, Jiafeng Cui, and Philip Richerme. Radial two-dimensional ion crystals in a linear paul trap. *Phys. Rev. Lett.*, 127:020503, Jul 2021.

[121] Brian C Sawyer, Joseph W Britton, and John J Bollinger. Spin dephasing as a probe of mode temperature, motional state distributions, and heating rates in a two-dimensional ion crystal. *Physical Review A*, 89(3):033408, 2014.

[122] Leon Balents. Spin liquids in frustrated magnets. *Nature*, 464(7286):199–208, 2010.

[123] Claire Lhuillier. Frustrated quantum magnets. *arXiv preprint cond-mat/0502464*, 2005.

[124] Antti P. Vepsäläinen, Amir H. Karamlou, John L. Orrell, Akshunna S. Dogra, Ben Loer, Francisca Vasconcelos, David K. Kim, Alexander J. Melville, Bethany M. Niedzielski, Jonilyn L. Yoder, Simon Gustavsson, Joseph A. Formaggio, Brent A. VanDevender, and William D. Oliver. Impact of ionizing radiation on superconducting qubit coherence. *Nature*, 584(7822):551–556, Aug 2020.

[125] Matt McEwen, Lara Faoro, Kunal Arya, Andrew Dunsworth, Trent Huang, Seon Kim, Brian Burkett, Austin Fowler, Frank Arute, Joseph C. Bardin, Andreas Bengtsson, Alexander Bilmes, Bob B. Buckley, Nicholas Bushnell, Zijun Chen, Roberto Collins, Sean Demura, Alan R. Derk, Catherine Erickson, Marissa Giustina, Sean D. Harrington, Sabrina Hong, Evan Jeffrey, Julian Kelly, Paul V. Klimov, Fedor Kostritsa, Pavel Laptev, Aditya Locharla, Xiao Mi, Kevin C. Miao, Shirin Montazeri, Josh Mutus, Ofer Naaman, Matthew Neeley, Charles Neill, Alex Opremcak, Chris Quintana, Nicholas Redd, Pedram Roushan, Daniel Sank, Kevin J. Satzinger, Vladimir Shvarts, Theodore White, Z. Jamie Yao, Ping Yeh, Juhwan Yoo, Yu Chen, Vadim Smelyanskiy, John M. Martinis, Hartmut Neven, Anthony Megrant, Lev Ioffe, and Rami Barends. Resolving catastrophic error bursts from cosmic rays in large arrays of superconducting qubits. *Nature Physics*, 18(1):107–111, Jan 2022.

[126] John M. Martinis, M. Ansmann, and J. Aumentado. Energy decay in superconducting josephson-junction qubits from nonequilibrium quasiparticle excitations. *Phys. Rev. Lett.*, 103:097002, Aug 2009.

[127] A. G. Kozorezov, A. F. Volkov, J. K. Wigmore, A. Peacock, A. Poelaert, and R. den Hartog. Quasiparticle-phonon downconversion in nonequilibrium superconductors. *Phys. Rev. B*, 61:11807–11819, May 2000.

[128] Austin G. Fowler and John M. Martinis. Quantifying the effects of local many-qubit errors and nonlocal two-qubit errors on the surface code. *Phys. Rev. A*, 89:032316, Mar 2014.

[129] Simon Heugel, Martin Fischer, Vladimir Elman, Robert Maiwald, Markus Sondermann, and Gerd Leuchs. Resonant photo-ionization of yb⁺to yb²⁺. *Journal of Physics B: Atomic, Molecular and Optical Physics*, 49(1):015002, Dec 2015.

[130] Gordon WF Drake. *Atomic, molecular and optical physics handbook*. Oxford Univ. Press, 1996.

[131] James E Turner. *Atoms, radiation, and radiation protection*. John Wiley & Sons, Weinheim, 2008.

[132] Stephan Gulde. Experimental realization of quantum gates and the deutsch-josza algorithm with trapped 40ca+–ions. *Universität Innsbruck, Ph.D. Dissertation*, 2003.

[133] Jiafeng Cui, A. J. Rasmusson, Marissa D'Onofrio, Yuanheng Xie, Evangeline Wolanski, and Philip Richerme. Susceptibility of trapped-ion qubits to low-dose radiation sources. *Journal of Physics B: Atomic, Molecular and Optical Physics*, 2021.

[134] E. Knill. Quantum computing with realistically noisy devices. *Nature*, 434(7029):39–44, Mar 2005.

[135] Robert Raussendorf and Jim Harrington. Fault-tolerant quantum computation with high threshold in two dimensions. *Phys. Rev. Lett.*, 98:190504, May 2007.

[136] D. Nigg, M. Müller, E. A. Martinez, P. Schindler, M. Hennrich, T. Monz, M. A. Martin-Delgado, and R. Blatt. Quantum computations on a topologically encoded qubit. *Science*, 345(6194):302–305, Jul 2014.

[137] Norbert M. Linke, Mauricio Gutierrez, Kevin A. Landsman, Caroline Figgatt, Shantanu Debnath, Kenneth R. Brown, and Christopher Monroe. Fault-tolerant quantum error detection. *Science Advances*, 3(10):e1701074, 2022/09/28 XXXX.

[138] Laird Egan, Dripto M. Debroy, Crystal Noel, Andrew Risinger, Daiwei Zhu, Debopriyo Biswas, Michael Newman, Muyuan Li, Kenneth R. Brown, Marko Cetina, and Christopher Monroe. Fault-tolerant control of an error-corrected qubit. *Nature*, 598(7880):281–286, Oct 2021.

[139] Thomas M. Stace, Sean D. Barrett, and Andrew C. Doherty. Thresholds for topological codes in the presence of loss. *Phys. Rev. Lett.*, 102:200501, May 2009.

[140] Roman Stricker, Davide Vodola, Alexander Erhard, Lukas Postler, Michael Meth, Martin Ringbauer, Philipp Schindler, Thomas Monz, Markus Müller, and Rainer Blatt. Experimental deterministic correction of qubit loss. *Nature*, 585(7824):207–210, Sep 2020.

[141] Tobias Graß and Maciej Lewenstein. Trapped-ion quantum simulation of tunable-range heisenberg chains. *EPJ Quantum Technology*, 1(1):8, Jun 2014.

[142] Leon Balents. Spin liquids in frustrated magnets. *Nature*, 464(7286):199–208, Mar 2010.

[143] C. Shen, Z. Zhang, and L.-M. Duan. Scalable implementation of boson sampling with trapped ions. *Phys. Rev. Lett.*, 112:050504, Feb 2014.

[144] J.-S. Chen, K. Wright, N. C. Pisenti, D. Murphy, K. M. Beck, K. Landsman, J. M. Amini, and Y. Nam. Efficient-sideband-cooling protocol for long trapped-ion chains. *Phys. Rev. A*, 102:043110, Oct 2020.

[145] Qiming Wu, Yue Shi, and Jiehang Zhang. Continuous raman sideband cooling beyond the lamb-dicke regime in a trapped ion chain, 2022.

[146] Mu Qiao, Ye Wang, Zhengyang Cai, Botao Du, Pengfei Wang, Chunyang Luan, Wentao Chen, Heung-Ryoul Noh, and Kihwan Kim. Double-electromagnetically-induced-transparency ground-state cooling of stationary two-dimensional ion crystals. *Phys. Rev. Lett.*, 126:023604, Jan 2021.

[147] M. Harlander, M. Brownnutt, W. Hänsel, and R. Blatt. Trapped-ion probing of light-induced charging effects on dielectrics. *New Journal of Physics*, 12(9):093035, Sep 2010.

[148] Ye Wang, Mu Qiao, Zhengyang Cai, Kuan Zhang, Naijun Jin, Pengfei Wang, Wentao Chen, Chunyang Luan, Botao Du, Haiyan Wang, Yipu Song, Dahyun Yum, and Kihwan Kim. Coherently manipulated 2d ion crystal in a monolithic paul trap. *Advanced Quantum Technologies*, 3(11):2000068, 2020.

Yuanheng Xie Email: xieyua2016@gmail.com
Github: github.com/Yuanheng-glitch

Education

- **Indiana University Bloomington** August 2016 - December 2022
  Ph.D- Physics *Supervisor: Prof.Phil Richerme*
- **University of Science and Technology of China** September 2012 - June 2016
  Bachelor of Science- Physics *Supervisor: Prof.Xiaohui Bao*

Projects

Indiana University Bloomington Graduate Research
Supervisor: Prof.Phil Richerme

Portable Ion Trap System: (Work in progress)Build a portable ion trap system, experimentally study the real-time susceptibility of trapped-ion quantum systems to ionizing radiation, measure the resulting changes in trapped-ion qubit lifetimes, coherence times, gate fidelities.

2D ion trap design and Construction: Design and construct a 2D ion trap and successfully trapped 2D ion crystal with up to 29 ions.

Optimized Pulsed Sideband Cooling: Calculate the fastest possible pulsed sideband cooling for a given number of pulses and develop and experimentally validate an improved method to measure ion temperatures after sideband cooling.

Characterize 2D ion crystal : Demonstrate the structural phase transition, transverse modes and measure the micromotion-induced heating with 7 ions in 2 dimensions.

PID controller Design: Design PID circuit bards to lock the Laser frequency and stabilized the amplitude of the RF wave.

ARTIQ (Advanced Real-Time Infrastructure for Quantum physics based on Python): Set up the control system for the quantum simulation experiments, generate precise timing pulses and implement quantum gates.

High Q factor Helical resonator: Build and calibrate a high voltage and low noise radio frequency resonator with a feedback loop.

Room Temperature Ultrahigh Vacuum System: Build a room temperature ultra high vacuum system at the pressure of $5 * 10^{-11}$ Torr.

University of Science and Technology of China Undergraduate Research
Supervisor: Prof.Xiaohui Bao

Atom heating effect during Zeeman optical pumping(Rb87): Calculate how many times does the optical pumping make the atomic energy completely out of the light trap and calculating pumping efficiency to guide the experiment.

Publications

Y. Xie, J. Cui, M. D'Onofrio, A.J. Rasmusson, S. Howell, and P. Richerme. **An Open-Endcap Blade Trap for Radial-2D Ion Crystals** . *Quantum Science and Technology 6, 044009.(2021)*

A.J. Rasmusson, M. D'Onofrio, Y. Xie, J. Cui, and P. Richerme. **Optimized Pulsed Sideband Cooling and Enhanced Thermometry of Trapped Ions** . *Phys. Rev. A 104, 043108 (2021)*

J. Cui, A.J. Rasmusson, M. D'Onofrio, Y. Xie, E. Wolanski, and P. Richerme. **Susceptibility of Trapped-Ion Qubits to Low-Dose Radiation Sources** . *J. Phys. B: At. Mol. Opt. Phys. 54, 13LT01 (2021)*

M. D'Onofrio, Y. Xie, A.J. Rasmusson, E. Wolanski, J. Cui, and P. Richerme. **Radial two-dimensional ion crystals in a linear Paul trap** . *Phys. Rev. Lett. 127, 020503 (2021)*

Talks and Poster Sessions

Building a Mobile Trap setup for severe environment study: NACTI 2022, Durham, North Carolina - August, 2022

An open-endcap blade trap for raidal-2D ion crystal: Midwest Cold Atom Workshop (MCAW), West Lafayette, Indiana - November, 2021

Characterization of Radial 2D Ion Crystals for Quantum simulation: The Quantum Economic Development Consortium(QED-C) Invited Talk - August, 2020

Characterization of Radial 2D Ion Crystals for Quantum simulation: The 51st Annual Meeting of the APS Division of Atomic, Molecular and Optical Physics, Portland, Oregon (Virtual) - June, 2020

Characterization of Radial 2D Ion Crystals for Quantum simulation: Midwest Cold Atom Workshop (MCAW), Evanston, Illinois - November, 2019

Characterization of Radial 2D Ion Crystals for Quantum simulation: Atomic Physics Gordon Conference, Newport, Rhode Island (Poster Session) - June, 2019

Skills Summary

Languages: Java, Wolfram Mathematica, Python, JavaScript, SQL